Influence of vacuum-assisted solvent evaporation on $MAPbI_3$ layers and solar cells

Dissertation zur Erlangung des akademischen Grades des Doktors der Naturwissenschaften (Dr. rer. nat.)

eingereicht im Fachbereich Biologie, Chemie, Pharmazie

der Freien Universität Berlin

vorgelegt von

Qin Tan

aus Guangan (Volksrepublik China)

Berlin, 2019

Die vorliegende Arbeit wurde in der Zeit von Oktober 2015 bis März 2019 im Institut für Si-Photovoltaik am Helmholtz-Zentrum Berlin für Materialien und Energie GmbH unter Leitung von PD Dr. Thomas Dittrich angefertigt.

1. Gutachter: PD Dr. Thomas Dittrich
2. Gutachter: Prof. Dr. Thomas Risse

Disputation am 16.10.2019

Acknowledgements

First of all I want to thank Prof. Martha Ch. Lux-Steiner for accepting me as his PhD student and giving me the opportunity to do my PhD thesis at the Helmholtz-Zentrum Berlin. Thank you for the great supervision and for helping me with your knowledge, your experience and the many long discussions we had. Acknowledgments also to Prof. xxx for his willingness to act as the co-examiner of this PhD thesis.

I am grateful to Prof. Nobert Nickel and Dr. Jörg Rappich for supporting my research at the Institut für Silizium-photovoltaik (EE-IS). Many thanks to Dr. Karsten Hinrichs, Dr. Mao Dong Huang, Dr. Steffen Fengler, Dr. Junming Li and Prof. Pongthep Prajongtat for the collaboration during my PhD studies.

Especially thanks to Dr. Lukas Kegelmann for critical reading of my thesis.

I want to thank my office mates, Dr. Felix Lang and Dr. Oleksandra Shargaieva. I really enjoyed our scientific discussion and thank you for the help with my experiments. I also want to thank Prof. Steve Albrecht, Dr. Lukas Kegelmann and for the support of building my experiment setup. Thanks to Carola Klimm for the SEM measurement and Thomas Lußky for the technical support. Also thanks to all other researchers and staffs for the supporting. Acknowledgments to Marion Krusche for assistance and patience with administrative work.

My PhD studies would not be possible without the financial support from the China Scholarship Council (CSC) and the Helmholtz Zentrum Berlin. I am grateful for the scholarships.

Last but not least, special thanks goes to my parents and girlfriend for their patience, motivation and understanding over the whole period of my PhD studies.

Table of Contents

Abstract

Hybrid organic-inorganic metal halide perovskites (HOIPs) belong to a class of semiconductors which can be deposited with very high quality from solutions so that solar cells with high efficiencies can be prepared at relatively low temperatures. methylammonium lead iodide ($MAPbI_3$) is an archetypical HOIP and served as a model system.

In this thesis, $MAPbI_3$ perovskite films were prepared by a vacuum-assisted evaporation of solvent (vacuum-assisted treatment) after spin coating of precursor solutions in combination with a post-annealing process. The vacuum-assisted treatment allowed for realization of practically ideal boundary conditions for studying out-diffusion of solvents.

The influence of the dimethyl formamide (DMF)/dimethyl sulfoxide (DMSO) ratio, temperature and time on morphology, the band gap, exponential tails and performance of solar cells was studied. In general, higher DMSO proportion, higher temperature and longer vacuum-assisted treatment time resulted in lower efficiencies. At the given pressure of 60 Pa, optimum conditions for the vacuum assisted treatment were found (DMF:DMSO = 9:1, 30 ℃, 10 s). It was shown that efficiencies above 20% can be realized with vacuum-assisted treatment and short post-annealing at 120 ℃ for solar cells based on $MAPbI_3$.

A methodology was developed for the quantitative measurement of residual solvent molecules in $MAPbI_3$ films by combining high resolution continuum source absorption spectrometry (HR-CSAS) and infrared spectroscopic ellipsometry (IRSE) and for diffusion analysis. For quantitative analysis, the area of the finger print peak of DMSO (S=O stretching mode, IRSE) was calibrated with the S/Pb molar ratio obtained by HR-CSAS.

The diffusion coefficient of DMSO in $MAPbI_3$ is a superposition of two thermally activated processes with E_{A1}, D_{01}, E_{A2} and D_{02} are 0.6 eV, 10^{-11} cm^2/s, 1.8 eV and $3.6x10^{-4}$ cm^2/s,

respectively, which can be assigned to activation of DMSO from loosely bonded complexes and from a trap site in the lattice of $MAPbI_3$.

The methodology and the knowledge about vacuum-assisted treatment and out-diffusion of solvent molecules can be transferred to the investigation of other systems such as multi-cation HOIPs.

Zusammenfassung

Hybride organisch-anorganische Metallhalogenidperowskite (HOIPs) gehören zu einer Klasse von Halbleitern, die mit sehr hoher Qualität aus Lösungen abgeschieden werden können, so dass Solarzellen mit hohem Wirkungsgrad bei relativ niedrigen Temperaturen hergestellt werden können. Methylammoniumbleiiodid ($MAPbI_3$) ist ein archetypischer HOIP und dient als Modellsystem.

In dieser Arbeit wurden dünne $MAPbI_3$-Perowskitschichten durch eine vakuumunterstützte Verdampfung des Lösungsmittels (vakuumunterstützte Behandlung) nach dem Spin Coating von Vorläuferlösungen in Kombination mit einer thermischen Nachbehandlung hergestellt. Die vakuumunterstützte Behandlung ermöglichte die Realisierung praktisch idealer Randbedingungen für die Untersuchung der Ausdiffusion von Lösungsmitteln.

Der Einfluss des Verhältnisses von Dimethylformamid (DMF)/Dimethylsulfoxid (DMSO), Temperatur und Zeit auf die Morphologie, die Bandlücke, exponentielle Bandausläufer und die Leistung von Solarzellen wurde untersucht. Im Allgemeinen führten ein höherer DMSO-Anteil, höhere Temperaturen und eine längere vakuumunterstützte Behandlungszeit zu niedrigeren Wirkungsgraden. Bei einem gegebenen Druck von 60 Pa wurden optimale Bedingungen für die vakuumunterstützte Behandlung gefunden (DMF:DMSO = 9:1, 30 °C, 10 s). Es wurde gezeigt, dass mit einer vakuumunterstützten Behandlung und einer kurzen thermischen Nachbehandlung bei 120 °C für Solarzellen auf Basis von $MAPbI_3$ Wirkungsgrade über 20% erreicht werden können.

Für die quantitative Messung von Restlösungsmittelmolekülen in $MAPbI_3$-Schichten wurde erstmals eine Methodik entwickelt, die hochauflösende Absorptionsspektrometrie mit kontinuierlicher Quelle (HR-CSAS: high resolution contiuum source absorption spectrometry) und spektroskopischer Ellipsometrie im Infrarotbereich (IRSE: infrared spectroscopic ellipsmetry) kombiniert und zur Diffusionsanalyse eingesetzt wird. Für die quantitative Analyse wurde die Fläche des spezifischen Absorptionspeaks von DMSO (S=O

Streckschwingung) mit dem von HR-CSAS erhaltenen S/Pb Molverhältnis kalibriert.

Der Diffusionskoeffizient von DMSO in $MAPbI_3$ wurde durch eine Überlagerung von zwei thermisch aktivierten Prozessen mit E_{A1}, D_{01}, E_{A2} und D_{02} sind 0.6 eV, 10^{-11} cm^2/s, 1.8 eV bzw. $3.6x10^{-4}$ cm^2/s beschrieben. Die thermisch aktivierten Prozesse entsprechen der Aktivierung von DMSO aus relativ lose gebundenen Komplexen und aus ins Gitter von $MAPbI_3$ eingebauten Molekülen.

Die Methodik und das Wissen über die vakuumunterstützte Behandlung und Ausdiffusion von Lösungsmittelmolekülen kann sowohl auf die Optimierung von Solarzellen als auch auf die Untersuchung der Diffusion von Lösungsmittelmolekülen in anderen HOIP Systemen, in welchen z.B. eine Vielzahl verschiedener Kationen und Anionen kombiniert werden, übertragen werden.

1. Introduction

As one of the renewable energies, solar energy can be harvested and transformed directly into electrical energy by photovoltaic devices. Solar cells are the primary application and can be categorized as first, second and third generation cells according to their development stages [1]. The first generation solar cells are built on silicon crystal, a predominant semiconductor for the photovoltaic technology. Crystalline silicon (c-Si) is the crystalline semblance of silicon and exists in two forms either single crystal or multiple crystal. The second generation solar cells consisting thin film are made of cadmium telluride (CdTe), copper indium gallium selenide (CIGS), gallium arsenide (GaAs) and amorphous silicon, whose layer thickness ranges from a few nanometers to tens of microns, which is much thinner as compared to the first generation solar cells made of crystalline silicon which employ wafers up to 200 μm. Other thin film technologies which are ongoing research and development phase are called third generation solar cells that comprise organic, dye-sensitized, polymer, copper tin zinc sulphide (CZTS), nanocrystals, micromorphs, quantum dots and perovskite solar devices.

Due to its remarkable rapid growth of power conversion efficiency (PCE), perovskite solar cells have drawn considerable interest and attention of the researchers. Perovskite solar cells generally consist of a hybrid organic-inorganic metal halide perovskite (HOIP) layer, which acts as a photo absorber as well as a charge carrier conductor. Kojima et al. [2] first used HOIP in dye-sensitized solar cells (DSSCs) and obtained a PCE of 3.81%. Since then, the HOIP solar cells have been rapidly developed and a PCE of 24.2% [3] has been reached. As the result of peculiar crystallographic structure, the HOIP group materials manifest a multitude of electronic properties including thermoelectric [4], piezoelectric [5] and semiconductivity depending on the material considered. In PV applications, they exhibit: (1) high mobilities and long diffusion lengths of charge carriers, (2) low non-radiative surface recombination rate, (3) high optical absorptivity and (4) excellent structural defect tolerance [6].

However, although HOIP materials offer exceptional properties suitable for photovoltaic applications, various challenges such as toxicity of Pb atoms and long-term stability still hinder their commercialization in PV market. Compared with the traditional solar cells, HOIP solar cells show benefits due to their relative low cost of fabrications. The HOIP film fabrication techniques, namely solution-processing, vapor deposition and hybrid processing (solution processing combined with vapor deposition) have been demonstrated to control the crystal formation and film morphology, which consequently affect the performance of HOIP solar cells. Solution engineering is shown to regulate the qualities of perovskite films and is therefore a key for enhancing the PCE.

In solution processing, there are several methods to control the crystallization of perovskite. Vacuum-assisted evaporation of solvents (vacuum-assisted treatment) is one of the promising intermediate steps for controlling the deposition of perovskites from solutions. It was firstly reported by Gao et al. [7] and named as a gas pump drying method. In this technique, a precursor solution layer formed after spin coating was exposed to vacuum in a very short time. Most of the solvent was removed immediately, thus leading an intermediate formed. Comparing with another method, the so-called anti-solvent dripping, there was no radial gradient in oversaturation which caused the spatially inhomogeneous nucleation of the HOIP or its intermediate [8]. The density of defects of HOIP films was reduced on a larger scale by using vacuum-assisted treatment. This enables to fabricate HOIP solar cells with relatively large areas exceeding 1 cm^2 showing high efficiencies. In previous studies, the influence of different pressures in this method was investigated, and different HOIP materials were used. Nevertheless, there are other factors affecting the process of vacuum-assisted treatment.

In this thesis, one of the most commonly used HOIP materials, methylammonium lead iodide ($MAPbI_3$), was chosen as the research subject. A self-build setup for vacuum-assisted treatment was used in the preparation of $MAPbI_3$ films. The influence of three major factors including solvent composition, temperature of the substrate during vacuum-assisted treatment and the time of vacuum-assisted treatment was investigated.

Resulting changes in the morphologies of MAPbI3 films, the band gaps (E_g) and exponential tails (E_t) of $MAPbI_3$ films and the performance of $MAPbI_3$ based solar cells were investigated.

As known from reports of other researchers, the formed intermediate such as MAI·PbI_2·DMSO helps to improve crystalline quality [9]. The intermediate is a kind of Lewis acid−base adduct [10], where the DMSO is an electron-pair donor defined as a base and the Pb^{2+} is an electron-pair acceptor defined as an acid. However, the coordination bond can be destroyed by heat energy, and the $MAPbI_3$ crystals finally form when DMSO is removed after post annealing. It can be assumed that the rate of DMSO escape influences the rate of $MAPbI_3$ crystallization and affects the crystalline quality. So, in this thesis, the out-diffusion of solvent depending on post annealing time and temperature was investigated through determining the amount of residual solvent by high-resolution continuum source absorption spectroscopy (HR-CSAS) and infrared spectroscopic ellipsometry (IRSE). Based on the analysis result and Fick's second law, a diffusion model was developed. The influence on morphologies, band gaps and exponential tails of $MAPbI_3$ were also studied. The performance of solar cells based on $MAPbI_3$ prepared with different post annealing time and temperature was characterized and parameters were optimized for reaching high PCEs.

In **Chapter 2**, the crystal structures and basic properties (including optical and electronic properties) of HOIPs were described. An overview of different preparation methods for HOIP films was given. The working principle and architectures of single-junction and multi-junction HOIP solar cells were also introduced.

Chapter 3 mainly introduced the materials and methods which were used in this thesis. Firstly, the methods and the self-build setup for $MAPbI_3$ layer preparation were described. A series of equipment including a pump, a big buffer tank and a small chamber in the glovebox made up the vacuum-assisted treatment setup. A precursor layer of $MAPbI_3$ on a substrate was deposited by spin coating in a glovebox and then treated in the small chamber.

After post annealing on a hot plate, a $MAPbI_3$ layer formed. Secondly, the fabrication of $MAPbI_3$ based solar cell was introduced. For all solar cells made in this thesis, $MAPbI_3$ was used as the photo absorber, poly[bis(4-phenyl)(2,4,6-trimethylphenyl)amine] (PTAA) was used as the hole selective material, fullerene (C_{60}) was used as the electron selective material, bathocuproine (BCP) was used as hole blocking material, indium tin oxide (ITO) and copper (Cu) were used as electrode materials. The whole structure was glass/ITO/PTAA/$MAPbI_3$/C_{60}/BCP/Cu. Third, the characterization methods were introduced. The E_g and E_t of $MAPbI_3$ were obtained by analyzing the data from modulated surface photovoltage (SPV) spectra. The qualitative analysis and quantitative analysis of DMSO in $MAPbI_3$ layers were performed by IRSE and HR-CSAS. The morphologies of $MAPbI_3$ layers were characterized by scanning electron microscope (SEM). The short-circuit current density (J_{SC}), open-circuit voltage (V_{OC}), fill factor (FF) and PCE of $MAPbI_3$ based solar cells were measured via current density-voltage (J-V) characteristics. The external quantum efficiency (EQE) was also measured.

The results of studying the influence of three factors on $MAPbI_3$ layers and solar cells were shown and discussed in **Chapter 4**. In the experiments of this chapter, N,N-dimethylformamide (DMF) and dimethyl sulfoxide (DMSO) were mixed and used as the solvent. The DMF/DMSO ratio was varied from 12:1 to 4:1, the substrate temperature was varied from 20 to 60 ℃, and the time of vacuum-assisted treatment was varied from 10 to 600 s. From the results, all these factors showed different influence on $MAPbI_3$ layers. Taken together, the decreasing DMF/DMSO ratio, increasing substrate temperature and vacuum-assisted treatment time all showed negative impacts on the performance of $MAPbI_3$ based solar cells. When applying the LaMer model, the reason could be attributed to the competition of nucleation and crystal growth which affected the crystallization and then affected the film qualities. The electronic properties such as E_g and E_t were also influenced. A solar cell with the highest efficiency of 17.8% was based on the $MAPbI_3$ layer prepared at the optimized conditions (9:1, 30 ℃, 10 s).

In **Chapter 5**, the out-diffusion of solvents depending on different post annealing time and temperature was studied. By using HR-CSAS and IRSE, the residual solvent was determined. However, when the $MAPbI_3$ layer was post annealed at higher temperature or longer time, the amount of residual solvent reduced. Based on the detected residual amount at different time and temperature and the Fick's second law, an out-diffusion model was established for DMSO in $MAPbI_3$. Besides, analysis results showed that the out-diffusion of DMSO was limited by two different active energies which related to the formation of $MAPbI_3$. Similar analysis was also made for the out-diffusion of DMF, but there was no clear result due to its relative small amount and low stability. It was shown that solar cells based on the $MAPbI_3$ with less residual DMSO and larger out-diffusion rate had higher PCE. A PCE of 20.2% was obtained when using the $MAPbI_3$ layer post annealed at 120 ℃ in a short time.

The conclusions are summarized in **Chapter 6**. A short outlook on the use of the vacuum-assisted treatment method for other perovskite and further study for solvent out-diffusion in perovskite layers is given.

2. Fundamentals of hybrid organic-inorganic metal halide perovskites (HOIPs)

In this chapter, fundamentals of hybrid organic-inorganic metal halide perovskites (HOIPs) are introduced whereas focus is set on crystal structures, optical and electronic properties of $MAPbI_3$ (it is sometimes written as $CH_3NH_3PbI_3$). Furthermore, architectures of perovskite solar cells and preparation methods for perovskite films are briefly reviewed.

2.1 Crystal structures of HOIPs

The perovskite-group materials are a series of compounds having crystal structures related to the mineral perovskite $CaTiO_3$ [11]. The general chemical formula of perovskite materials is ABX_3, i.e. A = Ca, B = Ti and X = O for $CaTiO_3$.

The ideal unit cell of the perovskite structure is a face centered cube (Figure 2.1 (a)). In this cube, the vertex positions are occupied by 8 cations of A, the centers of the cubic faces are occupied by 6 anions of X the center of the cube is occupied by a cation of B. One cation of B forms with the 6 anions of X an octahedron (coordination number of the cation of B is 6). A perovskite can be described by a structure in which the $[BX_6]$ octahedra are connected to each other in corner-sharing to form a three dimensional framework (see Figure 2.1 (b)). In this structure, the center of 8 connected $[BX_6]$ octahedral is occupied by a cation of A. The centers of the cube edges around a cation of A are occupied by anions of X. Therefore, the coordination number of a cation of A is 12. An anion of X is surrounded by 4 cations of A and 2 cations of B (coordination number 6). In HOIPs, the organic cations such as methylammonium ion ($CH_3NH_3^+$) or formamidinium ion ($CH(NH_2)_2^+$) occupy the A site, metal cations such as lead ion (Pb^{2+}) or tin ion (Sn^{2+}) occupy the B site and the halogen anions such as chloride (Cl^-), bromide ion(Br^-) or iodide ion (I^-) occupy the X site.

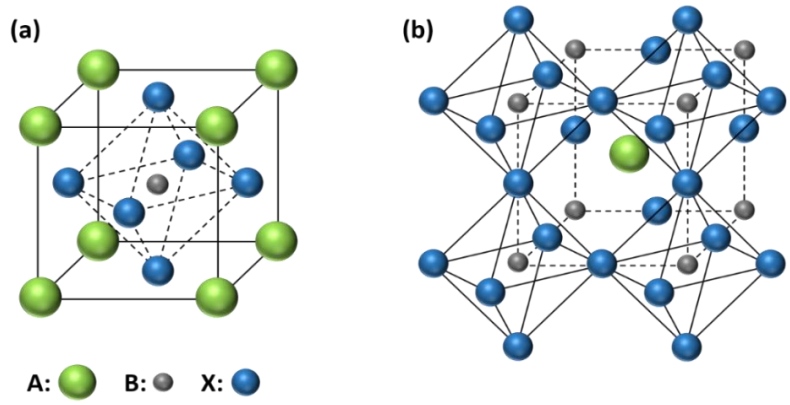

Figure 2.1. Outline of the ideal structure of perovskite that has unit cell with face-centered cubic stucture (a) and three dimensional framework of corner-sharing [BX_6] octahedra with cation A occupying the twelve-coordinate site in between the polyhedral.

Usually, perovskites in nature do not show the ideal cubic structure due to distortions [12]. Distortions can be caused, for example, by not matching radii of ions or by different energy lowering in electronically degenerate systems (Jahn-Teller effect [13]). Not matching radii of ions are described by the so-called tolerance factor. The radii of ions of A, B and X are given by r_A, r_B and r_X, respectively. Figure 2.2 (a) illustrates schematically a unit cell with the fcc structure for a set of values of r_A, r_B and r_X.

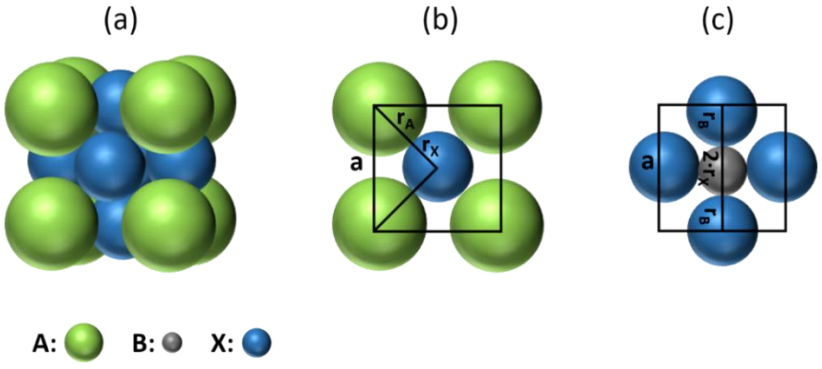

Figure 2.2. Schematic unit cell of the fcc structure for a set of ion radii (a) and cuts through the AX (b) and BX (c) planes.

The radii of the ions of A, B and X touch each other (see Figures 2.2 (b) and (c) for the cuts through the AX and BX planes, respectively). For a fcc structure, the lattice constant (a) can

be calculated from the values of $r_B + r_X$ and $r_B + r_x$ regarding to the following equation:

$$a = \sqrt{2} \cdot (r_A + r_X) = 2 \cdot (r_B + r_X) \qquad (2.1)$$

The Goldschmidt's tolerance factor (t) is defined as [14]:

$$t = \frac{r_A + r_X}{\sqrt{2} \cdot (r_B + r_X)} \qquad (2.2)$$

The value of t is equal to 1 for the fcc structure. This is the case for $SrTiO_3$ (r_A=1.44 Å, r_B=0.605 Å, and r_x=1.40 Å) [12]. However, in most cases, the value of t is not equal to 1. This has consequences for the symmetry and the formation of a perovskite structure. For example, the range of t for cubic perovskite formation is $0.89 < t < 1$ [15-16], the range of t for alkali metal halide perovskite formation is $0.813 < t < 1.107$ [17] and the range of t for HOIPs formation (A site was MA^+ or FA^+, B site was Pb^{2+}, Sn^{2+} or Ge^{2+} and X site was Cl^-, Br^- or I^-) is $0.912 < t < 1.142$ [18]. For $MAPbI_3$, the value of t is equal to 0.91 (r_{MA^+} = 217 pm, $r_{Pb^{2+}}$ = 119 pm, r_{I^-} = 220 pm) [19]. Note that the Goldschmidt's tolerance factor is rather an empirical approach to predict the stability and the accuracy of prediction is only about 75% [20].

In perovskites, given ions of A, B and X can be partially replaced by other ions of type A, B and X (mixing). This causes a change of t, and, by varying the stoichiometry, t can be adjusted. However, one should keep in mind that local variations of disorder in the arrangement of ions can cause phase segregation.

2.2 Phase transitions of HOIPs

Based on X-ray diffraction (XRD) techniques, cubic, tetragonal, trigonal and orthorhombic crystal structures of perovskites were distinguished [21-22]. The cubic, tetragonal, trigonal and orthorhombic phases are often denoted by α, β, γ and δ whereas several phases can appear within one crystal structure. Phase transitions of perovskite materials can be caused by changes in temperature, pressure or composition. As an example, table 2.1 gives an overview of the temperature ranges for phases in $MAPbI_3$, $MAPbBr_3$, $FAPbI_3$ and $MASnI_3$.

HOIPs undergo in general several phase transitions in the solid state depending on temperature, pressure and composition.

Table 2.1 Phase transitions of some HOIPs (data after ref [23-29]).

Perovskite	Phase	Temperature (K)	Crystal system	Lattice (Å)
$MAPbI_3$	α	>327.4	cubic	a=6.3285
	β	162.2-327.4	tetragonal	a=8.855 c=12.659
	γ	<162.2	orthorhombic	a=8.861 b=8.581 c=12.620
$MAPbBr_3$	α	>236.9	cubic	a=5.901
	β	155.1-236.9	tetragonal	a=8.322 c=11.832
	γ	149.5-155.1	tetragonal	a=5.894 c=5.861
	δ	<144.5	orthorhombic	a=7.979 b=8.580 c=11.849
$MASnI_3$	α	293	tetragonal	a=6.2302 c=6.2316
	β	200	tetragonal	a=8.7577 c=12.429
$FAPbI_3$	α	293	trigonal	a=8.9817 c=11.006
	β	150	trigonal	a=17.791 c=10.091

$MAPbI_3$ exists in cubic, tetragonal and orthorhombic phases in the temperature (T) ranges T > 327.4 K, 162.2 K < T < 327.4 K and < 162.2 K, respectively. Incidentally, solar cells can reach temperatures above 327.4 K under operation, i.e. $MAPbI_3$ undergoes phase transitions in solar cells under operation. In our experiments, measurements were performed at room temperature and the temperature of solar cells was fixed at 25℃ for measurements with a cooling stage, i.e. phase transitions did not occur. In difference to $MAPbI_3$, the compounds $FAPbI_3$, $MASnI_3$ and $MAPbBr_3$ exist only in the trigonal, tetragonal and cubic α phases, respectively, at temperatures above 293, 293 and 236.9 K,

respectively.

The situation is more complicated for mixed ion systems. Furthermore, the formation of phases and phase segregation depends also on the crystallization process. In this work, for example, the influence of residual solvent molecules on properties of only $MAPbI_3$ was investigated, despite the fact that higher PCE have been reached for solar cells based on mixed ion systems. The investigations were focused on the prototypical perovskite $MAPbI_3$ in order avoid the influence of local variations of disorder in the arrangement of ions.

2.3 Optical and electronic properties of HOIPs

2.3.1 Band gaps and optical absorption of HOIPs

The band gap of a photovoltaic absorber (E_g) is the most important parameter for a solar cell since the value of E_g limits the maxima of photo-generation and quasi Fermi-level splitting, i.e. of the short circuit current density and open circuit voltage. Regarding to the Shockley-Queisser limit, the range of E_g is between about 1.0 and 1.6 eV for reaching very high efficiencies above 30% with single junction solar cells. The band gaps of numerous HOIPs are in this range. The values E_g are summarized in Figure 2.3 for some HOIPs.

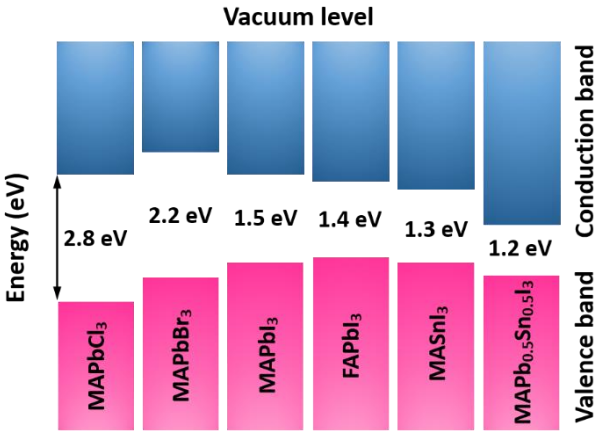

Figure 2.3. Band gaps of different hybrid organic-inorganic metal halide perovskites (data after ref [30-32]).

For example, E_g is equal to about 1.5 eV for $MAPbI_3$. In general, the band gaps decrease

with increasing atomic number of the halogen in ABX_3. For $MAPbX_3$ and X = Cl, Br and I, the values of E_g are equal to about 2.8, 2.2 and 1.5 eV, respectively, i.e. E_g of HOIPs is dominated by the halogen and metal.

The band gap of HOIPs can be additionally varied by mixing ions of type A, B and X. Figure 2.4 shows examples for the specific influence of mixing (A: MA-FA, B: Pb-Sn, X: Br-I). The change of the MA/FA ratio in $MA_{1-x}FA_xPbI_3$ had only weak influence on E_g which varied between 1.51 and 1.61 eV. The value of E_g of $MAPb_{1-x}Sn_xI_3$ changed between 1.17 and 1.55 eV whereas the minimum was around $MAPb_{0.5}Sn_{0.5}I_3$. E_g of $MAPb(I_{1-x}Br_x)_3$ changed between 1.58 and 2.28 eV. For $FAPb(I_{1-x}Br_x)_3$, E_g varied between 1.51 and 2.27 eV.

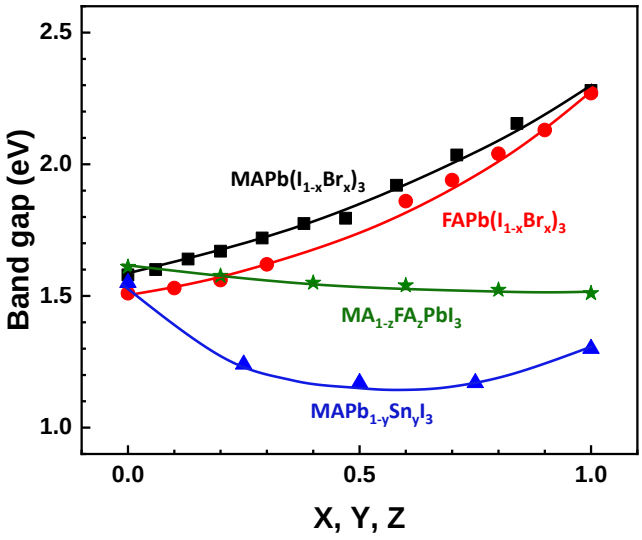

Figure 2.4. Dependence of the band gaps of $MAPb(I_{1-x}Br_x)_3$, $FAPb(I_{1-x}Br_x)_3$, $FAPb_{1-y}Sn_yI_3$ and $MA_{1-z}FA_zPbI3$ on the stoichiometry (data after ref [33-36]).

Ideal photovoltaic absorbers are transparent for photons with energy (hν) below E_g. Above E_g, the absorption coefficient increases with increasing E_g whereas this increase is proportional to $(h\nu-E_g)^{0.5}$ for direct semiconductors [37]. HOIPs are direct semiconductors with a very steep increase of the absorption coefficient [38]. In Figure 2.5, the absorption spectrum of $MAPbI_3$ is compared with the absorption spectra of c-Si and GaAs. On the

logarithmic scale, the onset of absorption of $MAPbI_3$ is nearly as steep as for GaAs. At 100 meV above E_g, the absorption coefficients are about 20, $1x10^4$, $3x10^4$ cm^{-1} for c-Si, GaAs and $MAPbI_3$, respectively. Therefore, the thickness of absorber films for HOIPs based solar cells is of the order of only several hundred nanometers.

Incidentally, the absorption coefficient of $MAPbI_3$ is about 1 cm^{-1} at photon energy of about 1.45 eV. The very low absorption coefficient is caused by absorption due to exponentially distributed tail states near the conduction and valence band edges. The value of the exponential parameter of the so-called Urbach tail (E_t) is about 14–24 meV for $MAPbI_3$ [39] which is significantly larger than for GaAs but much smaller than for disordered semiconductors such as intrinsic amorphous silicon (50–60 meV [40]). As remark, at room temperature, the value of E_t can depend on the substrate, deposition conditions and ion mixing [41]. In general, HOIPs have a nearly ideal transparency for photon energies below E_g.

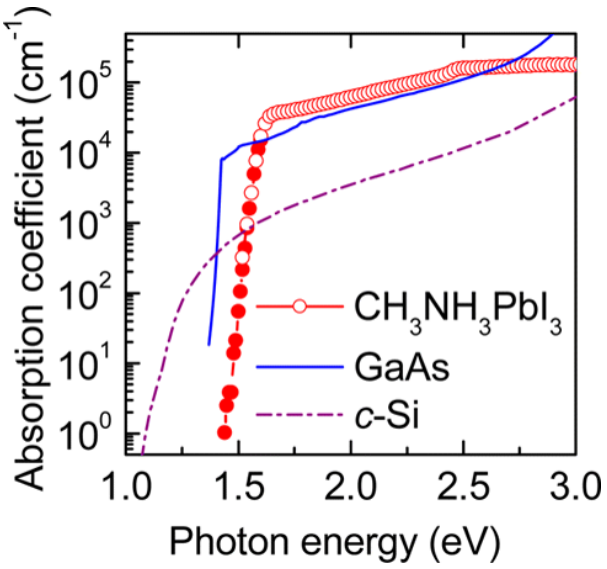

Figure 2.5. Effective absorption coefficient of a $CH_3NH_3PbI_3$ perovskite thin film compared with other typical photovoltaic materials including GaAs and crystalline silicon (c-Si), all measured at room temperature. Reprinted with permission from ref [42]. Copyright (2014) American Chemical Society.

2.3.2 Diffusion length of HOIPs

In semiconductors, charge carriers can be driven by diffusion (driving force: concentration gradient) or drift (driving force: electric field). Diffusion and drift are characterized by the parameters of the diffusion constant (D) and mobility (μ), respectively whereas the mobility is the proportionality factor between the electric field and the velocity of the charge carrier. D and μ are connected via the so-called Einstein relation:

$$D = \mu \frac{k_B T}{q} \qquad (2.3)$$

whereas k_B, q and T denote the Boltzmann constant ($1.38064852 \times 10^{-23}$ m^2 kg s^{-2} K^{-1}), elementary charge ($1.60217662 \times 10^{-19}$ C) and the absolute temperature, respectively.

The diffusion length is defined as the average distance that an excess charge carrier can move between its generation and recombination. Therefore, the diffusion length limits the collection of photo-generated charge carriers in most solar cells. L depends on the D and the carrier lifetime:

$$L = \sqrt{D \cdot \tau} \qquad (2.4)$$

For $MAPbI_3$ layers, L was measured directly by using the steady-state photocarrier grating method and amounted to about 350 nm [43]. For $MAPbI_3$(Cl) layers, L was about 1.5–1.9 μm as shown by electron beam induced current measurements [44]. By using the Goodman method [45], it was shown that L is limited by the grain size in $MAPbI_3$ [46] and that L can achieve values larger than 10 μm in crystalline powders of $MAPbI_3$ [47]. Incidentally, in a $MAPbI_3$ single crystal, a diffusion length as large as 175 μm has been shown [48]. Therefore, $MAPbI_3$ can be prepared with very low densities of recombination active defects. This is unique for solution based deposition technology.

The diffusion length is limited by the crystal size, i.e. the grain size shall be of the order or larger than the thickness of $MAPbI_3$ layers in solar cells (several hundred nm). As an example, Figure 2.6 shows a cross section across a $MAPbI_3$ layer with different grain sizes. It indicates the importance of reducing the number of grain boundaries on the transport path

which can increase the transport length of charge carriers (or effective diffusion length) and reduce non-radiative recombination in the bulk.

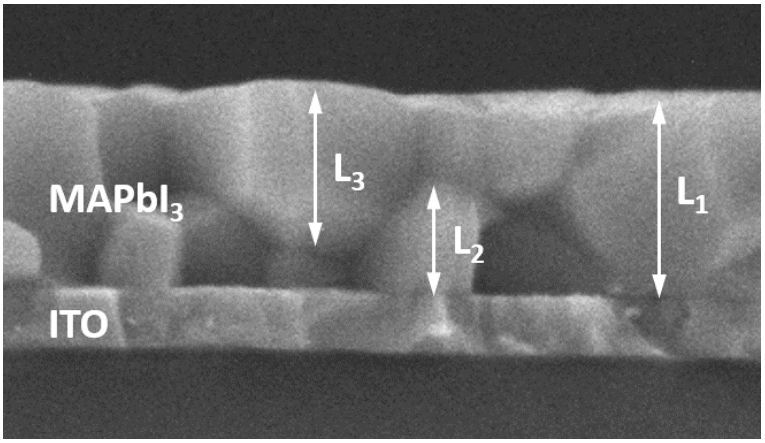

Figure 2.6. Diffusion lengths limited by grain size in crystalline $MAPbI_3$ layer.

2.3.3 Doping of HOIPs and formation of charge-selective contacts

The splitting of the Fermi-energies of electrons and holes in an illuminated photovoltaic (PV) absorber is the first prerequisite for getting a photovoltage in a solar cell. The second prerequisite is the ability to extract photo-generated electrons from an illuminated PV absorber at a high chemical potential (Fermi-energy of electrons, E_{Fn}) and to transfer the electrons back to the PV absorber at a reduced chemical potential (Fermi-energy of holes, E_{Fp}) after passing an external load. The electrons transferred back to the PV absorber recombine with holes.

Solar cells based on crystalline silicon, III-V semiconductors (such as GaAs) can be doped by purpose and charge-selective p-n homo-junctions can be formed. For perovskite, Wang et al. [49] reported that the change of composition in precursor solutions led to variations of p- (excess of MAI) and n- (excess of PbI_2) type. Naikaew et al. [50] observed that the $MAPbI_3$ changed from p- to n-type semiconductor with the appearance of PbI_2 after 90 min annealing at 100 ℃. As so far, the controlled doping for perovskite is impossible. Therefore, in perovskite solar cells, the extraction of electrons at E_{Fn} is realized by electron separation with charge-selective electron contacts, where holes are extracted by separation with

charge-selective hole contacts at E_{Fp}.

Charge separation in a perovskite solar cell is a directed transfer of photo-generated charge carriers from a perovksite absorber across an interface into electronic states of a contacting material (Figure 2.7). The driving force for a directed charge transfer is given by the decrease of the potential energy of transferred mobile charge carriers in their final state, i.e. transferred photo-generated charge have a lower potential energy after the charge transfer than before.

Transferred photo-generated electrons or holes should remain mobile in the contacting material for getting them out to external loads. Mobile electrons and holes in the contacting material are characterized by their Fermi-energies ($E_{F,ce}$ and $E_{F,ch}$). Charge-selective electron or hole contacts act as sinks for photo-generated electrons or holes. In contrast, the transfer of photo-generated holes or electrons should be blocked from the PV absorber into contacting materials of charge-selective electron or hole contacts, respectively. The transfer of photo-generated holes or electrons is blocked by energetic barriers.

In ideal charge-selective contacts, the potential energy of transferred photo-generated electrons (holes) is reduced, transfer of photo-generated holes (electrons) is blocked and $E_{F,ce}$ ($E_{F,ch}$) is aligned with E_{Fn} (E_{Fp}).

For solar cells based on HOIPs, for example, TiO_2 [51], SnO_2 [52], ZnO [53] or C_{60} [54] have been applied for electron selective contacts and spiro-OMeTAD [51], poly(3,4-ethylenedioxythiophene) (PEDOT) [55], PTAA [54], or NiO_x [56] have been applied for hole-selective contacts.

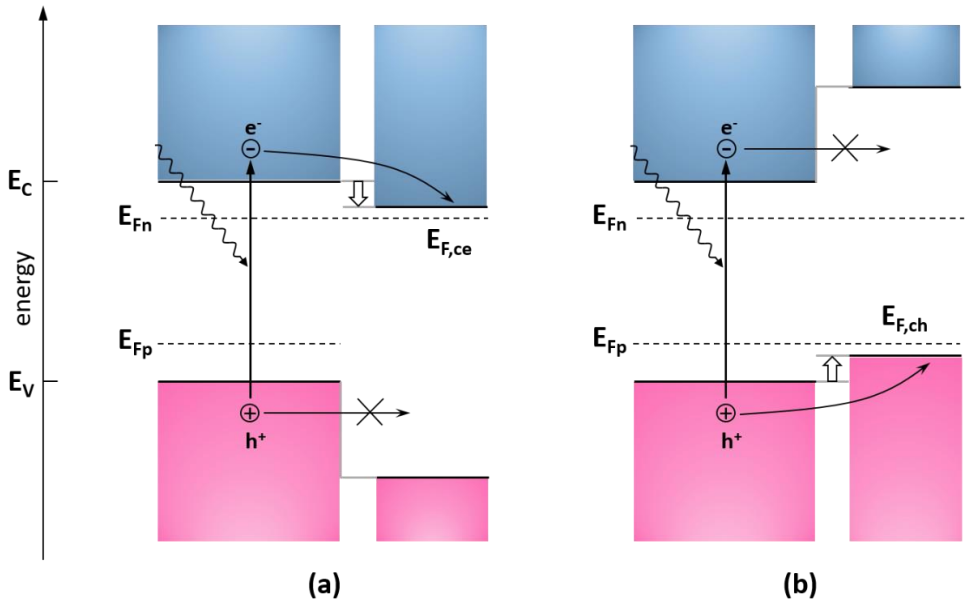

Figure 2.7. Schematic band diagrams of ideal charge-selective electron (a) and hole (b) contacts acting as sinks for photo-generated electrons and holes, respectively. The Fermi-energies E_{Fn} and $E_{F,ce}$ (a) and E_{Fp} and $E_{F,ch}$ (b) are aligned at charge-selective electron and hole contacts. The transfer of photo-generated holes or electrons is blocked from entering contacting material of charge-selective electron or hole contacts, respectively.

2.4 Stability of HOIPs

2.4.1 Stability in air (H_2O and O_2)

In ambient air, there are two components, water (H_2O) and oxygen (O_2), affecting the chemical stability of HOIPs. H_2O can be the catalyst for irreversible degradation. For example, Frost et al. [57] proposed a simple acid−base reaction shown in Figure 2.10. The combination of H_2O and n[$(CH_3NH_3^+)PbI_3$] will lead to the formation of [$(CH_3NH_3^+)_{n-1}(CH_3NH_2)(PbI_3)_n$] [$H_3O$] degrading afterwards into HI, CH_3NH_2, PbI_2, H_2O and n-1[$(CH_3NH_3^+)PbI_3$]. Since both HI and CH_3NH_2 are gases at room temperature, their escape drives continuous degradation. At the end, $MAPbI_3$ is converted into PbI_2.

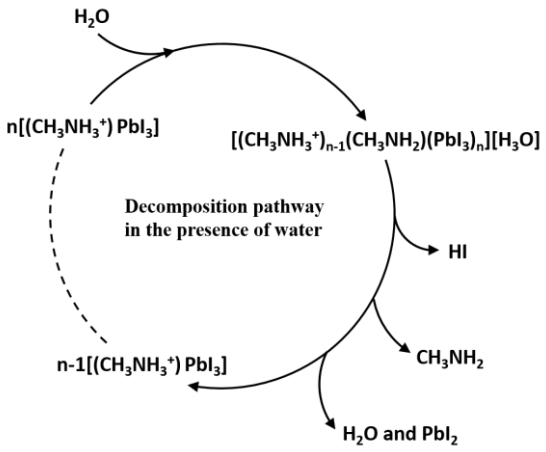

Figure 2.10. Proposed decomposition pathway of $CH_3NH_3PbI_3$, in the presence of water. Reprinted with permission from ref [31]. Copyright (2014) American Chemical Society.

Niu et al. [58] studied the degradation mechanism of $CH_3NH_3PbI_3$ by comparing XRD patterns before and after exposure to H_2O and proposed the following reactions:

$$CH_3NH_3PbI_3(s) \xleftrightarrow{H_2O} PbI_2(s) + CH_3NH_3I\ (aq)$$

$$CH_3NH_3I\ (aq) \longleftrightarrow CH_3NH_2\ (aq) + HI\ (aq)$$

$$4HI\ (aq) + O_2(g) \longleftrightarrow 2I_2(s) + 2H_2O(l)$$

$$2HI\ (aq) \xleftrightarrow{h\nu} H_2(g) + I_2(s)$$

At first, the $CH_3NH_3PbI_3$ degrades into PbI_2 (s) and CH_3NH_3I (aq) in presence of H_2O. Then the CH_3NH_3I further decomposes into CH_3NH_2 (aq) and HI (aq). HI can be oxidized forming I_2 and H_2O. It can also produce H_2 and I_2 under photodecomposition. The consumption of HI drives the whole decomposition process.

The role of O_2 in the degradation of $CH_3NH_3PbI_3$ was studied by Aristidou et al. [59]. They proposed a possible reaction scheme for the degradation shown as follows:

$$CH_3NH_3PbI_3 \xleftrightarrow[\text{no moisture}]{\text{light}} CH_3NH_3PbI_3{}^*$$

$$O_2 \xleftrightarrow{CH_3NH_3PbI_3{}^*} O_2^-$$

$$CH_3NH_3PbI_3 + O_2^- \xleftrightarrow{\text{deprotonation}} CH_3NH_2 + PbI_2 + 1/2I_2 + H_2O$$

Firstly, optical excitation results in the formation of $CH_3NH_3PbI_3$*, which carries both photo-generated electrons and holes. Secondly, superoxide (O_2^-) is generated through electron transfer from $CH_3NH_3PbI_3$* to O_2. Finally, under the attack of the resulting O_2^-, the deprotonated $CH_3NH_3PbI_3$ decomposes into CH_3NH_2, PbI_2, I_2 and H_2O. It is noteworthy that the generated H_2O can further accelerated the degradation.

2.4.2 Photo stability

As with some other solar cells such as organic solar cells, dye sensitized solar cells and c-Si solar cells [60-62], degradation can happen in perovskite solar cells under illumination. In perovskite solar cells, TiO_2 is one of the most commonly used electron transporting materials. However, it is also a photocatalyst sensitive to UV light. Leijtens et al. [63] showed a degradation of $CH_3NH_3PbI_3$ in TiO_2 based solar cells, which was most likely caused by the UV light. In this research, part of devices were encapsulated to get rid of the impact from ambient air and were compared with the devices without encapsulation.

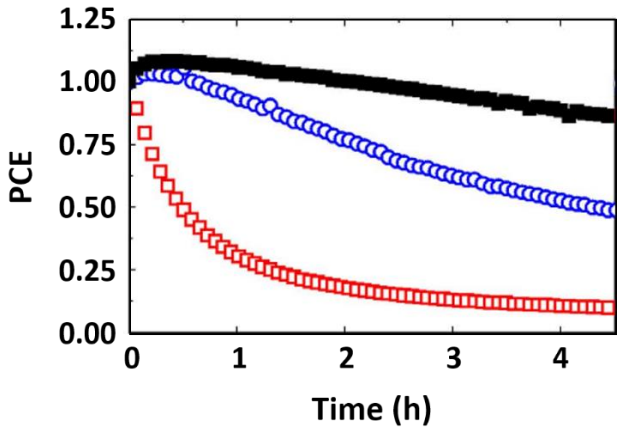

Figure 2.11. Power conversion efficiency (PCE) degradation curves of TiO_2 based $CH_3NH_3PbI_3$ solar cells which are non-encapsulated (blue open circles) and encapsulated with (filled black squares) and without a<435 nm cutoff filter (open red squares). Reprinted with permission from ref [37]. Copyright (2017) Springer Nature.

As shown in Figure 2.11, the PCE of the encapsulated device decreased within few hours, when UV light was not filtered. In order to explain this, they proposed a degradation

mechanism. At first, an electron-hole pair is formed in TiO_2 upon the band gap excitation. Then the hole in valence band recombines with the electron at the O_2 adsorption site causing desorption and leaving positively charged trap state and a free electron in the conduction band. The excess holes from spiro-OMeTAD layer recombine with these free electrons. The adsorbed O_2 will cause a degradation of $CH_3NH_3PbI_3$.

Wojciechowski et al. [64] compared the photo stability of $CH_3NH_3PbI_3$ on TiO_2 with that on fullerene (C_{60}). It was shown that J_{SC} of TiO_2 or C60 based device decreased by more than 50 or 10 %, respectively, after an initial small increase. It was assumed that this difference was related to the presence or absence of O_2 desorption caused by UV illumination. Furthermore, Tang et al. [65] supposed that photo-degradation of $CH_3NH_3PbI_3$ was heavily influenced by defects. For example, iodine vacancies are generated in $CH_3NH_3PbI_3$ films when the $CH_3NH_3^+$ ions are lost in vacuum. The degradation mechanism was proposed as follows:

$$\mathrm{CH_3NH_3PbI_3} \xrightarrow{\text{vacuum}} \mathrm{CH_3NH_2(g) + HI(g) + PbI_2 + V_I^-}$$

$$\mathrm{e + V_I^-} \xrightarrow{\text{trapped}} \mathrm{e(V_I^-)}$$

$$\mathrm{e(V_I^-) + Pb^{2+} \longrightarrow Pb^+ + 2I^- + V_{Pb}^{2+}}$$

$$\mathrm{2Pb^+ \longrightarrow Pb^0 + Pb^{2+}}$$

$$\mathrm{h + V_{Pb}^{2+}} \xrightarrow{\text{trapped}} \mathrm{h(V_{Pb}^{2+})}$$

$$\mathrm{2h(V_{Pb}^{2+}) + 2I^- \longrightarrow I_2}$$

During vacuum degradation, volatile CH_3NH_3I was formed together with iodine vacancies (V_I^-) which can trap photo-generated electrons. Trapped electrons caused the reduction of neighbor Pb^{2+} to Pb^+, and two Pb^+ further reacted to form Pb^0 and Pb^{2+}. The formed Pb vacancies in crystals trapped photo-generated holes and then oxidized I^- to I_2. The whole reaction can be written as:

$$\mathrm{2CH_3NH_3PbI_3} \xrightarrow[\text{light}]{\text{vacuum}} \mathrm{2CH_3NH_2(g) + 2HI(g) + PbI_2 + Pb + I_2(g)}$$

In conclusion, there are several proposed mechanisms for photo degradation. But the degradation is usually a result of comprehensive effect of several factors. Further studies of photo degradation mechanism need be done.

2.4.3 Thermal stability

In normal operation conditions, the temperature of solar cells will increase under illumination. So the thermal stability of perovskite solar cells should also be considered. The cumulative temperature can be as high as 85 ℃ if the environmental temperature is 40 ℃ [66]. There are two kinds of thermal degradation in device, one is from the perovskite material and another comes from other unstable layers. Here we only talk about the intrinsic thermal stability of perovskite itself. Conings et al. [67] studied the thermal stability of $CH_3NH_3PbI_{3-x}Cl_x$ and found that the perovskite degraded at 85 ℃ in N_2. The calculated formation energy of unit cell in $CH_3NH_3PbI_{3-x}Cl_x$ was 0.11-0.14 eV and the thermal energy (0.093 eV) calculated at 85 ℃ was close to that. Thus degradation at 85 ℃ was expected. By using thermogravimetric analysis for $CH_3NH_3PbX_3$ (X = I or Cl), Dualeh et al. [68] found that the organic component of perovskite was decomposed to HI and CH_3NH_2 leading to a subsequent degradation. Phillippe et al. [69] used hard X-ray photoelectron spectroscopy to investigate the influence of temperature on both $CH_3NH_3PbI_3$ and $CH_3NH_3PbI_{3-x}Cl_x$ films. They proposed the following reaction for thermal degradation:

$$CH_3NH_3PbI_3 \xrightarrow{\text{heat}} CH_3NH_2(g) + HI(g) + PbI_2$$

Furthermore, Pisoni et al. [69] studied the thermal conductivity of $CH_3NH_3PbI_3$. Their research showed that thermal conductivity of $MAPbX_3$ was very low in both monocrystals and polycrystalline layers. That led to heat accumulation inside the perovskite and resulted in thermal degradation.

2.5 Vapor and solution based preparation of HOIPs

Hybrid organic-inorganic metal lead halide perovskites can be prepared by different deposition routes. There are two main precursor components: an organic halide salt (such as

MAX or FAX, X = Cl, Br, I) and a metal halide salt (such as PbX_2, X = Cl, Br, I). These preparation methods (Figure 2.12) can be categorized into three routes of processing based on evaporation in vacuum, deposition of precursor salt solutions, and hybrid.

In the work of Liu et al. [71], high performance solar cells (PCE>15%) were made by vacuum deposition (Figure 2.12 (a)), where the organic and inorganic species were co-evaporated to form uniform planar perovskite films. Later, Chen et al. [72] performed a sequential vapor deposition of $PbCl_2$ followed by CH_3NH_3I on the substrate with temperatures between 65 and 85 ℃ which enhanced the penetration of CH_3NH_3I into $PbCl_2$. Besides, this method shows the advantage of preparing multi-stack thin films over large areas [73].

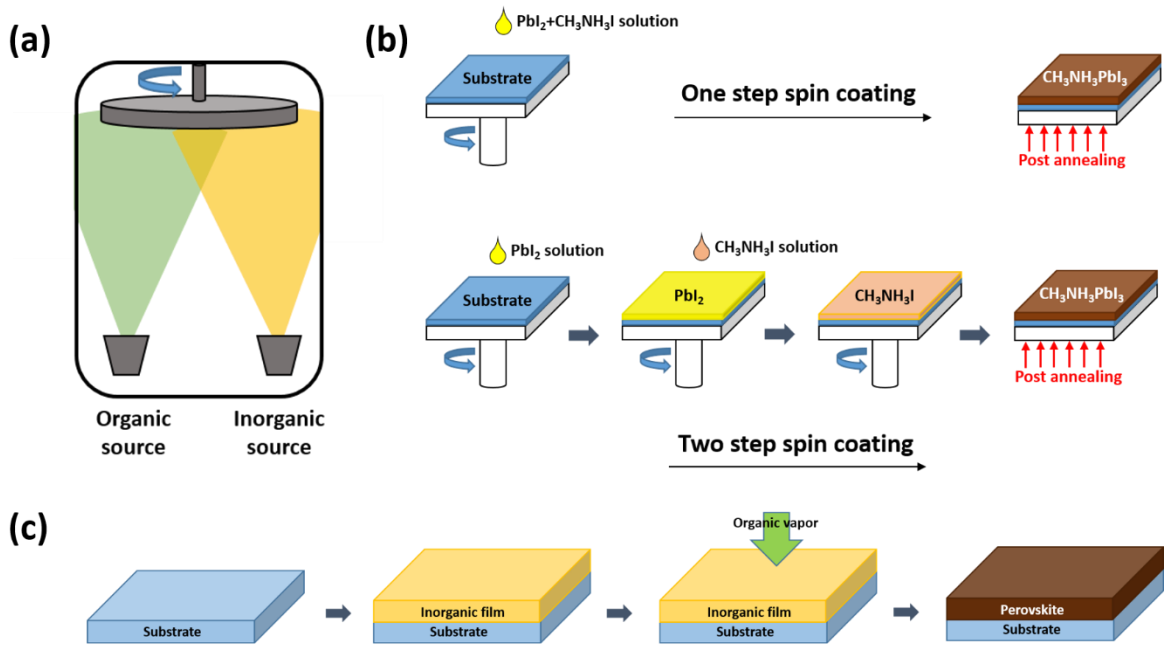

Figure 2.12. Different deposition methods for perovskite films: vacuum deposition (a), one step and two step spin coating solution processes (b), and vapor-assisted solution process using organic vapors to react with pre-deposited metal halide films (c).

Solution processing technique for perovskite film preparation is the most prominent method due to simplicity and low energy consumption for suitable mass production. With solution process, perovskite such as $MAPbI_3$ can be deposited on substrates via two routes. The

most commonly used method as so far is depositing a mixed solution containing CH_3NH_3I and PbI_2, also called one step preparation method. In this route, the precursor solution can be spread on substrates in several ways such as spin coating (Figure 2.12 (b)), doctor blading or printing. For removing the solvent from the formed precursor solution layer, there are also several techniques. The most commonly used one is called anti-solvent dripping which was firstly reported by Jeon et al. [9]. In their works, toluene was used as an anti-solvent (which cannot dissolve CH_3NH_3I and PbI_2) to wash away the solvent, γ-butyrolactone (GBL) and dimethylsulphoxide (DMSO), immediately during spin coating. Then extremely uniform and dense perovskite layers formed via a CH_3NH_3I–PbI_2–DMSO intermediate phase and the fabricated solar cells had a certified PCE of 16.2%. Conings et al. [74] invented the universal complex-assisted gas quenching technique, which introduces a nitrogen gas flow to take away residue solvent to form an intermediate DMSO-complex, and they applied this technique to many perovskite materials. Through this method, an efficiency of 18.0% was obtained. A vacuum flash-assisted solution process (VASP) was developed by Li et al. [75] for high-efficiency and large-area perovskite solar cells. Shiny, smooth and crystalline perovskite films with high electronic quality formed from the DMSO-$PbI_{1.7}Br_{0.3}$-$(FAI)_{0.85}(MABr)_{0.15}$ intermediate prepared by VASP. The fabricated perovskite solar cells with an aperture area exceeding 1 cm^2 showing a maximum PCE of 20.5% and a certified PCE of 19.6% was achieved.

Another route is called two step preparation method, where a metal halide salt (such as PbI_2) layer and an organic halide salt (such as CH_3NH_3I) layer are successively deposited by spin coating or dipping and then form a $CH_3NH_3PbI_3$ layer via reaction. Burschka et al [51] first developed a two-step method, in which PbI_2 was introduced onto a porous TiO_2 film and subsequently converted into the perovskite by exposing it to CH_3NH_3I solution, which yielded a perovskite film with a good film quality and a PCE of 15% in a mesoporous device. After that, an inter diffusion method was introduced by Xiao et al. [76], which combined a sequence spin coating of PbI_2 and CH_3NH_3I, then conversion into perovskite film, which yielded a 15.4% PCE in a planar device.

Based on these techniques, the hybrid method, which combines both solution and vapor processes, was first proposed and developed by Chen et al. (Figure 2.12 (c)) [77]. A PbI_2 layer was first deposited by spin coating, followed by a reaction of the pre-deposited PbI_2 film with CH_3NH_3I vapor. The compact layer featured a polycrystalline texture of large grains over 1 μm with small surface roughness. Leyden et al. [78] used a similar vapor deposition method, where CH_3NH_3I vapor was reacted with a pre-deposited $PbCl_2$ film, resulting in a highly stable and scalable perovskite film.

2.6 Solar cells based on HOIP absorbers

2.6.1 Architectures of single-junction perovskite solar cells

The widely used architectures of single junction perovskite solar cells can be catalogued into mesoporous scaffold and planar heterojunction structures. In the mesoporous scaffold structure which inherited from DSSCs (Figure 2.13 (a)), metal oxide nanoparticles, such as titanium oxide (TiO_2) or aluminium oxide, (Al_2O_3) are applied to form mesoporous scaffold, into which the perovskites are infiltrated. It is noticeable that different nanoparticles have different functions in the structure. For mesoporous TiO_2 layer, it assists the electron transporting between the perovskite and electrode [79]. The perovksite solar cells based on the mesoporous TiO_2 structure has reached an efficiency of 23.2% [80]. A further intriguing advancement in mesoporous scaffold structure has been achieved by Lee et al. [81] when they replaced the mesoporous TiO_2 with inert mesoporous Al_2O_3. Although Al_2O_3 was not directly involved in electron transporting mechanism, the incorporation of Al_2O_3 imparted surpassing optoelectronic features to the perovskite [82]. One more advantage associated with the replacement of TiO_2 with Al_2O_3 is that one can improve the stability under UV illumination [63].

On the other hand, benefitting from the high charge carrier mobilities and long diffusion lengths, perovskite solar cells can also afford a planar heterojunction configuration. Liu et al. [71] established that mesoporous scaffold is not a requisite to achieve high efficiencies for perovskite solar cells. The planar devices include regular (n-i-p) (Figure 2.13 (b)) and

inverted (p-i-n) (Figure 2.13 (c)) devices, depending on which charge-selective contact is used atop of the transparent electrode. Yu et al. [83] applied a TiO_2/C_{60}-SAM double-layer as ETL in a regular planar structure, a PCE of 19.7% was obtained. The efficiencies of pervoskite solar cells with inverted structures are already over 21% [84]. It is worth noting that the current best performing devices usually reported involve mesoporous scaffold devices; albeit, recently, the efficiencies of planar devices have also improved over 23% [85], and also the fabrication of planer devices is relatively easier compared to the mesoporous devices.

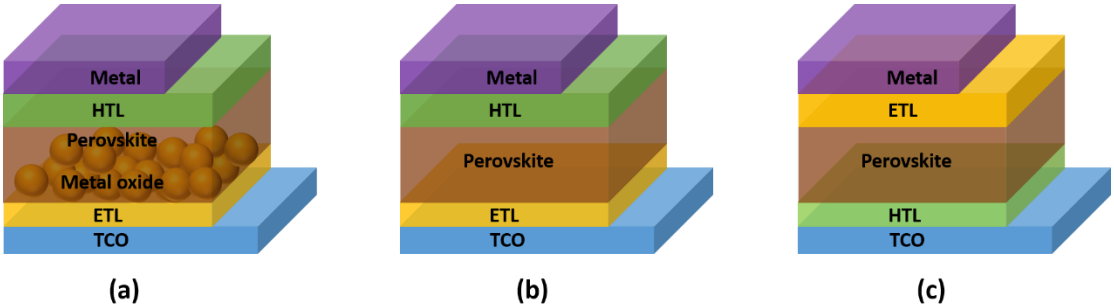

Figure 2.13. Device architectures of mesoporous scaffold, regular (n-i-p) and inverted (p-i-n) planar heterojunction perovskite solar cells. Electron transporting layer (ETL) is used to form electron-selective contact with perovskite and hole transporting layer (HTL) is used to form hole-selective contact with perovskite. The light is incident on the transparent conductive oxide (TCO).

2.6.2 Architectures of multi-junction perovskite solar cells

Except the researches on single-junction perovskite solar cells, the studies of multiple-junction (tandem) solar cells, is believed to be an effective strategy for reaching higher efficiencies as it theoretically allows the Shockley–Queisser limit in single junction devices. In tandem solar cells, photons with high or low energies can be selectively harvested by the front or rear cells with different band gaps which also reduce the thermal loss. Because of the tunable band gaps between 1.17 and 2.3 eV [35], [86], perovskites can be used in constructing tandem devices with themselves, or with a variety of semiconductors, such as silicon, CIGS and organic semiconductors. Theoretical predictions suggest that the

peak efficiency for the mechanically stacked tandem is 37.2% and for the monolithic tandem when combed with a 1.6 eV perovskite solar cell and a Si solar cell is 29.4% [87].

The tandem solar cells containing perovskites can be fabricated in two types of configuration based on how the junctions are electrically coupled between the top and bottom cell. The mechanically stacked solar cell is called as 4-terminal (4T) tandem and the monolithic tandem solar cell is called as 2-terminal (2T) tandem. Their structures are shown in Figure 2.14. In 4T tandems, the top and bottom cells are fabricated independently and are then mechanically stacked upon each other (Figure. 4(a)), this kind of structure offers more flexibility during processing. However, when comparing with 2T tandems, the extra transparent electrodes in 4T devices result in additional absorption losses. In monolithic 2T tandems, two sub-cells are electrically connected through a transparent internal electrode (Figure 4(b)). The 2T architecture requires only one external circuit and only one substrate support which reduces the production cost. The challenges of the 2T tandems include the development of a charge recombination layer and the sophisticated multi-layer fabrication, as well as the optimization of the sub-cell thickness to ensure the current match in between for reaching high efficiencies.

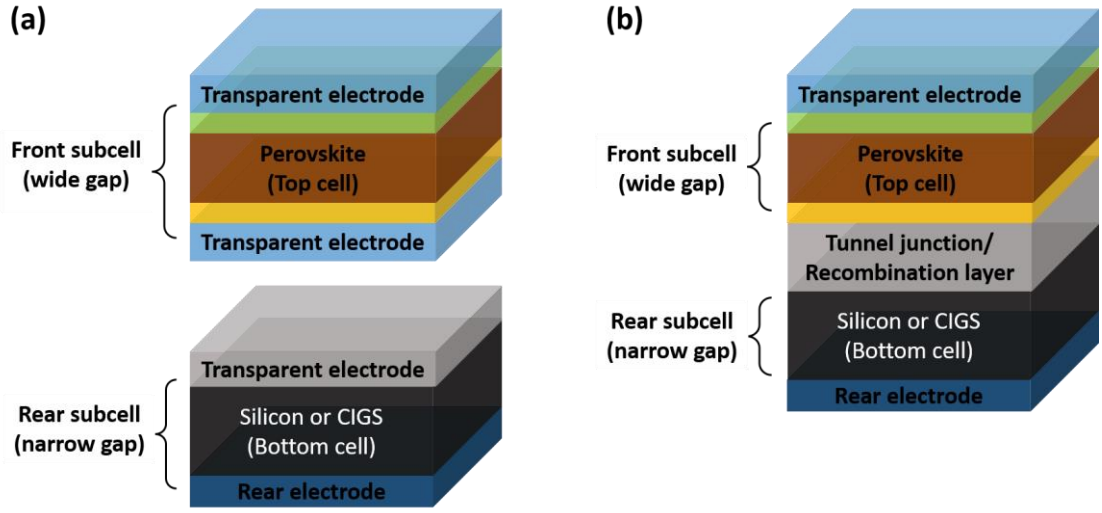

Figure 2.14. Schematic showing: (a) 4-terminal (4T) and (b) 2-terminal (2T) tandem perovskite solar cells.

As stated, perovskite tandem solar cells mainly consist of perovskite solar cells with wide band gap and other solar cells with narrow band gap. Generally, for rear cells in perovskite tandems, silicon is the most commonly used narrow band gap material. McMeekin et al. [34] demonstrated the feasibility of achieving PCE>25% for 4T tandem solar cells when using $Cs_{0.17}FA_{0.83}Pb(I_{0.6}Br_{0.4})_3$ with a band gap of 1.75 eV in the top cell and combining it with a 19%-efficiency silicon bottom cell. Jost et al [88] reported perovskite/silicon 2T tandem solar cells with PCEs>25% which employ a textured light management foil. In addition, perovskites can also be applied in rear cells with narrow band gaps. For instance, Yang et al. [89] developed $MA_{0.5}FA_{0.5}Pb_{0.75}Sn_{0.25}I_3$ with a band gap of 1.33 eV in a rear cell, and when it was combined with $MAPbI_3$ as a top cell, a 4T tandem device with a PCE of 19.08% could be achieved. Eperon et al. [90] developed an infrared absorbing perovskite, $Cs_{0.25}FA_{0.75}Pb_{0.5}Sn_{0.5}I_3$, which had a band gap of 1.2 eV and was applied in a rear cell. When combining it with a top cell which contained $Cs_{0.17}FA_{0.83}Pb(I_{0.5}Br_{0.5})_3$ with a band gap of 1.6 eV, the PCEs of 17% and 20.3% were obtained from 2T and 4T tandem solar cells respectively.

2.7 Conclusions

In summary, this chapter has presented a basic introduction of HOIPs especially $MAPbI_3$. Due to the crystal structure and mixing ions, the band gap of HOIPs can be varied at the range of 1.2–2.8 eV, which including a range of band gaps for achieving high efficiencies in solar cells. HOIPs have high absorption coefficients and long carrier diffusion lengths which are crucial for reaching high efficiencies. Furthermore, the grain size of polycrystalline HOIPs layers shall be of the order or larger than the thickness of the HOIP absorber layer for getting highest efficiencies. Meanwhile, the density of pinholes in HOIPs layers should be as low as possible to avoid local shunts. Previous studies showed that long term stability of HOIPs is still challenging, for example, due to reactions caused by H_2O and O_2, light (especially UV) and heat. Encapsulation of HOIP layers or solar cells is necessary when sample are exposed, for example, to air for times longer than several hours or days, depending on the conditions. Usually, samples without encapsulation stored in a

glovebox can be stable, with regard to the structure, even for several months. Incidentally, changes in electronic properties can appear faster. For relatively short measurement times, instabilities can be ignored. Moreover, as HOIPs cannot be doped on purpose, charge-selective contacts are required for extracting and transporting the photo-generated charge carriers. A p-i-n charge-selective system can be formed (HTM/HOIP/ETM). In our experiments, two organic semiconductors, PTAA and C_{60}, were used for hole and electron selective contacts, respectively.

3. Materials and methods

In this chapter, the materials, experimental methods and setup are introduced. This includes, (1) the preparation of $MAPbI_3$ layers, (2) the characterization of the morphology and electronic properties, (3) the detection of residual solvent in $MAPbI_3$ layers, (4) the fabrication and characterization of $MAPbI_3$ based solar cells.

3.1 Film and device preparation

3.1.1 Equipment of vacuum-assisted treatment

When using the solution method to prepare perovskite films, the formation of the intermediate phase plays an important role during the perovskite crystallization. Figure 3.1 depicts the general preparation procedure of the $MAPbI_3$ layers including the vacuum-assisted treatment. First, a thin layer of precursor solution was formed on a substrate by spin coating. Second, the intermediate phase layer was formed during the vacuum-assisted treatment. Third, the multi-crystalline perovskite layer was obtained after post annealing.

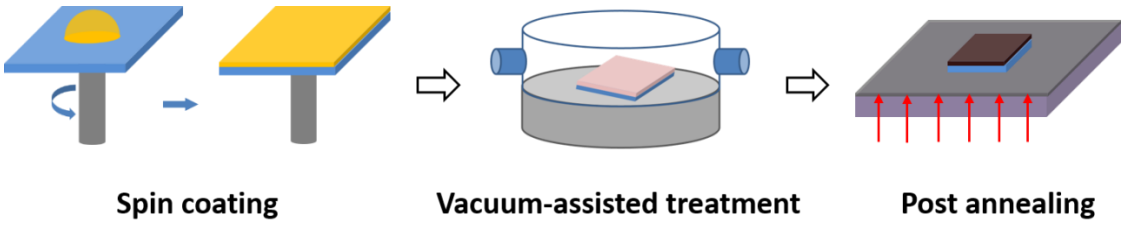

Figure 3.1. Schematic of the general preparation procedure of perovskite films with vacuum-assisted treatment.

The setup developed in our lab for the vacuum-assisted treatment is shown in Figure 3.2. Unlike the equipment of reported vacuum-assisted treatment which were handled in air environment [75, 91-92], our equipment allows to prepare the perovskite films in N_2 atmosphere protecting the perovskite from O_2 and H_2O. The principle scheme of the setup is given in Figure 3.2 (a). A small vacuum chamber (Figure 3.2 (b)) was integrated into a glovebox (MBraun) where all treatments were performed. The small vacuum chamber (63

mm inner diameter, VACOM) was based on a window flange connected with a ring and a planar bottom flange. The total volume of the small vacuum chamber was about 56 cm³. A Peltier element (40x40 mm²) was gently pressed on the bottom flange in order to control the temperature at the surface of the Peltier element. The temperature was measured with a Pt100 resistance and controlled with a Peltier controller (Thermocool, TC2812-RS232). In the experiments, this temperature was changed between 20 and 60 °C.

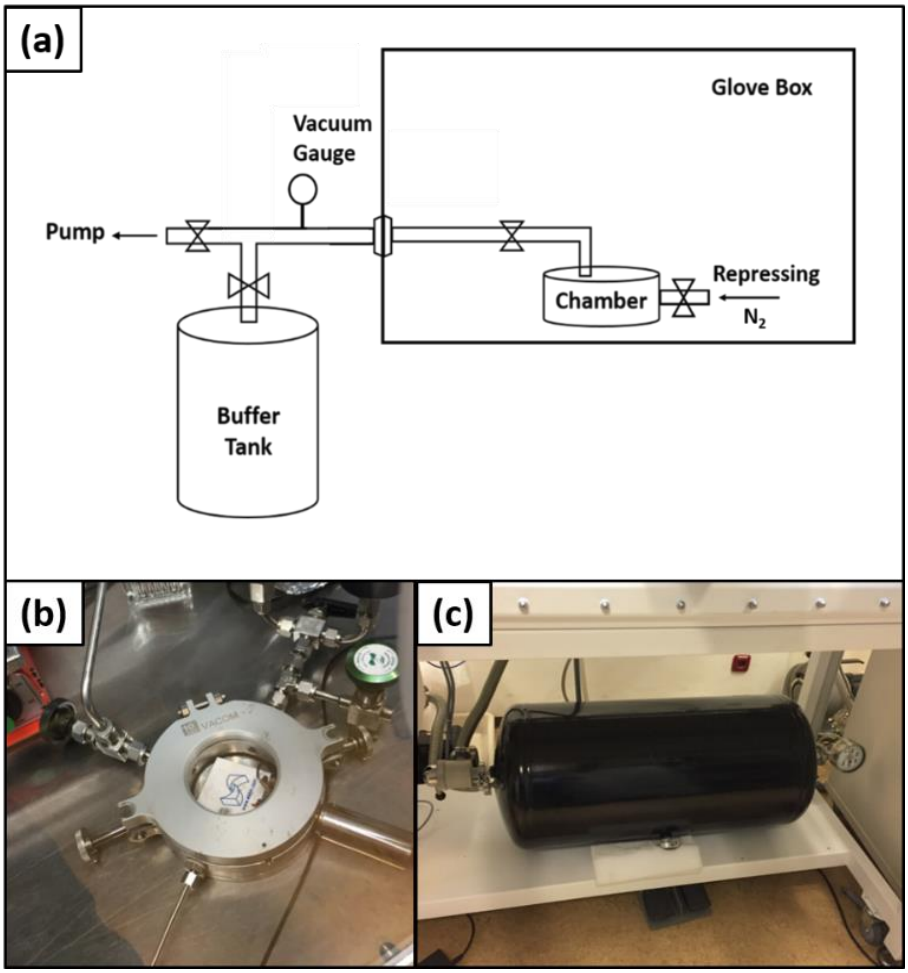

Figure 3.2. Sketch of the setup for vacuum-assisted treatment (a), small vacuum chamber for vacuum-assisted treatment in the glovebox (b), buffer tank for the vacuum-assisted treatment outside the glovebox (c).

The small vacuum chamber had connections to the atmosphere in the glovebox or to the vacuum system with the buffer tank by two separate valves. The vacuum system included the small vacuum chamber, a rotary vacuum pump (Pfeiffer, DUO 5 M), a vacuum buffer

tank (Figure 3.2 (c)) with a volume of 1.06×10^5 cm ^{3}and a vacuum gauge (Pfeiffer Balzers TPG 251 single gauge). The base pressure of the buffer tank was 1.8 Pa. Then, in ideal condition, a low pressure value of about 54 Pa will be reached in the small vacuum chamber after connecting it with the evacuated buffer tank following the equation:

$$P_1 \cdot V_1 + P_2 \cdot V_2 = P_3 \cdot (V_1 + V_2) \qquad (3.1)$$

This equation was deduced from the ideal gas law. P_1 was the initial pressure of the buffer tank, P_2 was the initial pressure of the small vacuum chamber (about normal pressure), and P_3 was the pressure in both chambers after being connected. V_1 was the volume of buffer tank and connecting pipe (about 1.08×10^5 cm^3) and V_2 was the volume of the small chamber. The measured pressure was about 60 Pa when connecting the evacuated buffer tank with the small vacuum chamber after 1-2 s. The pressure further decreased to about 30 Pa within one min and continued to decrease further with increasing time due to the connected vacuum pump.

For the vacuum-assisted treatment operation, the tank was firstly pumped to the base pressure while the valve between the tank and small chamber was kept closed. The temperature of the Peltier element surface was controlled at a setting value. Then the sample with a formed precursor layer was transferred into the small chamber immediately after spin coating within 2 s and the connecting valve was opened. The whole time between the end of spin coating and reaching 60 Pa in the small chamber was 5 – 6 s. After finishing the treatment time in vacuum, the connecting valve to the buffer tank was closed and the valve connecting the small chamber with the glovebox was opened for repressing. Finally, the sample was taken out and put onto a hot plate for post annealing.

3.1.2 Preparation of $MAPbI_3$ layers

Depending on the characterization, the substrates of $MAPbI_3$ layers were grouped as shown in Table 3.1. The fully covered or patterned ITO glass (SnO_2:In coated on glass) substrates (sheet resistance of 15 Ω/sq, Automatic Research, size 2.5x2.5 cm^2) were cleaned in an ultrasonic bath by washing subsequently in soap water, deionized water, acetone and

isopropanol for 15 min. Then the substrates were dried with a N_2 flow and cleaned with ozone for 15 min. Residual organics were removed by the ozone cleaning. For a 100 nm Au layer deposition, Au was evaporated with a evaporation rate of 1 Å/s at the vacuum degree of $7x10^{-5}$ Pa. For PTAA layer deposition, PTAA (99%, Sigma Aldrich) was spin coated (4000 rpm for 30 s) from a toluene (anhydrous, 99.8%, Sigma Aldrich) solution (2 mg/mL) and annealed at 100 ℃ for 10 min in N_2 atmosphere (glovebox).

Table 3.1. Substrates used for the different characterization methods (HR-CSAS: high resolution continuous source absorption spectrometry, SEM: scanning electron microscopy, SPV: modulated surface photovoltage spectroscopy, solar cells: current-voltage characteristics at AM1.5, IRSE: infrared spectroscopic ellipsometry).

Substrates	Characterization
glass/ITO	HR-CSAS
glass/ITO/PTAA	SEM, SPV
glass/patterned ITO/PTAA	solar cells
glass/ITO/Au/PTAA	IRSE

The 1 M precursor solution was prepared by dissolving PbI_2 (99.99%, TCI) and CH_3NH_3I (99%, dyenamo) with the molar ratio of 1:1 in the mixed solvent of DMSO (anhydrous, ≥99.9%, Sigma Aldrich) and DMF (anhydrous, 99.8%, Sigma Aldrich). Then the solution was stirred at 60 ℃ overnight. Then the precursor solution was spin coated onto the prepared substrate at 3000 rpm for 7 s to form a precursor layer. After vacuum-assisted treatment and post annealing, a dark-brown $MAPbI_3$ perovksite layer formed. During the vacuum-assisted treatment and post annealing, some parameters including the solvent ratio, the substrate temperature during vacuum-assisted treatment (T_{vac}, taken as the surface temperature of the Peltier element), the time of sample exposing in vacuum (t_{vac}), the temperature (T_{ann}) and the time (t_{ann}) of post annealing were varied to study their influence on $MAPbI_3$ layers and solar cells. The post annealing was performed on a preheated hot plate. Figure 3.3 shows the temperature calibration of the hot plate, i.e. the evolution of the

temperature at the surface of a dummy sample for different annealing temperature. The annealing temperature was reached in the experiments within 15–20 s. Therefore, it was reasonable to start the experiments with the annealing time of 1 min.

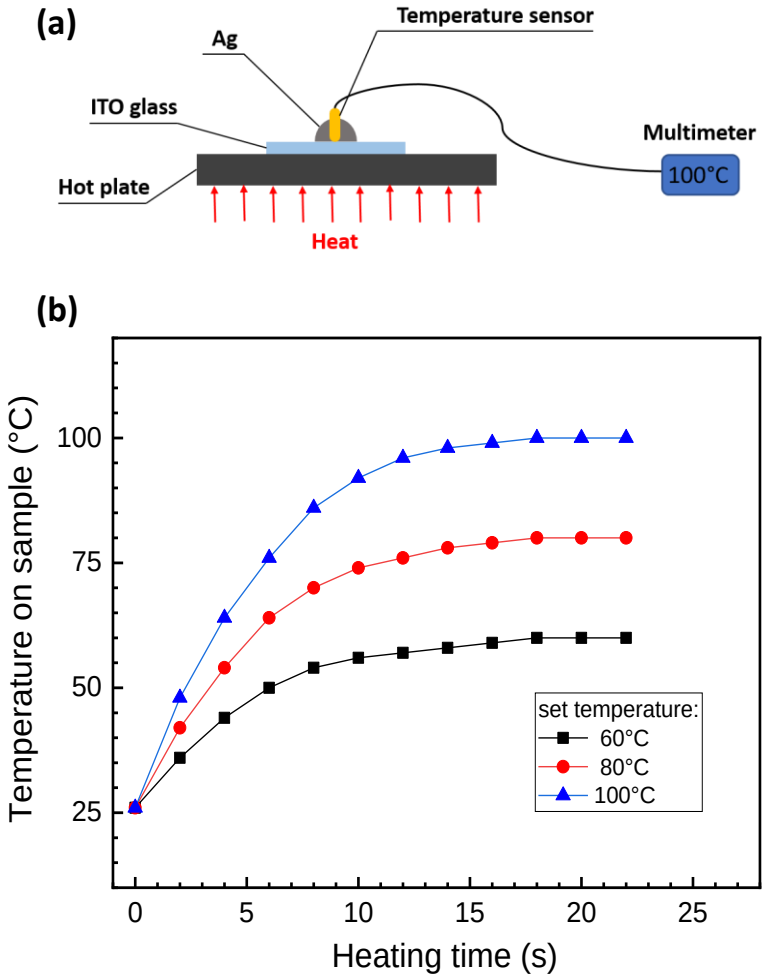

Figure 3.3. Setup for the temperature measurement (a) and temperature calibration of a sample on the hot plate for annealing set-temperatures of 60, 80 and 100 ℃ (b).

Table 3.2 gives the overview of the parameter variations for the different series of experiments. Incidentally, samples were prepared on different substrates for each series with regard to the requirements of the given characterization techniques (Table 3.1).

Table 3.2 Overview of varied parameters of vacuum-assisted treatment and post annealing.

Series number	DMF:DMSO (volume ratio)	T_{vac} (℃)	t_{vac} (s)	T_{ann} (℃)	t_{ann} (min)
1	12:1 9:1 8:1 7:1 6:1 4:1	30	60	100	10
2	9:1	20 30 40 50 60	60	100	10
3	9:1	30	10 30 60 120 300 600	100	10
4	9:1	30	60	60	150
				80	60
				100	10
				120	5
5	9:1	30	60	100	1 2 4 6 8 10 15 30

3.1.3. Fabrication of perovskite solar cells

All the perovskite solar cells in this thesis were prepared with the same structure (See Figure 3.4). In the solar cells, the PTAA layer and the C_{60} layer were used as hole transporting layer and electron transporting layer, respectively. The BCP layer played a role of hole blocking layer. The ITO and Cu layers were used as anode and cathode, respectively.

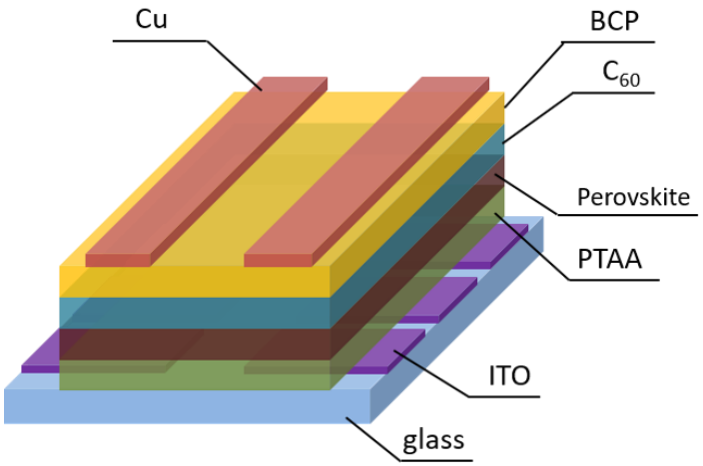

Figure 3.4. Schematic drawing of the $MAPbI_3$ perovskite solar cells.

The PTAA and $MAPbI_3$ layers were prepared as described above. A C_{60} (99.5%, Sigma Aldrich) layer with a thickness of 23 nm was evaporated at 350 ℃ with a rate of 0.1 Å/s. Then an 8 nm thin BCP (99.99%, Sigma Aldrich) layer was evaporated at 130 ℃ with a rate of 0.2 Å/s. Finally, a 100 nm Cu layer was evaporated with a rate of 1 Å/s. For all thermal evaporation steps, the pressure in the evaporation chamber was about $7x10^{-5}$ Pa. The size of the glass substrate was 25x25 mm^2. The areas and shapes of ITO layer and Cu layer are shown in Figure 3.5. Each substrate had 6 pixels of solar cells and the active area was 4x4 mm^2 for each cell.

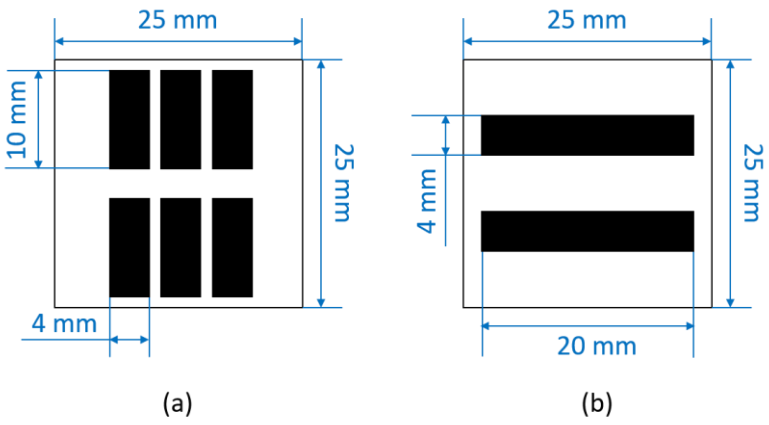

Figure 3.5. Sketch maps of ITO layer (a) and Cu layer (b).

3.2 Modulated surface photovoltage (SPV) spectroscopy

3.2.1 Principle of SPV

A surface photovoltage (SPV) arises when photo-generated charge carriers are separated in space. Therefore, SPV techniques are effective methods to investigate photo-generated charge carrier separation in layers by detecting the change in the surface dipole [93-97]. SPV can be used as a non-destructive, contactless and surface-sensitive tool to analyze electronic properties of semiconductor materials such as transition energies. Processes of charge separation, transport and recombination can be studied by SPV. In our experiments, we applied the modulated SPV spectroscopy to measure the band gap (E_g) and the parameter of the exponential tails close to E_g (E_t) of the $MAPbI_3$ layers prepared under different conditions.

As shown in Figure 3.6 (a), SPV signals are measured between the sample and the reference electrodes. Both electrodes are connected with a measurement resistance (R_m). Therefore the Fermi levels of these two electrodes can be aligned via electrons flow. The difference between the work functions of the sample electrode (W_S) and the reference electrode (W_{ref}) is defined as the contact potential difference (CPD). Under illumination, the incident light causes a change in surface dipole and therefore work function of the sample electrode results in a change of CPD (ΔCPD, see Figure 3.6 (b)). The light induced voltage between the electrodes (V_S) is equal to -ΔCPD and is

the surface photovoltage signal.

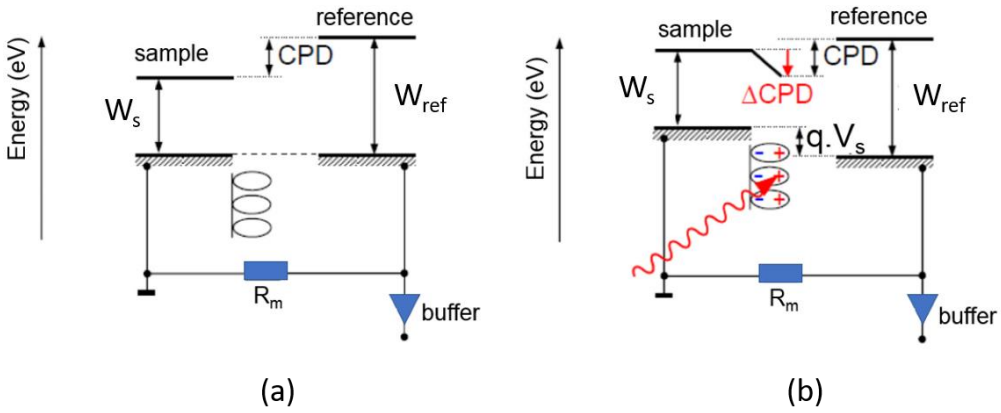

Figure 3.6. Energy schemes of a sample electrode with a surface layer and reference electrode in the dark (a) and under illumination (b). Both the electrodes are connected by a measurement resistance. The reference electrode is connected to a high impedance buffer. The work functions of the sample and reference electrodes are W_s and W_{ref}, respectively. The contact potential difference (CPD), the light induced change of the CPD (ΔCPD) and the light induced voltage between the electrodes (V_s) are indicated.

The SPV signal V_S is equivalent to the potential at a charged parallel plate capacitor [98], which can be written by the following equation:

$$V_s = \frac{Q \cdot d_s}{\varepsilon_0 \cdot \varepsilon} \qquad (3.2)$$

As shown, V_S is proportional to the distance between the centers of positive and negative charge carriers (d_s). Q is the amount of separated charge carriers in space obtained by integration of photo-generated charge carriers of the same sign over the thickness of the investigated layer. The two constants are vacuum permittivity (ε_0= 8.85×10^{-12} F/cm) and permittivity (ε) respectively.

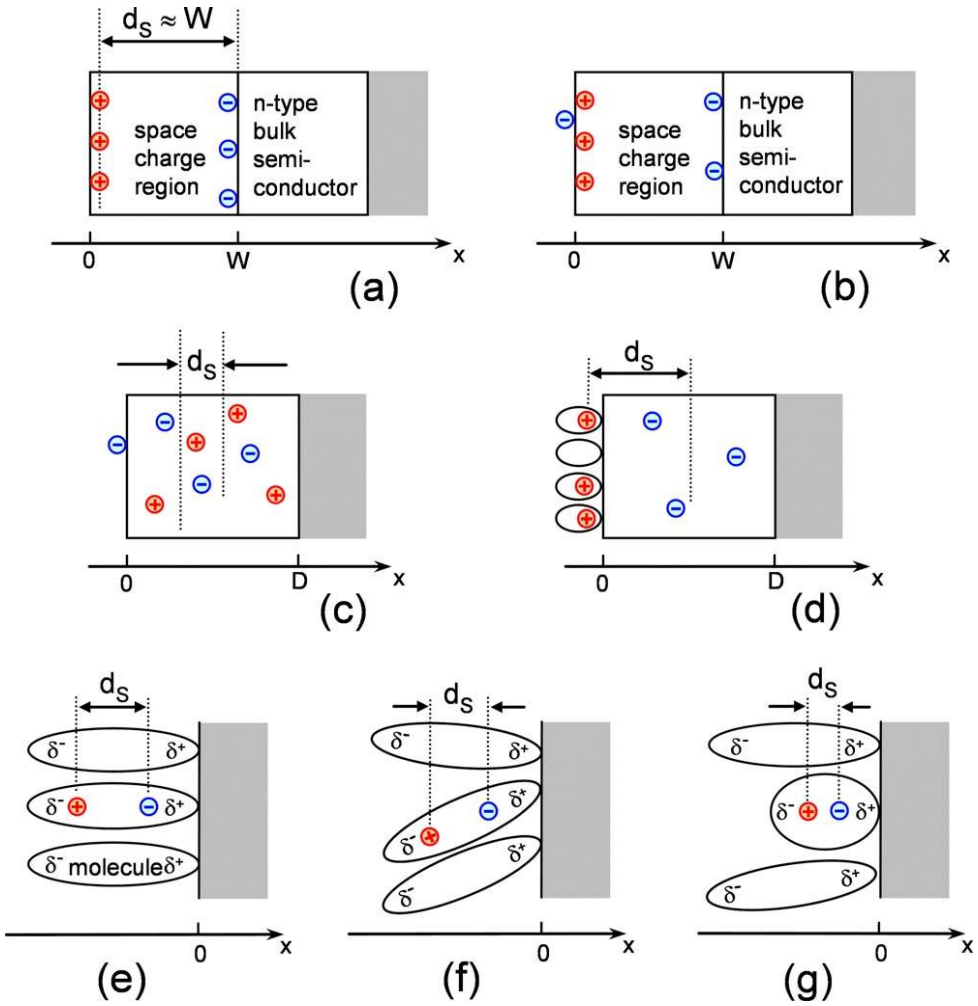

Figure 3.7. Illustration of mechanisms of charge separation [charge separation in a space charge region of a doped semiconductor (a), preferential trapping at surface states in the cases of a space charge region (b) and absence of a space charge region (c), surface sensitization with dye molecules and injection of charge carriers (d), light induced change of polarization of molecules (e), light induced change of orientation disorder (f), and light induced reconfiguration of molecular structures (g)]. Reprinted from ref [99], with the permission of AIP Publishing.

Figure 3.7 gives an overview of processes leading to charge separation. The most frequent process is the charge separation in a surface space charge region of a semiconductor with a width of the space charge region (W) which can change from the nanometer to the micrometer ranges. Depending on the measurement conditions, the value of d_s is close to W (a). Charge can be trapped at semiconductor surface

states, for example, at a crystalline Si surface, leading to a charge separation in space (b). Furthermore, asymmetric trapping and different diffusion coefficients of mobile positive and negative charge carriers can cause SPV signals (c). The value of d_S is usually much smaller than the layer thickness D. The injection of charge carriers causes a SPV signal when insulators are sensitized, for example, with dye molecules (d). The value of d_S is limited by the thickness of the blocking layer. The polarization of adsorbed molecules changes under illumination and can be detected as a SPV signal (e). The value of d_S depends on the size of a molecule and on internal charge transfer. The orientation disorder (f) or restructuring of adsorbed molecules (g) caused by a change in polarization may also affect the behavior of d_S.

For the SPV measurements on $MAPbI_3$ layers, (a) is the dominating mechanism. There are few defects at the $MAPbI_3$ surface. And considering the sample structure (glass/ITO/PTAA/$MAPbI_3$), charge transfer (injection or internal photoemission) via excitation from PTAA can be neglected as there is very small (nearly no) hysteresis **[100-101]** in the prepared solar cells.

3.2.2 Band gap and exponential tails analysis by low signal modulated SPV spectroscopy

The SPV spectroscopy performed with examining modulated illumination at low light intensities (usually the order of tens of $\mu W/cm^2$) is called low signal modulated SPV spectroscopy. The sign of modulated SPV signals gives the direction of modulated charge separation. A positive SPV signal is measured for separation of electrons towards the sample electrode whereas a negative SPV signal is obtained when electrons are separated towards the sample surface.

In modulated SPV measurements with a double phase lock-in amplifier, the in-phase signals (x signals) and phase-shifted by 90 ° signals (y signals) are distinguished. The x and y signals correspond to the sine or cosine of the modulated signals, respectively.

The amplitude of modulated SPV signals (R) is defined as:

$$R = \sqrt{x^2 + y^2} \qquad (3.3)$$

The phase angel (φ) is defined as:

$$\varphi = \arctan\frac{y}{x} \qquad (3.4)$$

Analysis can be made for x, y and R signals.

As mentioned before, the SPV signal is proportional to the charge separation length. For $MAPbI_3$ layers with built-in electric fields, the width of the space charge region will be disturbed due to the modulated photo-generation. But if this disturbance is much smaller than the width, the error can be ignored, and the charge separation distance can be assumed as a constant. Besides, the SPV signal is also proportional to the amount of separated charge carriers. For the analysis of the E_g and E_t, the amount of separated charge carriers shall be proportional to the amount of absorbed photons when meeting the following conditions: (1) Low signals depend linearly on the light intensity. (2) Charge separation length and/or diffusion length are (much) smaller than the absorption length which is the case near E_g. (3) No change of SPV sign, i.e. the phase angle is nearly constant (no change of the charge separation mechanism).

For E_g analysis, the nature of E_g is considered in the analysis of the so-called Tauc plot. This method of determining E_g was introduced by Tauc who demonstrated that amorphous germanium has an indirect transition in its optical absorption spectrum **[102]**. For a semiconductor with a direct band gap, the Tauc plot is found from the extrapolation of the linear region of the squared spectrum normalized to the photon flux to the axis of the photon energy (see Figure 3.8 (a)). If there is only one mechanism of charge separation and relaxation, the distribution of exponential defect states below the band gap can be analyzed by dividing the SPV amplitude by the photon flux (Φ). The value of E_t was obtained by fitting the leading edge of the SPV amplitude normalized Φ with an exponential function also called Urbach plot **[103]** (see

Figure 3.8 (b)).

$$\frac{\mathrm{R}}{\Phi} = B \cdot exp(\frac{hv - E_g}{E_t}) \qquad (3.5)$$

Where B is a proportionality factor, *hv* is the photon energy.

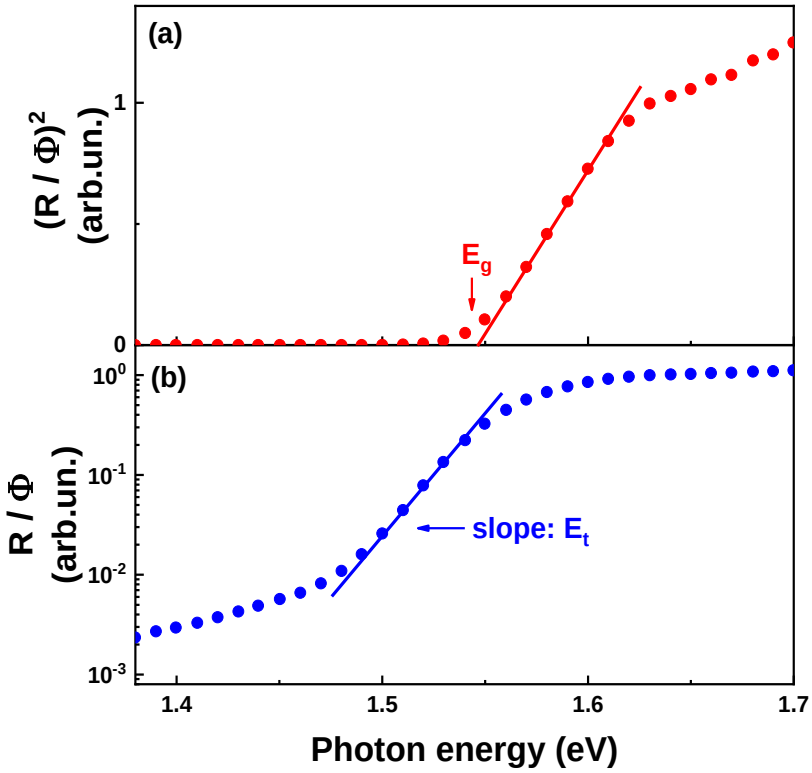

Figure 3.8. Analysis of the band gap with Tauc plot (a) and of the exponential tails with Urbach plot (b) for a direct semiconductor.

3.2.3 Setup for modulated SPV spectroscopy

Figure 3.9 shows a schematic of the setup for SPV measurement in the fixed capacitor arrangement [104]. The change of the surface potential is measured with a capacitor. The sample is one of the electrodes of the capacitor, and the other electrode is composed of a quartz cylinder coated by SnO_2:F. A mica sheet (30 µm) is placed between these two electrodes as a dielectric layer. The light of a halogen lamp (100 W) is directed into a monochromator. The photon energies are adjusted with a quartz prism monochromator (SPM2). The exciting light is modulated with a mechanical

chopper (modulation frequency 16 Hz) resulting in alternating variation of the SPV signals. The SPV signals were coupled with a high impedance buffer (input resistance 50 GΩ) and measured with a double phase lock-in amplifier (EG&G 5210).

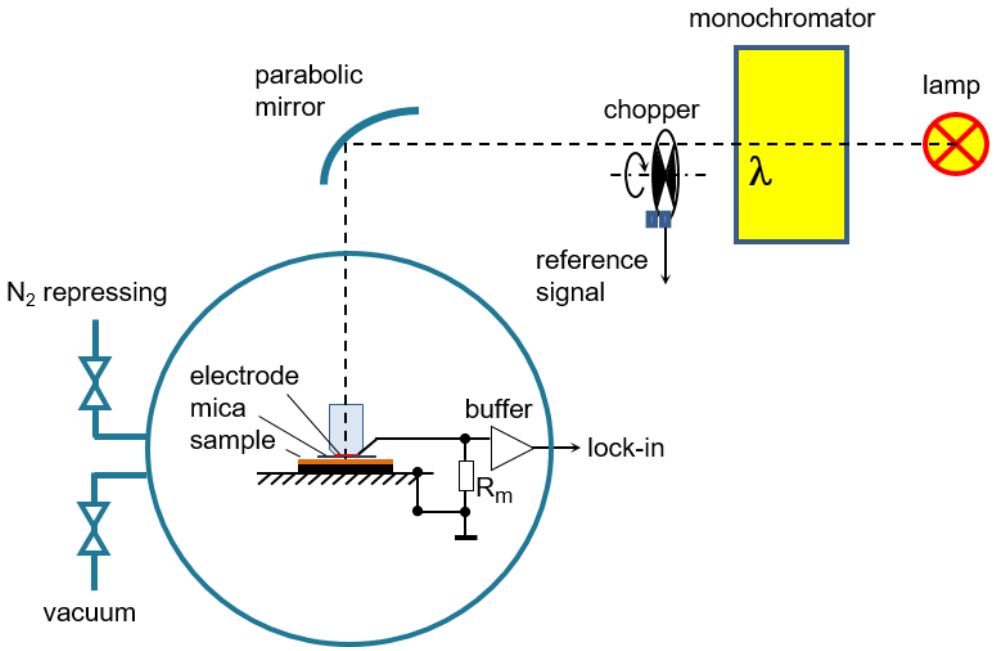

Figure 3.9. Schematic of the setup configuration for surface photovoltage measurements in the fixed capacitor arrangement.

The measurement capacitor with the sample and the high-impedance buffer with the powering battery were placed into a homemade SPV chamber in order to reduce the noise level (100 – 300 nV). For SPV measurements, a certain series of samples was monolithically prepared in the glovebox where each sample was enclosed into a separate sample box (closed). After the depositions, the modulated SPV measurements were performed on each sample of the given series within the same day. After taking out a sample box from the glovebox, the given sample was placed immediately into the SPV chamber, which was then evacuated to vacuum and filled with nitrogen atmosphere (base pressure $7x10^4$ Pa).

3.3 High-resolution continuum source absorption spectrometry (HR-CSAS)

3.3.1 Principle of HR-CSAS

High-resolution continuum source atomic/molecular absorption spectrometry uses the basic principle of atomic absorption spectrometry (AAS). It makes use of the atomic/molecular absorption spectrum of a sample in order to assess the concentration of specific analytes within it. It requires standards with known analyte content to establish the relation between the measured absorbance and the analyte concentration and relies therefore on the Lambert – Beer Law [105].

In brief, the electrons of the atoms/molecules can be promoted to higher orbitals (excited state) for a short period of time (nanoseconds) by absorbing a defined quantity of energy (radiation of a given wavelength). This amount of energy is specific for a particular electron transition in a particular element. The width of an absorption line is only of the order of a few picometers (pm), which gives the technique its elemental selectivity. Incidentally, a very high spectral resolution can be reached by combining a pre-monochromator with an echelle monochromator [106]. The radiation flux without and with a sample in the atomizer is measured using a CCD detector, and the ratio between the two values (the absorbance) is converted to the analyte concentration or mass using the Lambert – Beer Law.

In HR-CSAS, a continuum radiation source with high intensity in the ultraviolet region (Xe lamp) was used instead of an element-specific line radiation source in traditional AAS [107]. The high light intensity allowed for highly sensitive measurements at high resolution without the need for minimizing the sample dilution [108]. The main advantages of such methodology are: (1) real simultaneous registration of analyte absorption and background; (2) extended dynamic range; (3) improved detection limits; (4) determination of non-metals and halogens; (5) simultaneous element detection during one atomization step.

An example of a HR-CSAS spectrum is shown in Fig. 3.10 illustrating the molecular spectrum of carbon monosulfide (CS). The peak at 258.055 nm belongs to CS molecules. The specific peak at 258.055 nm is integrated for HR-CSAS analysis.

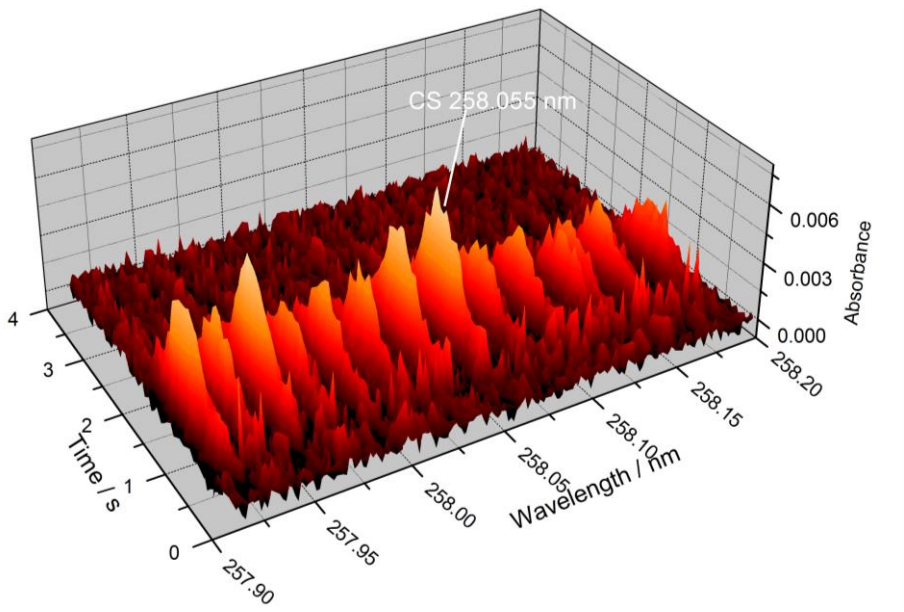

Figure 3.10. Time- and wavelength resolved CS molecular absorption spectrum around 258.055 nm.

3.3.2 Measurement of HR-CSAS

The instrumental concept of HR-CSAS is shown schematically in Figure 3.11. The atomic/molecular absorption measurements were performed in a high-resolution spectrometer system, model contrAA 700 (Analytik Jena AG, Jena, Germany) with a transversely heated graphite furnace. The instrument was equipped with a 300 W xenon short-arc lamp operating in a hot-spot mode as a continuum source for wavelengths from 190 nm to 900 nm, a high resolution double monochromator, consisting of a prism pre-monochromator and an echelle grating monochromator, and a linear CCD-array detector. Pyrolytically coated standard graphite tubes with Pin-platform (Analytik Jena. Part no. 407-A81.025) were used for heating the analyte solution.

The quantification of DMSO is based on the fact the one DMSO molecule contains one sulfur atom (S), and the DMSO is the only S-containing ingredient of the perovskite layer. The determination of S was accomplished by using the CS molecular absorption [109-110]. To reduce the experimental errors caused by the difference between the samples, the Pb in the perovskite layer was also detected by HR-CSAS.

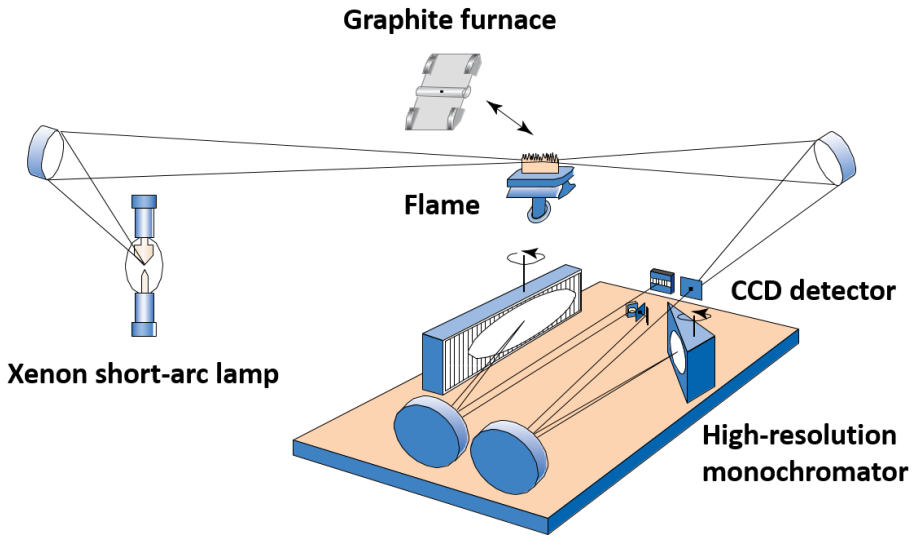

Figure 3.11. Instrumental concept for HR-CSAS. Reprinted from ref [106] with the permission of John Wiley & Sons.

For sample preparation, a $MAPbI_3$ layer on the substrate was washed into a 1.5 ml microcentrifuge tube with acetonitrile. To do this, the substrate was kept inclined for about 45 ° so that the pipetted solvent is slowly spreading on the thin film. For one piece sample (2.5 cm x 2.5 cm) the washing procedure was performed three times using 100 µl acetonitrile each time. After washing, additional 200 µl pure water was added into the microcentrifuge tube. The tube was shortly vortex mixed, and then the total volume of the solution was evaporated to 200 µl at about 35 ℃ heated under a halogen lamp. Finally, 3-5 mg zinc powder was added, and vortex mixed again. The top solution was used for the determination of S. The precipitate was dissolved by using 100 µl nitric acid and diluted to 5 ml with water. This solution was used for the determination of Pb.

For the determination of the amount of S, 20 µl sample solution together with 5 µl palladium modifier solution were charged into the graphite tube. The optimized temperature program used for the S determination is given in Table 3.3. At the high temperature, the DMSO molecules decompose and CS molecules are formed. The CS molecular absorption line at 258.056 nm was used for the determination and quantification of S. Peak volume selected absorbance (PVSA), i.e., integrated absorbance summated over three pixels has been used for signal evaluation. The calibration was accomplished using a calibration curve recorded with aqueous S standard solution made of DMSO.

For the determination of the amount of Pb, 5 µl sample solution were charged into the graphite tube. The optimized temperature program used for the Pb determination is given in Table 3.3. Due to the high concentration of Pb, a weak Pb atomic absorption at 261.418 nm (only 2.1% sensitivity of the Pb line at 217.000 nm) was used for the determination and quantification of Pb. Peak volume selected absorbance (PVSA), i.e., integrated absorbance summated over three pixels has been used for signal evaluation. The calibration was accomplished using a calibration curve recorded with aqueous Pb standard solution.

Table 3.3. Temperature programs used for the generation of CS absorption spectra and for the atomization of Pb in the graphite furnace. S standard solution was made of DMSO. Wavelengths 258.056 nm for CS and 261.418 nm for Pb.

Step	Temperature (℃)	Heating rate (℃/s)	Hold time (s)
Drying 1	90	4	20
Drying 2	110	4	30
Pyrolysis	160 (for CS) 400 (for Pb)	200	10
Vaporization Atomization	2500 (for CS) 1900 (for Pb)	3000	4
Cleaning	2600	1000	3

The S standard solution was prepared by dissolving high-purity DMSO (Sigma Aldrich) in deionized water. Zinc powder with particle size less than 45 μm (pro analysi, Merck, Darmstadt, Germany) was used for reducing and separating the Pb matrix. Nitric acid (65%) of "pro analysi" quality, and palladium matrix modifier were provided by Merck (Darmstadt, Germany). Acetonitrile for ULC/MS was provided by the Biosolv (Valkenswaard, Netherlands). Argon for spectrometry (99.998 % vol.) was supplied by Air Liquid (Berlin, Germany).

3.4 Infrared spectroscopic ellipsometry (IRSE)

3.4.1 Principle of IRSE

Ellipsometry is a robust technique which helps us to accomplish contact free, non-destructive and in-situ studies of surfaces or layers. When combining a Fourier transform spectrometer with a photometric ellipsometer, more information such as electronic band structure and chemical bonds could be obtained [111-112].

As shown in Figure 3.12, when linearly polarized light with a known orientation is reflected at oblique incidence from an interface, it generally becomes elliptically polarized. The new orientation and shape of the ellipse depend on the direction of the polarization of the incident light, the angle of incidence, and the optical properties of the interface. And the light can be classified as two orthogonally polarized components: the paralleled (p) and the perpendicular (s). We assume that the amplitudes of p- and s-components of the incident and reflected light are E_{pi}, E_{si}, E_{pr}, E_{sr}, respectively. Define the reflection coefficients:

$$R_p = \frac{E_{pr}}{E_{pi}}, \quad R_s = \frac{E_{sr}}{E_{si}} \qquad (3.6)$$

Then the ration of the reflectance is:

$$\frac{R_p}{R_s} = \frac{E_{pr}/E_{pi}}{E_{sr}/E_{si}} = \frac{(E_p/E_s)_r}{(E_p/E_s)_i} e^{i(\beta_r - \beta_i)} \qquad (3.7)$$

Where $\beta_i = (\beta_p - \beta_s)_i$ is the phase difference in the incident light, and $\beta_r = (\beta_p - \beta_s)_r$ is the phase difference in the reflected light. Define the amplitude ratio:

$$tan\,\Psi = \frac{(E_p/E_s)_r}{(E_p/E_s)_i} \qquad (3.8)$$

and phase difference change:

$$\Delta = \beta_r - \beta_i \qquad (3.9)$$

then

$$\frac{R_p}{R_s} = \tan\Psi \cdot e^{i\Delta} \qquad (3.10)$$

The Ψ and Δ are called ellipsometric parameters, both of them can be measured independently and experimentally. The availability can help to assign bands by identification of the Kramers–Kronig relations in the corresponding spectrum.

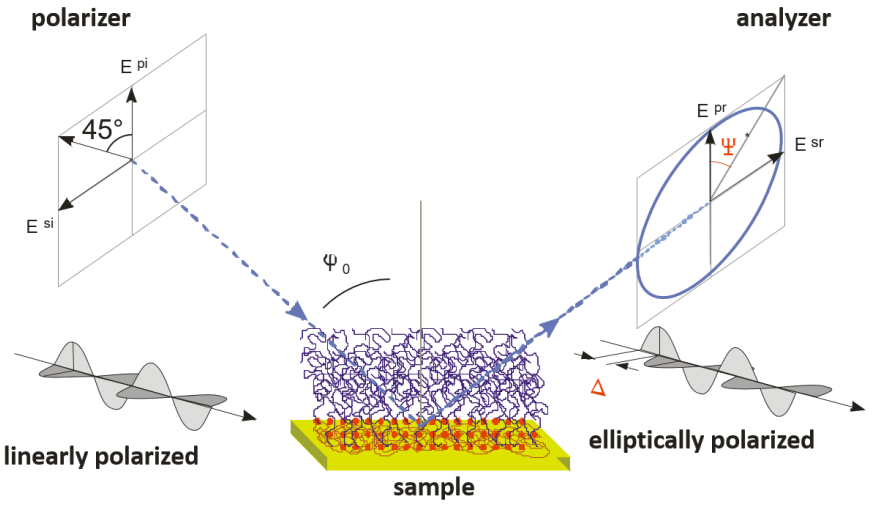

Figure 3.12. Principle of measurement: upon reflection at the sample, the polarization of the light is changed, i.e. the linearly polarized incident light becomes elliptically polarized after reflection.

3.4.2 Measurement of IRSE

The infrared spectroscopic ellipsometry measurements were carried out in the 300-5000 cm^{-1} spectral range at room temperature. Infrared ellipsometry is only

practicable in combination with Fourier transform spectrometer (FTS). The optical layout of the photometric ellipsometric measurement is shown in Figure 3.13.

In our measurement, The IRSE setup is a custom-built infrared spectroscopic ellipsometer attached to a FTIR (Vertex 70 from BRUKER, Germany) equipped with a liquid nitrogen cooled photovoltaic mercury cadmium telluride (MCT) detector and permanently purged with dry air. The ellipsometric parameter tanΨ, defined as the amplitude ratio of the reflected p- and s-polarized components, was measured at a spectral resolution of 4 cm^{-1}, an incidence angle of 80 ° for 4 cycles of 64 scans. Further details on the ellipsometric method can be found in ref.[114].

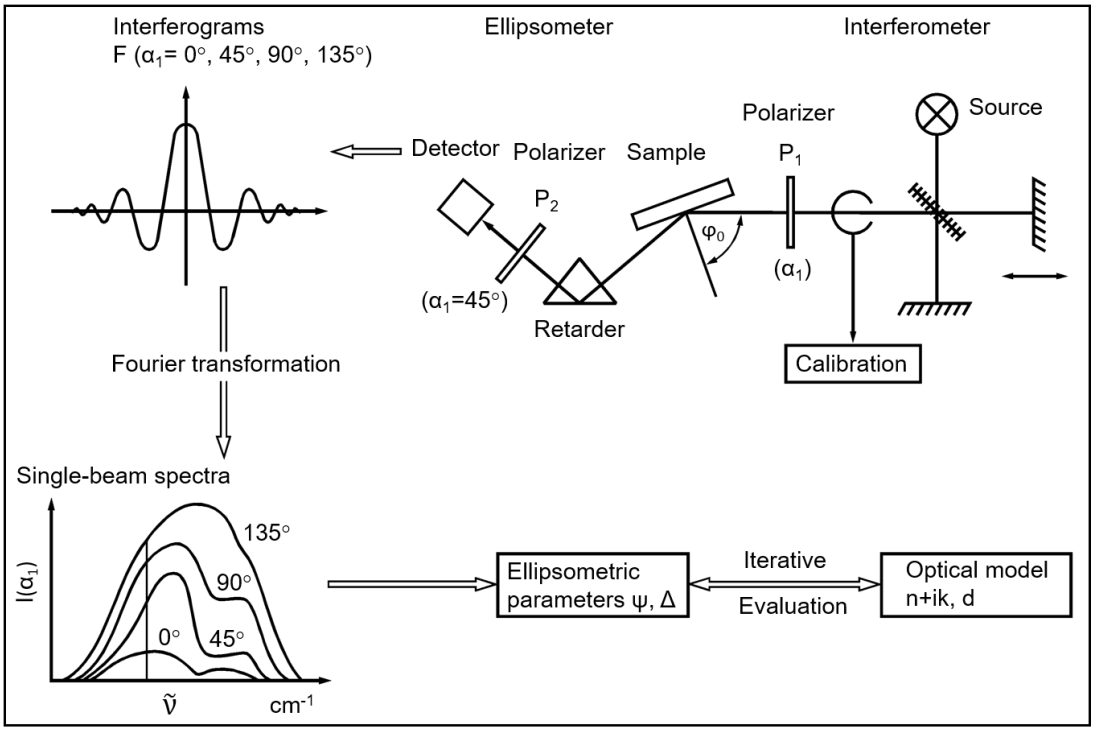

Figure 3.13. General procedure of infrared spectroscopic ellipsometry. Reprinted from ref [113] with the permission of Elsevier.

Compared to a dense DMSO layer, the vibrational absorption of DMSO molecules diluted in the perovskite layer is much smaller because of the relatively low density of vibrational dipole moments. For an isotropic thin layer on a metallic substrate then the bands in a tanΨ spectrum would correlate almost linearly with the vibrational absorption. The relative accuracy of the linear correlation between the integrated

density of DMSO molecules homogeneously diluted in $MAPbI_3$ and the IRSE signals at the S=O vibrational mode better than 5% was estimated by using the Brüggemann effective medium approximation, a layer thickness is about 400 nm and a refractive index of the $MAPbI_3$ equals to 2.

3.5 Scanning electron microscopy (SEM)

3.5.1 Principle of SEM

Electron microscopy (EM) is a technique that is often used for imaging nanometer-scale objects. It works in a similar way to traditional light microscope, however, a beam of electrons with a well-defined de Broglie wavelength replaces the visible light [115]. And magnetic fields are used to focus the electron beams instead of lenses. There are mainly two types of electron microscopy: the transmission electron microscopy (TEM) and the scanning electron microscopy (SEM).

The working mechanism of SEM is based on the interactions of the electrons and atoms at various depths in the sample. In SEM, when the focused electron beam of high energy collides on the sample surface, various kinds of signals are produced (see Figure 3.14), detected and sent to a video screen. These signals include secondary electrons (SE), Auger electron, characteristic X-rays, continuous X-rays, back-scattered electrons (BSE), transmitted electrons and electromagnetic radiations in ultraviolet, visible and infrared regions. Besides, electron-hole pairs, phonons (lattice vibrations) and plasmas (electron oscillation) can also be produced. By analyzing these signals, various physical and chemical properties of the samples such as morphology, composition, crystal structure and electronic structure can be obtained.

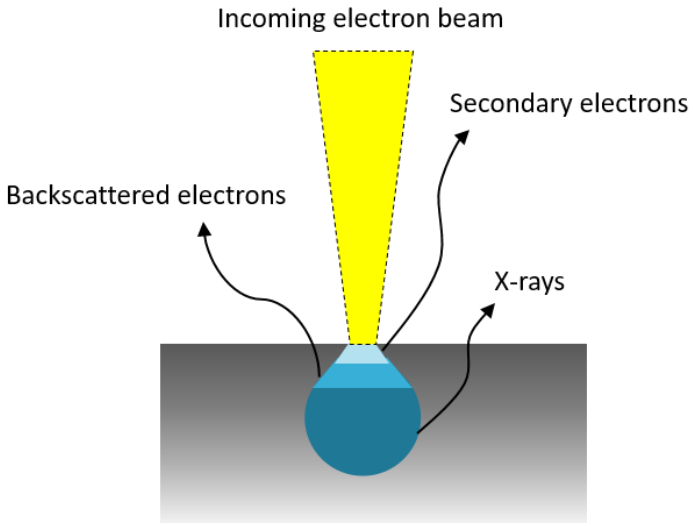

Figure 3.14. Different types of signals produced from different regions

3.5.2 Composition and application of SEM

Scanning electron microscope consists of three major components: a vacuum system, an electron beam system, and an imaging system. Figure 3.15 shows a brief schematic of the basic SEM components. The vacuum system mainly includes a vacuum pump and a vacuum column. And the main reason to use a vacuum system is that the filament in the electron beam system will be rapidly oxidized and disabled in atmosphere. The other reason is to increase the electron mean-free-path, then more electrons can be collected for imaging.

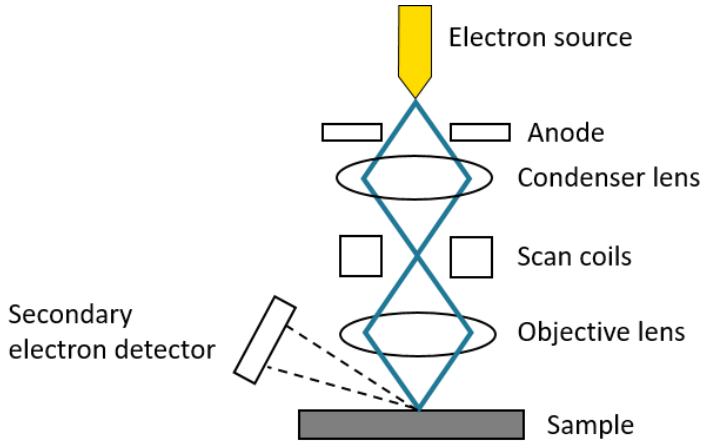

Figure 3.15. Brief schematic of the basic SEM components.

The electron beam system is composed of an electron gun and electromagnetic lenses. It is mainly used to generate an electron beam with a narrow energy distribution and certain energy for scanning image. At last, different detectors such as SE detector and BSE detector are used for the imaging system to analysis the generated signals.

The most common mode of scanning electron microscope is to detect secondary electrons emitted by exited atoms at the sample surface. The intensity of SE signal is affected by the included angle between the incident electron beam and surface, so an image of surface morphology can be obtained by detecting the generated SE signals. As the intensity of BSE signal is strongly related to the atomic number, BSE images can provide information about the elements distribution in the sample. Moreover, the characteristic X-rays can be used to identify the abundance of elements in the sample. In our experiment, SEM is used analysis the surface morphologies of perovskite film from top view and cross section.

3.6 Characterization of solar cells

Under illumination, a solar cell can provide a certain photovoltage at a given photocurrent. The combination of these two operation parameters for the solar cell is called a working point. According to Ohm's law, a particular working point of a solar cell is fixed with a load resistance (R_L). The short circuit current (I_{SC}) and the open circuit voltage (V_{OC}) are measured at R_L which is, under idealized conditions, equal to zero or infinitely high, respectively. The I_{SC} normalized to the area of the solar cell is called the short circuit current density (J_{SC}). A current-voltage characteristic (J-V characteristic) is a plot of all working points in a considered range. Figure 3.16 shows schematically the J-V characteristic of a solar cell under illumination.

The working point at maximum power is called the maximum power point (mpp). The corresponding photovoltage and photocurrent density are called V_{mp} and J_{mp}, respectively.

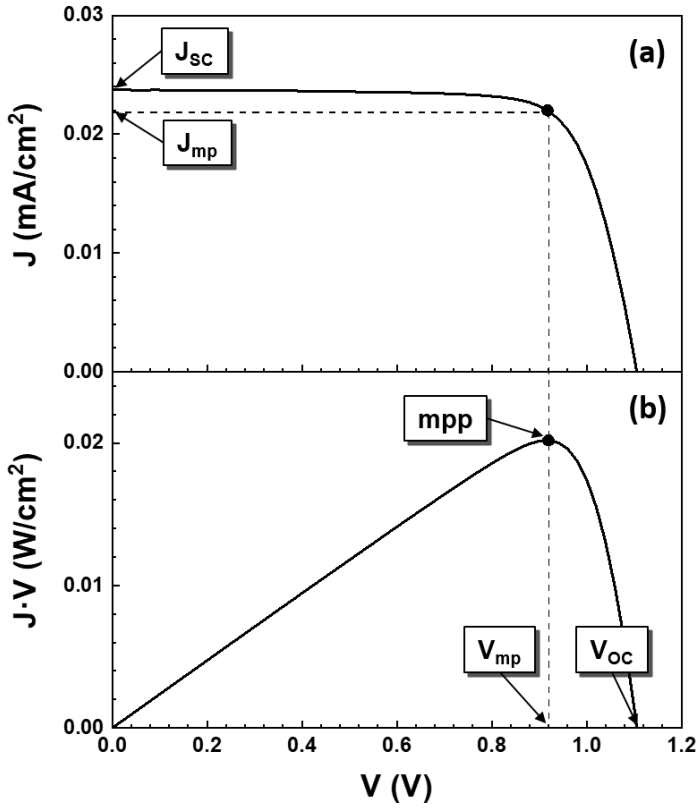

Figure 3.16. Example of a current-voltage characteristic (a) and of the corresponding power-voltage characteristic (b) of a solar cell under illumination. The open circuit voltage, the short circuit current density, the maximum power point and the voltage and current density at the maximum power point are denoted by V_{OC}, J_{SC}, mpp, V_{mp} and I_{mp}, respectively.

The values of J_{SC} and V_{OC} can be measured directly. Thus, it is easier to characterize the maximum power with the J_{SC}, V_{OC} and an additional parameter. This parameter is described as the proportion of the maximum power and the product of J_{SC} and V_{OC}. It is therefore called the fill factor (FF).

$$\mathrm{FF} = \frac{J_{mp} \cdot V_{mp}}{J_{SC} \cdot V_{OC}} \qquad (3.11)$$

The power conversion efficiency (PCE) of a solar cell is defined as the ratio between the maximum output power of the solar cell and the incident power from the sunlight (P_{in}).

$$\mathrm{PCE} = \frac{J_{SC} \cdot V_{OC} \cdot FF}{P_{in}} \qquad (3.12)$$

In the equivalent circuit of a solar cell (Figure 3.17), there are two fundamental functions expressed by a current source driven by illumination, i.e. the photo current (I_{ph}) generator, and a diode describing the condition of charge separation, i.e. the current can only pass through the element in one direction.

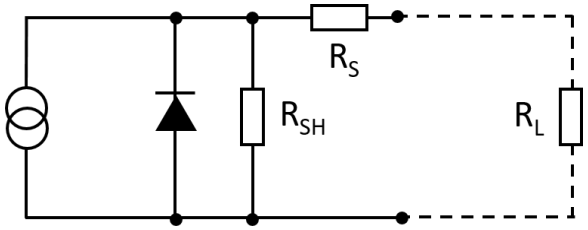

Figure 3.17. Equivalent circuit of a solar cell containing a photocurrent generator, a diode describing charge separation, a load resistance (R_L), a shunt resistance (R_{SH}) and a series resistance (R_S).

A current across a diode (I_D) is described by the diode equation.

$$I_D = I_0 \cdot \left[\exp\left(\frac{q \cdot U}{k_B \cdot T}\right) - 1\right] \qquad 3.13$$

The diode equation contains the proportionality factor which is called the diode saturation current (I_0) or diode saturation current density (J_0, in a unit area). The diode saturation current is a specific characteristic of each solar cell depending on the absorber and contact materials as well on their geometry.

The resistance of an ideal diode is very low in forward direction and very large in reverse direction. So the photo current is not shunted by the diode. Therefore the photo current is a reverse current and has to be subtracted from the diode current. For I-V characteristics, the I_{ph} corresponds to I_{SC} as a convention. This results in the diode equation of the ideal solar cell.

$$I = I_{SC} - I_0 \cdot \left[\exp\left(\frac{q \cdot U}{k_B \cdot T}\right) - 1\right] \qquad (3.14)$$

The V_{OC} of an ideal solar cell can be obtained from equation 3.14 when setting the current to zero.

$$V_{OC} = \frac{k_B \cdot T}{q} \cdot \ln\left(\frac{I_{SC}}{I_0} + 1\right) \approx \frac{k_B \cdot T}{q} \cdot \ln\left(\frac{I_{SC}}{I_0}\right) \qquad (3.15)$$

The value of I_0 depends on the materials and on interfaces between materials forming the diode and can change over many orders of magnitude. The importance of I_0 for the performance of a solar cell follows from the limitation of V_{OC} by I_0. The minimization of I_0 is crucial for the optimization of the performance of solar cells in general. Based on equation 3.15, I_0 can be roughly estimated from the measured I_{SC} and V_{OC}.

$$I_0 = \frac{I_{SC}}{\exp\left(\frac{q \cdot V_{OC}}{k_B \cdot T}\right)} \qquad (3.16)$$

In practice, solar cells have losses due to ohmic resistances. For example, contact resistances or material resistances are responsible for series resistances (R_S) and local shunts or other factors cause shunt resistances (R_{SH}). As depicted in Figure 3.17, R_S and R_{SH} have to be considered in the equivalent circuit of a real solar cell.

When the R_S and R_{SH} are taken into account, the diode equation is

$$I = I_{SC} - I_0 \cdot \left[\exp\left(\frac{q \cdot (U + I \cdot R_S)}{k_B \cdot T}\right) - 1\right] - \frac{U + I \cdot R_S}{R_{SH}} \qquad (3.17)$$

The values of R_S and R_{SH} can strongly influence the I-V characteristics of a solar cell. Figure 3.18 shows the principal influence of R_S and R_{SH} on the J-V curves of solar cells.

As known, a part of the photon flux from the sun (Φ_{sun}) is absorbed and converted into the photocurrent of the solar cell. The photons have different energy (E_{ph}) and the photons with energy below the E_g don not participate the process of photoelectric conversion. The maximum photo current can be obtained if all photons with energy equal or above E_g are absorbed and each absorbed photon generates one electron-hole pair (quantum efficiency equal to 1).

$$I_{SC}^{max} = q \cdot \int_{E_g}^{\infty} \Phi_{sun}(E_{ph}) \cdot dE_{ph} \qquad (3.18)$$

Solar cells are characterized under standard test conditions (STC, ref [116]). Under STC for AM1.5G (global radiation at air mass 1.5), the temperature is 25 ℃, P_{in} is equal to 100 mW/cm^2 and the sun spectrum is equal to the spectrum given, for example, in ref [117]. The band gap of $MAPbI_3$ is of the order of 1.55 eV. The maximum photocurrent density for a solar cell based on $MAPbI_3$ is of the order of 25-28 mA/cm ²(see ref [118]).

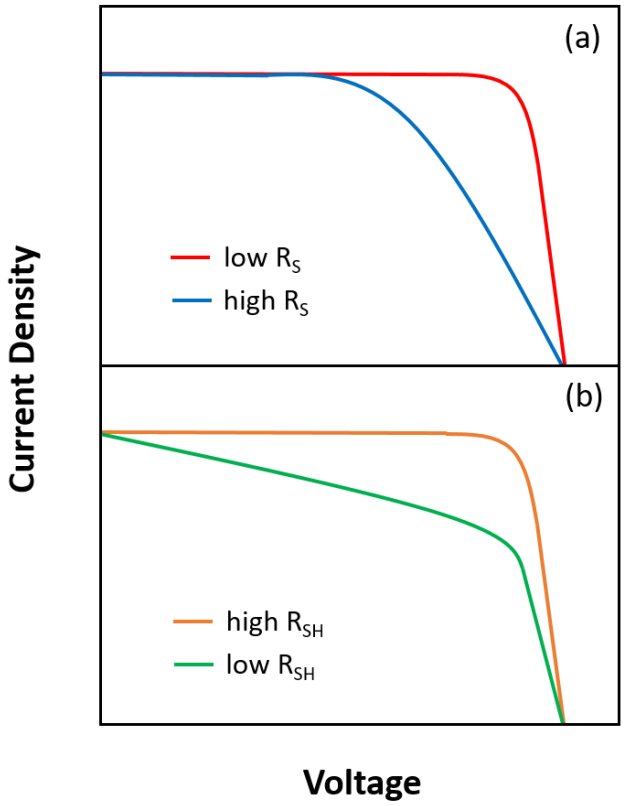

Figure 3.18. J-V characteristics for a solar cell with negligible R_{SH} (a) or R_S (b) for different values of R_S (a) and R_{SH} (b).

Moreover, as described above, when a photon is absorbed by the absorber in a solar cell it can produce an electron-hole pair. The photo-generated electrons may reach the p-n junction and contribute to the current produced by the solar cell; such an electron is said to be collected. Or, the electrons recombine with no contribution to the current.

The ratio between the number of collected photo-generated electrons (N_e) and of incident photons (N_{ph}) is called quantum efficiency (QE) of a solar cell.

$$QE(\lambda) = \frac{N_e(\lambda)}{N_{ph}(\lambda)} \qquad (3.19)$$

The external quantum efficiency (EQE) of a solar cell includes the effect of optical losses such as transmission and reflection. The J_{SC} of a solar cell can be calculated if the EQE spectrum of a solar cell is known. For this purpose, the product of the EQE spectrum and the photon flux spectrum of the sun ($\varphi_{sun}(\lambda)$) are integrated over the wavelength.

$$J_{SC} = q \cdot \int_0^{\infty} EQE(\lambda) \cdot \Phi_{sun}(\lambda) \cdot d\lambda \qquad (3.20)$$

The values of the J_{SC} obtained from the J-V characterization with a sun simulator and obtained from the EQE spectrum should be equal if the sun simulator and the reference solar cell for the analysis are well calibrated. In practice, however, there is a deviation due to the experimental errors.

In our experiments, J-V characterization under 1 sun equivalent illumination were performed by using an Oriel LCS-100 class ABB sun simulator in a N_2-filled glovebox. The sun simulation was calibrated with a c-Si reference solar cell from Fraunhofer ISE. J-V scans were performed with a Keithley 2400 SMU, controlled by a program written in LabView. The voltage values were swept in 20 mV steps with an integration time of 40 ms per point and settling time of 40 mV after voltage application, corresponding to a scan speed of 250 mV/s. This fast scan speed was chosen to emphasize possible current-voltage hysteresis. Forward and reverse scan were swept subsequently without interruption.

EQE spectra were recorded with an Oriel Instruments QEPVSI-b system with a Newport 300 W xenon arc lamp, controlled by TracQ-Basic software. The white light is split into monochromatic light by a Newport Cornerstone 260 monochromator and

chopped at a frequency of 78 Hz before being conducted to the PSC surface via optical fibers. The system is calibrated using a Si reference cell with known spectral response before every measurement. The average short-circuit mismatch between integrated values from EQE and values from J-V scans is 1-5%.

4. Properties of $MAPbI_3$ layers and solar cells with varied vacuum-assisted evaporation conditions

The formation of perovskite layers from films of dissolved precursor salts depends on numerous factors influencing evaporation, formation of intermediate phases and formation of seeds. For a vacuum-assisted treatment, such factors can be (1) the stoichiometry of solvents (such as DMF:DMSO), (2) the temperature during vacuum-assisted treatment (T_{vac}), (3) the time of vacuum-assisted treatment (t_{vac}), (4) the value of the vacuum, and (5) the composition of dissolved salts. In this chapter, we kept the values of the vacuum (60 Pa) and the composition of dissolved salts (methylamine and PbI_2) unchanged and varied DMF: DMSO, t_{vac}, and T_{vac}. The influence of variations on $MAPbI_3$ layers and solar cells were investigated.

4.1 The function of vacuum-assisted treatment in perovskite preparation

Hybrid organic-inorganic metal halide perovskite absorbers for solar cells are usually prepared from metal salt solutions. Films of metal salt solutions can be easily deposited by spin coating, printing or dipping. Then the films of the dissolved precursor solutions are transferred into perovskite phase by performing evaporation of solvents and subsequent annealing at a relatively low temperature (post annealing, usually at 90-150 ℃). The controlled evaporation of the solvents is important for the formation of a homogeneous perovskite layer. As a method for rapid solvent evaporation, vacuum-assisted evaporation of solvents (vacuum-assisted treatment) is one of the practical way to control the morphology.

To understand the effect of vacuum-assisted evaporation on the morphology of the perovskite film, the nucleation and growth process of the perovskite in solution system can be described by the classical LaMer model, which is widely used to

explain the nucleation and grain growth process [119-121]. In Figure 4.1 (a), the LaMer curves show the concentration change of the perovskite precursor solution as a function of time at a constant and isothermal evaporation rate of the solvent.

As illustrated, the LaMer model can be divided into three stages. At the first stage, with the evaporation of the solvent, the solution concentration reaches saturation concentration (C_s). However there are no nuclei generated because the energy barrier needs to be overcome. Once the solution concentration exceeds a supersaturation concentration (minimum concentration of nucleation, C_{min}), in the second stage, nuclei start to generate. With the continuous evaporation of solvent, the solution concentration continuously increases, and as a result, the nucleation rate increases. Afterwards, the solution concentration drops below the C_{min} as the solute is continuously consumed during the nucleation. At this point, the nucleation rate drops down to zero. Then, in the third stage, the size of the nuclei gradually increases due to the continuous addition of monomers. Figure 4.1 (a) also shows that, under the fast solvent evaporation, the nucleation period of time is longer. This is because the rapid evaporation of solvent keeps the solution concentration above the C_{min} in spite of the solute consumption.

Figure 4.1 (b) shows the nucleation/growth model in perovskite precursor solution under slow and fast solvent evaporation. As shown, under the slow solvent evaporation, after the nuclei are generated, those nuclei will grow rapidly because of the large sized colloidal particles dispersed in the precursor solution [122], leading to fast solute consumption. Then the solution concentration drops down to C_{min} quickly but is larger than C_s. In the later stage, no more nuclei are generated on the substrate but grains will continuously grow in the region. These grains grow too fast and too large based on colloidal particles, leading to localized solute accumulation on the substrate [123-124]. Therefore the perovskite film contains large sized rod-shaped grains from colloid-based growth and small grains from solution-based growth and bares the substrate due to the reasons of the fast crystal growth rate and few nuclei generated.

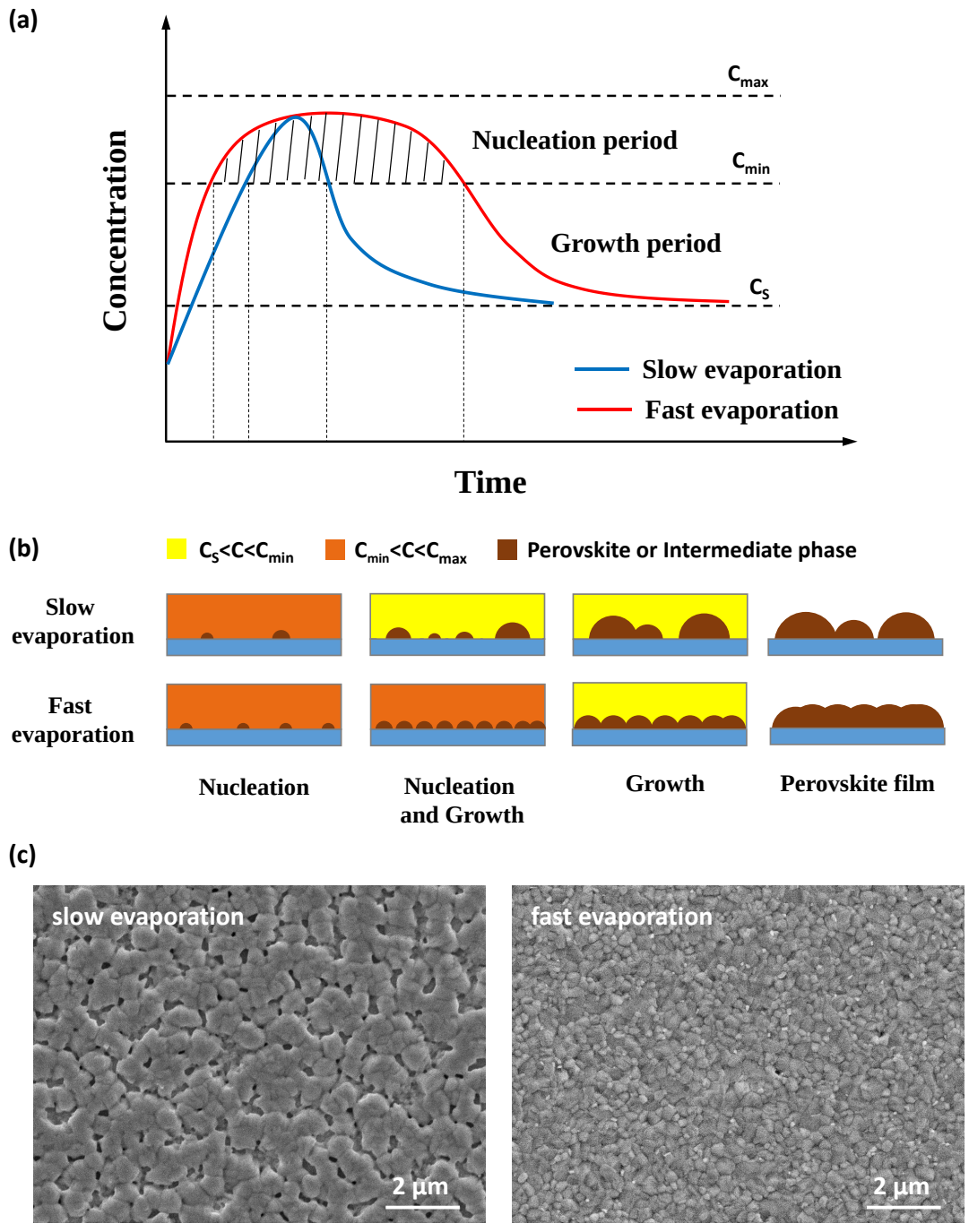

Figure 4.1. LaMer model of slow solvent evaporation (blue curve) and fast solvent evaporation (red curve): the concentration change of the perovskite precursor solution as a function of time at a constant evaporation rate of the solvent (a), the nucleation/growth competition model under slow solvent evaporation and fast solvent evaporation (b), surface morphologies of $MAPbI_3$ films prepared by slow solvent evaporation and fast solvent evaporation respectively (c). C_s: saturation concentration; C_{min}: minimum concentration of nucleation; C_{max}: maximum concentration of nucleation.

Under the fast solvent evaporation, the solution concentration stay above C_{min} longer. Thus the nuclei are generated on the substrate until there is no place left and the crystal growth time reduces remarkably. Finally the uniform grain size and full-coverage perovskite film can be obtained. Based on the above analysis and the LaMer model, if the vacuum-assisted treatment is adopted, a perovskite layer with high quality could be produced. However, the measured surface morphologies of $MAPbI_3$ layers prepared via slow and fast solvent evaporation (see Figure 4.1 (c)) were consistent with the estimated result from the model.

4.2 Influence of the DMF/DMSO ratio during the vacuum-assisted treatment

The mixed solvents of DMF and DMSO are frequently used for preparing high-quality pervoskite layers in solution method. As they have different boiling points and bonding abilities with PbI_2, changing the DMF/DMSO ratio (below mentioned DMF/DMSO ratios are all volume ratios) will have significant effect on the solvent evaporation, the formation of intermediate phases and the formation of seeds thus affecting the crystal quality, the surface morphology, the electronic and the optical properties of these perovskite films (the temperature and the time of vacuum-assisted treatment were kept at 30 ℃ and 60 s respectively).

4.2.1 Influence of the DMF/DMSO ratio on morphology of $MAPbI_3$

The SEM images of the $MAPbI_3$ films are shown in Figure 4.2.

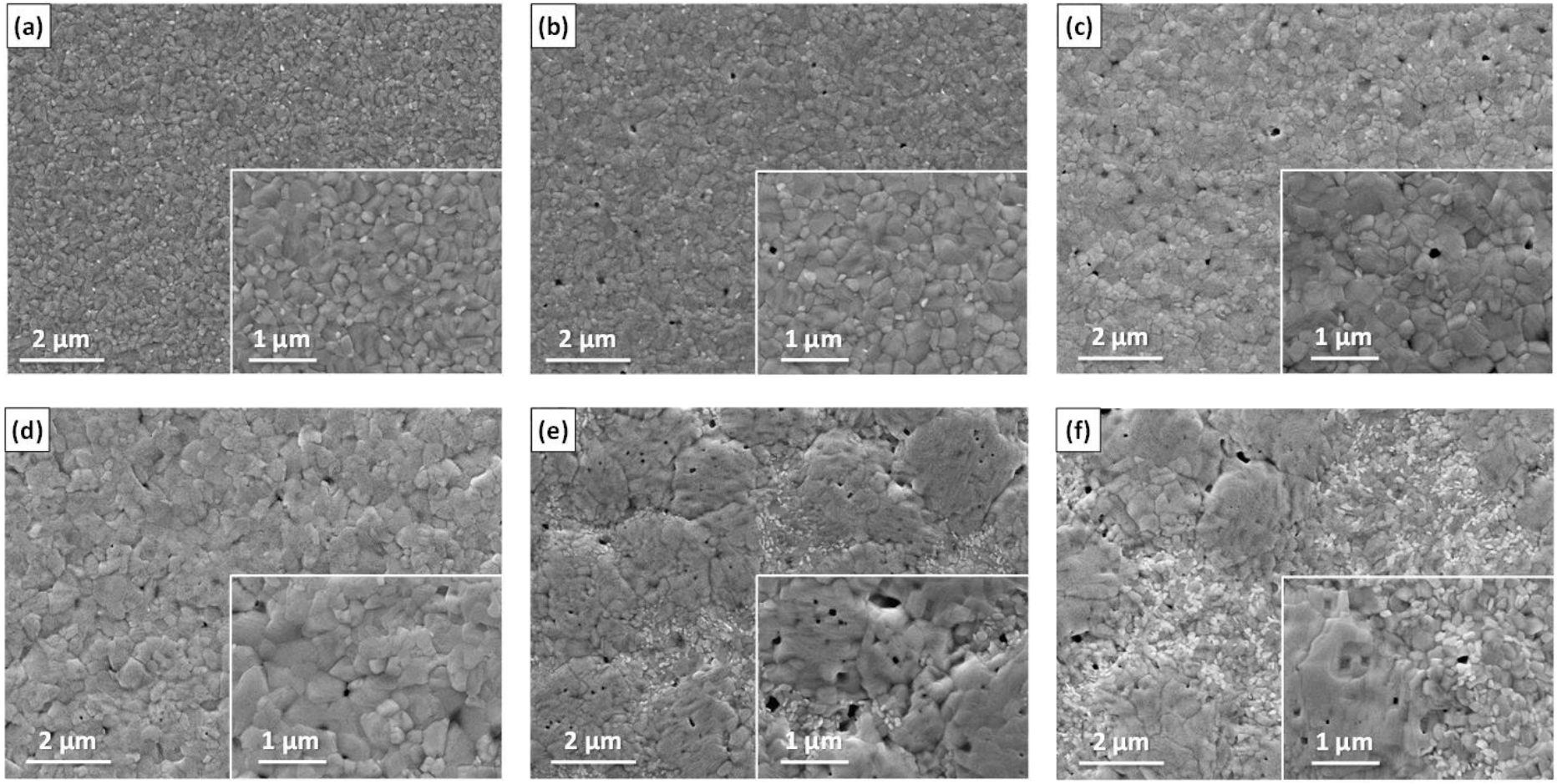

Figure 4.2. Surface view morphologies of the MAPbI3 films prepared from precursor solution with the DMF/DMSO ratio of 12:1(a), 9:1(b), 8:1(c), 7:1(d), 6:1(e) and 4:1(f). The scale bars in all large images are 2 µm and the scale bars in all small images are 1 µm.

From the top-view images, we can observe that the grain size gradually increased when the DMF/DMSO ratio decreased from 12:1 to 7:1. From the grain size distributions (Figure 4.3), we found that the mean size increased from 241 to 316 nm, and more crystals larger than 300 nm formed with increasing DMSO proportion. But when the DMSO proportion continued to increase (6:1 and 4:1), many small crystals (smaller than 200 nm) appeared and large clusters without clear grain boundaries formed.

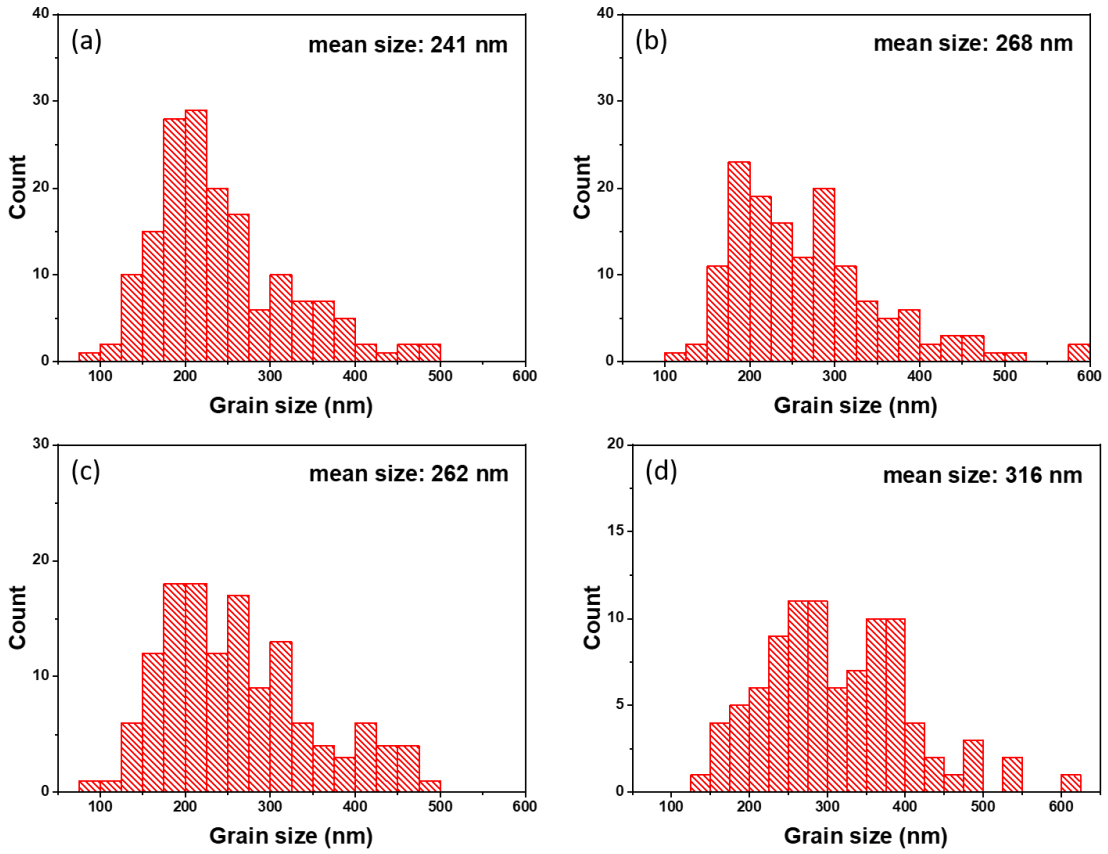

Figure 4.3 Grain size distribution of $MAPbI_3$ prepared from precursor solutions with DMF/DMSO ratios of 12:1 (a), 9:1 (b), 8:1 (c) and 7:1 (d).

Note that more pinholes/voids existed in the $MAPbI_3$ films when the proportion of DMSO increased. The pinhole densities are shown in Figure 4.4. The pinhole density increased by an order of magnitude when the DMF/DMSO ratio was reduced from 12:1 to 9:1. Hereafter, although the pinhole densities had a trend of increase, the variation was small. The increasing proportion of DMSO increased the boiling point

of the mixed solvent which led to a decline in the solvent evaporation rate.

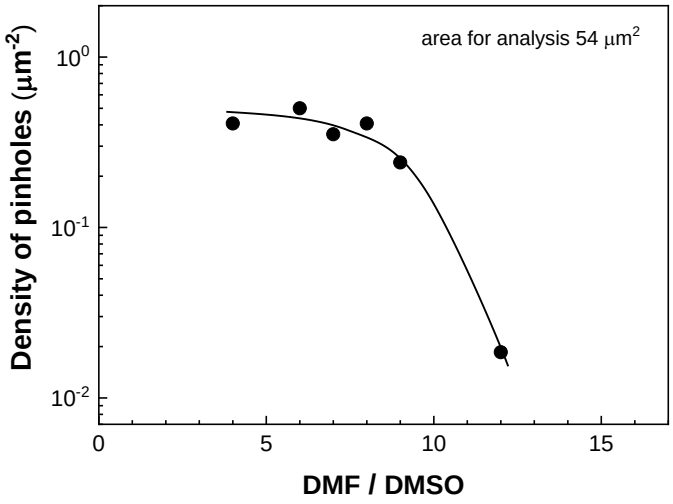

Figure 4.4. Pinhole densities of $MAPbI_3$ films as a function of the DMF/DMSO ratio. The solid line is a guide for the eye.

On the basis of the above results and the qualitative nucleation/growth model, a higher DMSO proportion caused the formation of a smaller number of nuclei and of larger grains due to shorter nucleation and longer growth times. Therefore, the mean size of grains increased, but the pinhole density increased as well. As the proportion of DMSO continued to increase, larger grains no longer formed and many small crystals and clusters appeared. This is in contradiction to the qualitative nucleation/growth model (solution-based growth). However, one has to take into account that increasing coordination between DMSO and PbI_2 can lead to a strong increase of nuclei (colloid-based growth). A quantitative, i.e. kinetic, model considering both solution-based and colloid-based growth shall take into account the competition between DMF, DMSO and iodide for adsorption sites.

4.2.2 Influence of the DMF/DMSO ratio on the band gap and exponential tails of $MAPbI_3$

Figure 4.5 shows in-phase and phase-shifted by 90 ° SPV spectra of $MAPbI_3$ prepared

from the precursor solutions with DMF/DMSO ratio of 12:1, 9:1, 8:1, 7:1, 6:1 and 4:1. The in-phase signals were negative for all samples. This means that photo-generated electrons were separated preferentially toward the external surface. Furthermore, the amplitude of in-phase signals successively increased with the increasing DMSO proportion and the phase-shifted by 90 °signals changed a little.

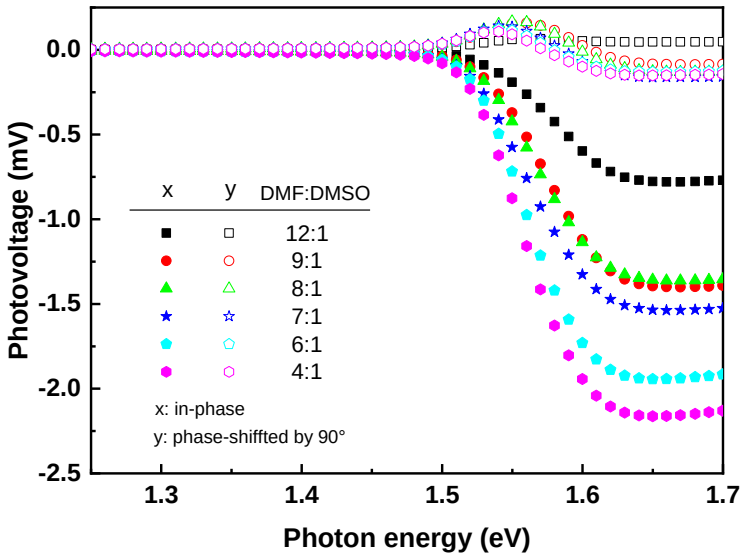

Figure 4.5. In-phase and phase-shifted by 90 °SPV spectra of $MAPbI_3$ prepared from the precursor solutions with DMF/DMSO ratios of 12:1, 9:1, 8:1, 7:1, 6:1 and 4:1 (squares, circles, triangles, stars, pentagons and hexagons respectively).

The values of E_g were determined from the SPV amplitude spectra by analyzing the Tauc plots (Figure 4.6 (a)). For the samples prepared from the precursor solutions with DMF/DMSO ratio of 12:1, 9:1, 8:1, 7:1, 6:1 and 4:1, the values of E_g were 1.564, 1.559, 1.551, 1.547, 1.545 and 1.543 eV, respectively (Figure 4.6 (b)). Therefore, the increase of the DMSO proportion in the precursor solution led to a decrease of the band gap of $MAPbI_3$. Therefore, the band gap of $MAPbI_3$ layers is not constant but depends on preparation conditions. This shall be caused by tiny distortions in the local crystal structure.

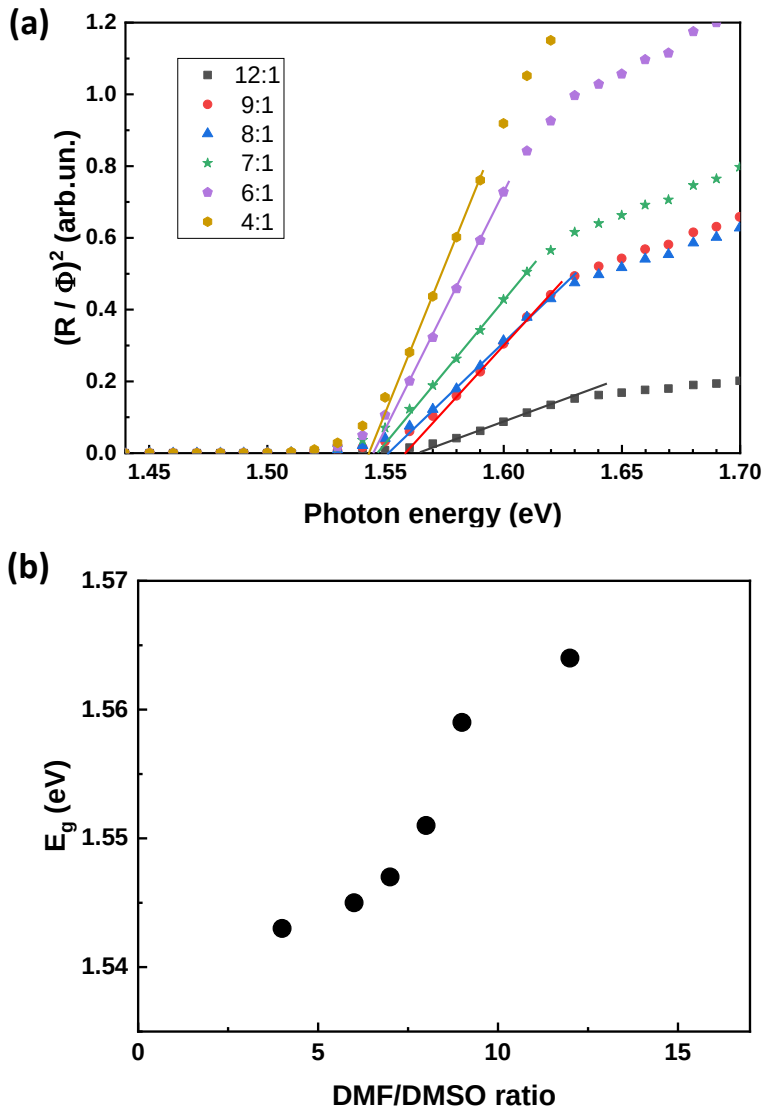

Figure 4.6. Tauc plots of the SPV amplitude spectra of $MAPbI_3$ layers prepared with DMF/DMSO ratios of 12:1, 9:1, 8:1, 7:1, 6:1 and 4:1 (squares, circles, triangles, stars, pentagons and hexagons, respectively) (a) and band gaps as a function of the DMF/DMSO ratio (b).

Figure 4.7 (a) shows the quotient of the SPV amplitude and the photon flux spectra on a logarithmic scale. The exponential increase close to E_g was described by the characteristic energy of exponentially distributed defect states below the band gap (E_t). As shown, the corresponding values of E_t were low and amounted to 22.5, 20.5, 20.5, 20, 18.8 and 19.5 meV for the DMF/DMSO ratio of 12:1, 9:1, 8:1, 7:1, 6:1 and 4:1, respectively (Figure 4.7 (b)). Furthermore, E_t showed a trend of decrease with increasing DMSO proportion. For comparison, the exponential tails were of the order

of 80−140 meV for In_2S_3 layers deposited from a solution-based process [125]. Therefore, the disorder in $MAPbI_3$ layers was relatively low and did only slightly change as a function of the DMF/DMSO ratio.

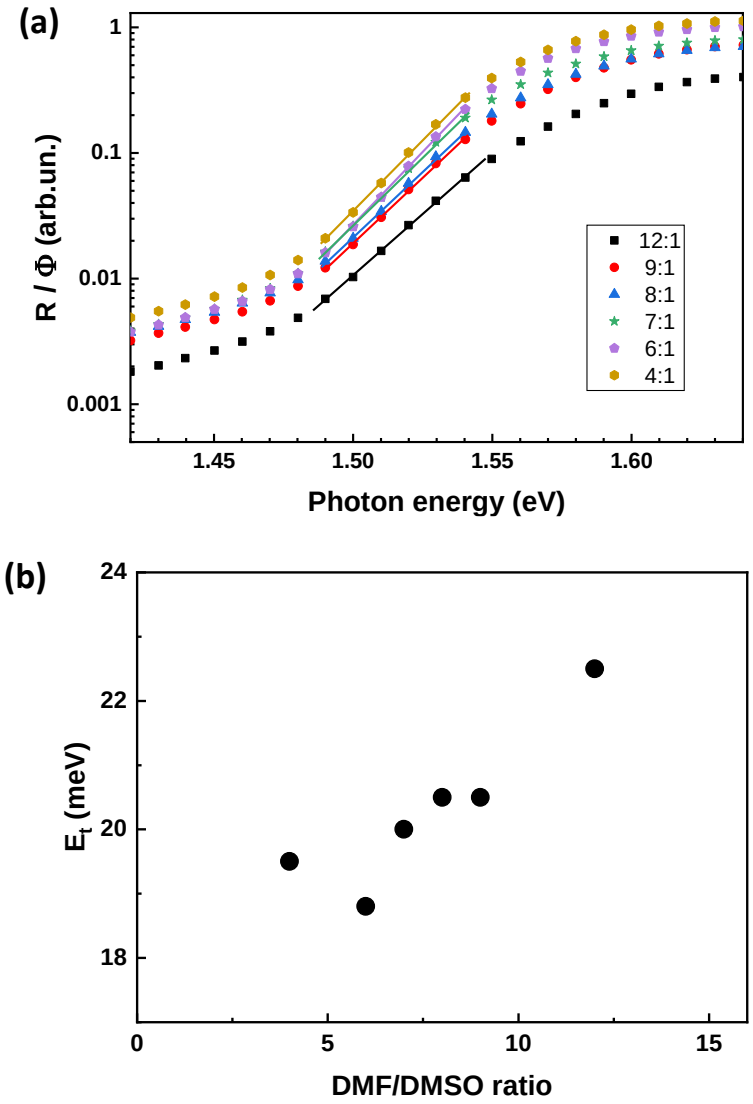

Figure 4.7. Spectra of the quotient of SPV amplitude and the photon flux on a logarithmic scale near the band gap of $MAPbI_3$ layers prepared with DMF/DMSO ratios of 12:1, 9:1, 8:1, 7:1, 6:1 and 4:1 (squares, circles, triangles, stars, pentagons and hexagons respectively) (a) and exponential tails as a function of the DMF/DMSO ratio (b).

4.2.3 Influence of DMF/DMSO ratio on $MAPbI_3$ based solar cells

Typical J-V characteristics in forward and backward scans for a $MAPbI_3$ based solar

cell from our experiments are shown in Figure 4.8. In the forward scan, the values of J_{SC}, V_{OC}, FF were 20.77 mA/cm^2, 1.09 V, 77.68%, respectively, and corresponded to an efficiency of 17.54%. In the backward scan, the values of J_{SC}, V_{OC}, FF were 20.66 mA/cm^2, 1.09 V, 78.06%, respectively, and corresponded to an efficiency of 17.53%. All values were very close, even the fill factors. The hysteresis index between the forward and backward scans can be defined as [126]:

$$H = \frac{\int_0^{Voc} J_{rev}(V)\,dV - \int_0^{Voc} J_{for}(V)dV}{\int_0^{Voc} J_{rev}(V)dV} \qquad (4.1)$$

Where $J_{for}(V)$ and $J_{rev}(V)$ are the current densities during forward and reverse scan respectively. The absolute value of hysteresis index was 0.002 for the given example. Since the hysteresis index was comparable to this very small value also for other solar cells, only the forward characteristics were considered for the variation of parameters and statistics in the following analysis.

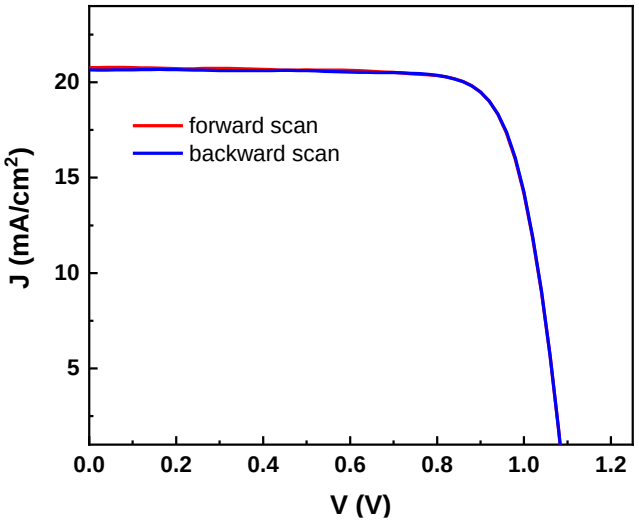

Figure 4.8. Typical J-V characteristics in forward and backward scans (red and blue lines, respectively) for a solar cell based on a $MAPbI_3$ layer prepared by vacuum-assisted treatment.

Figure 4.9 shows the measured values of J_{SC}, V_{OC}, FF and PCE for the solar cells based on the $MAPbI_3$ prepared from the precursor solution with DMF/DMSO ratios of 12:1, 9:1, 8:1, 7:1, 6:1 and 4:1, respectively. There were about 12 solar cells measured

for each DMF/DMSO ratio.

As shown in Figure 4.9 (a), the highest PCE of 17.43% was obtained from the solar cells based on the $MAPbI_3$ prepared from the precursor solution with the DMF/DMSO ratio of 9:1. The average value of the PCE was 17.27%. For comparison, the average PCE was 17.00% for DMF/DMSO ratio equal to 12:1. Furthermore, the values of the average PCE decreased with decreasing DMF/DMSO ratios to 16.20%, 15.60%, 15.50% and 13.48% for DMF/DMSO ratios of 8:1, 7:1, 6:1 and 4:1, respectively. The solar cells prepared for a DMF/DMSO ratio of 9:1 also had the highest values of V_{OC} (Figure 4.9 (b)) and J_{SC} (Figure 4.9 (c)). With the increasing DMSO proportion, the values of the average J_{SC} were 20.60, 21.04, 20.31, 19.78, 19.99 and 18.11 mA/cm^2 in turn. There was a decline trend when DMSO proportion kept increasing. But it was not monotonous at the DMF/DMSO ratio of 6:1. For the values of the average V_{OC}, the trend was the same. In contrast, there was no clear trend for FF which scattered between about 73 and 78 % (Figure 4.9 (d)). The maximum values of FF for DMF/DMSO ratios of 12:1, 9:1, 8:1, 7:1 were about 77.5%, but for DMF/DMSO ratios of 6:1 and 4:1, the maximum values were 76.5% and 74.5% respectively.

According to the results, we speculate that when the DMF/DMSO ratio declined from 12:1 to 9:1, the grain size was the main factor which affected the solar cell performance. The diffusion length in $MAPbI_3$ layers is limited by the size of the grains [46]. Therefore, larger grain size helped to increase the diffusion length of photo-generated charge carriers [47]. Furthermore, an increase of the mean grain size also meant a decrease of the region around grain boundaries available for recombination which reduced the recombination loss.

As the DMSO proportion kept increasing, the performance of solar cells showed descend trend with a decrease in all parameters. The decline of V_{OC} in solar cells was larger than that of band gap by a factor of the order of 3. Therefore, the increased

recombination rate with increasing DMSO proportion was not only caused by a reduction of E_g (limitation by radiative recombination) but also influenced by other recombination processes.

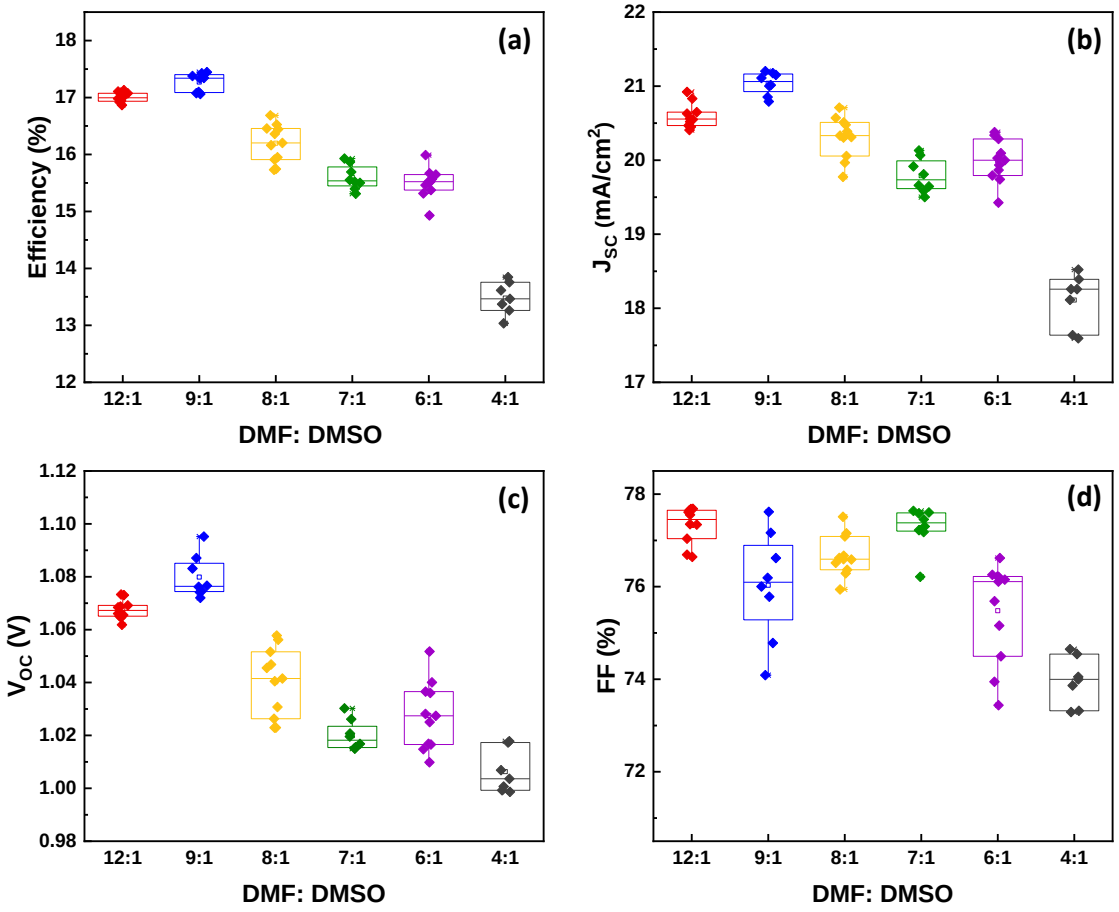

Figure 4.9. (a) power conversion efficiency (PCE), (b) short-circuit current density (J_{SC}), (c) open-circuit voltage (V_{OC}) and (d) fill factor (FF) of the solar cells based on the $MAPbI_3$ prepared from the precursor solution with DMF/DMSO ratios of 12:1, 9:1, 8:1, 7:1, 6:1 and 4:1, respectively.

Moreover, we also compared the average values of the measured short-circuit current densities (J_{SC}) and the maximum values of the ideal short-circuit current densities (J_{SC}^{max}, see the calculation of J_{SC}^{max} in Chapter 3) from the $MAPbI_3$ solar cells with different measured band gap. As shown in Figure 4.10 (a), the J_{SC} increased when the J_{SC}^{max} decreased with the increased band gap. It could be that the change of morphologies of $MAPbI_3$ reduced the optical loss. Besides comparing the difference

between J_{SC}^{max} and J_{SC}, the diode saturation current density (J_0) was also studied (Figure 4.10 (b), see the diode equation of the ideal solar cells in Chapter 3). The importance of J_0 for the performance of a solar cell follows from the limitation of V_{OC} by J_0. The minimization of J_0 is crucial for the optimization of the performance of solar cells in general. As shown, there was a downtrend of J_0 when the band gap increased. Combined with the previous result, the solar cells which showed better performance were based on the $MAPbI_3$ prepared with less DMSO.

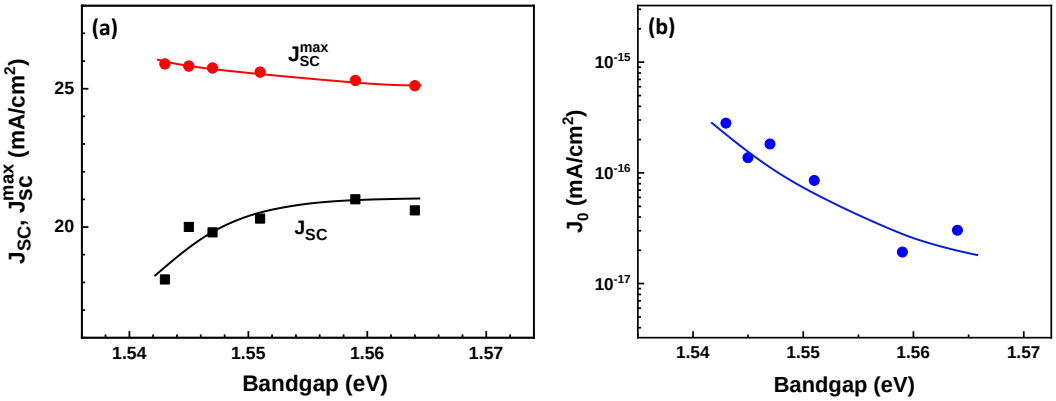

Figure 4.10. The average values of the measured short-circuit current densities (J_{SC}), the maximum values of the ideal short-circuit current densities (J_{SC}^{max}) and the diode saturation current density (J_0) of $MAPbI_3$ solar cells based on $MAPbI_3$ prepared from solution with different DMF/DMSO ratio.

4.3 Role of the temperature during the vacuum-assisted treatment

Except the boiling point and bonding ability, the temperature is also a main factor which has effect on the solvent evaporation and crystallization. Therefore, the surface morphology, electronic properties and optical properties of $MAPbI_3$ prepared with different temperature during vacuum were investigated (the DMF/DMSO ratio and the time of vacuum-assisted treatment were kept at 9:1 and 60 s respectively).

4.3.1 Role of the temperature for the morphology of $MAPbI_3$ layers

The SEM images of the $MAPbI_3$ films are shown in Figure 4.11.

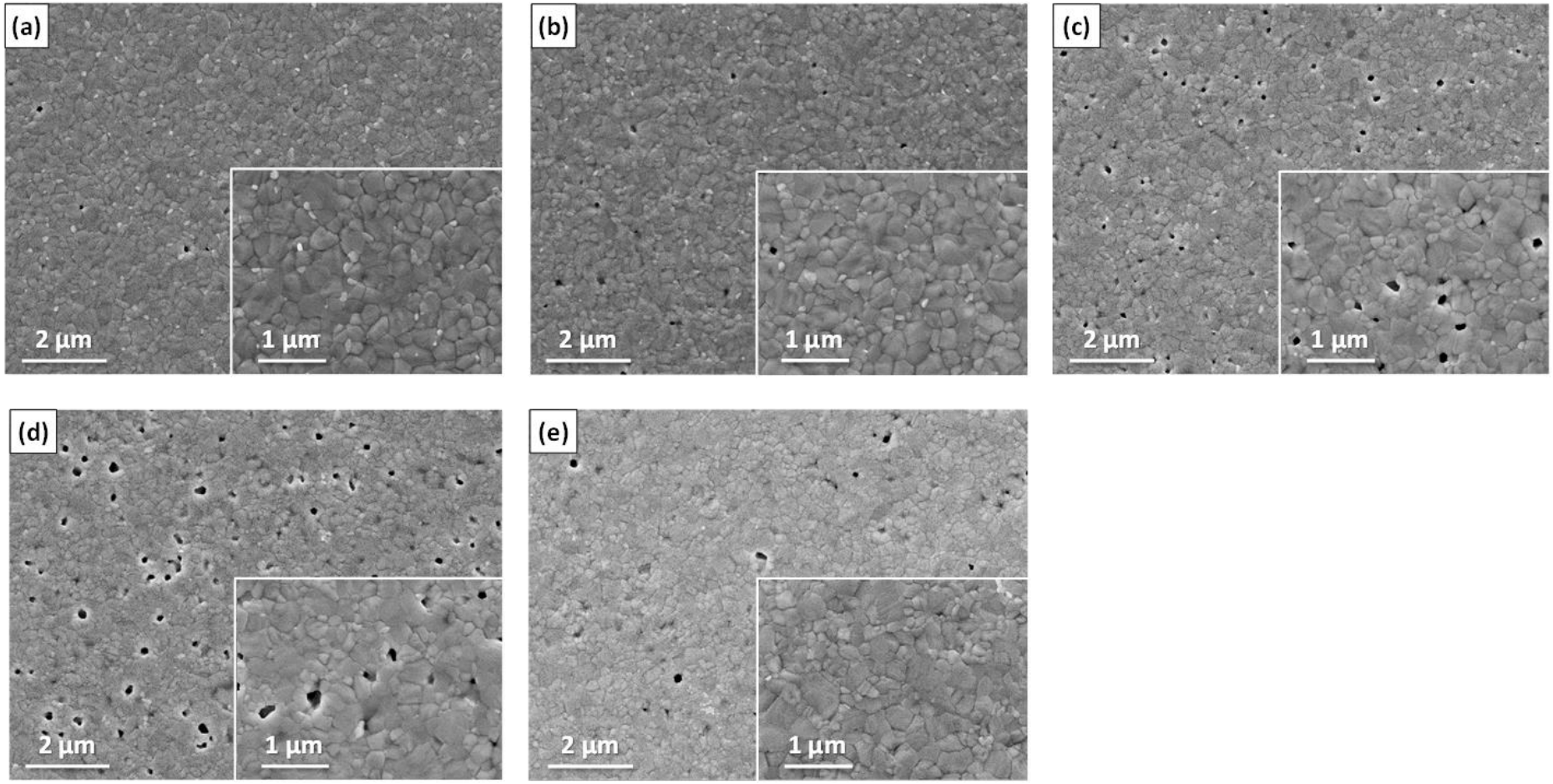

Figure 4.11. Surface view morphologies of the $MAPbI_3$ films prepared by vacuum-assisted treatment with the temperature of 20 ℃ (a), 30 ℃ (b), 40 ℃ (c), 50 ℃ (d) and 60 ℃ (e). The scale bars in all large images are 2 µm and the scale bars in all small images are 1 µm.

From the top-view images, we can observe that, more and more small crystals appeared while the amount of crystal over 400 nm dropped off when the temperature increased from 20 ℃ to 60 ℃.

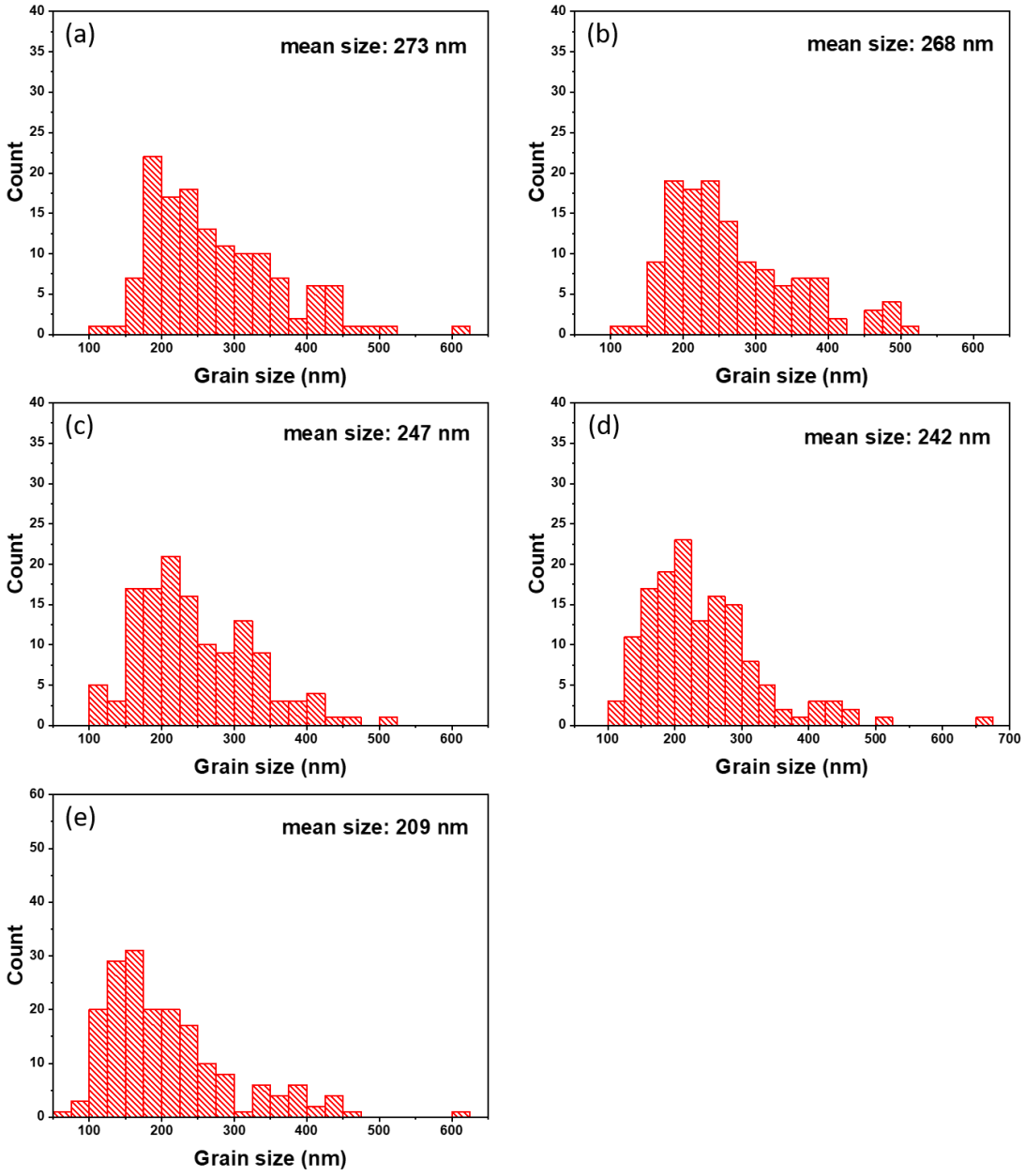

Figure 4.12. Grain size distribution of $MAPbI_3$ prepared by vacuum-assisted treatment with the temperature of 20 ℃ (a), 30 ℃ (b), 40 ℃ (c), 50 ℃ (d) and 60 ℃ (e).

And the mean size (Figure 4.12) decreased from 273 to 209 nm. The higher temperature not only increased the rate of solvent evaporation but also supplied more

heat for crystallization. From the LaMer model, we know that there is a competition between the nucleation and crystal growth. When the rate of solvent evaporation increased by higher temperature, the solution concentration had more time to keep above the minimum concentration of nucleation. It is known that the solubility of $MAPbI_3$ increases with the increasing temperature when it's below 60°C [127]. So the crystal growth was inhibited with the increasing temperature and the nucleation dominated. This helps explain the formation of more small crystals. But there were no dense films obtained when the temperature increased.

Instead, as shown in Figure 4.13, the pinhole densities of the $MAPbI_3$ films increased. This is not accord with the crystallization model of $MAPbI_3$ that we created before. In the experiments, it is important to note that the color of the films changed from transparent to light brown with the increasing temperature. This indicated that only MAI_2 ÞPbI$_2$ ÐDMSO intermediate phase formed after vacuum-assisted treatment at low temperature and more $MAPbI_3$ formed as the DMSO was removed from the intermediate phase after vacuum-assisted treatment at high temperature. This happened slowly when comparing with the post annealing at higher temperature, and caused an inhomogeneous crystallization. It might be the reason of pinholes formation.

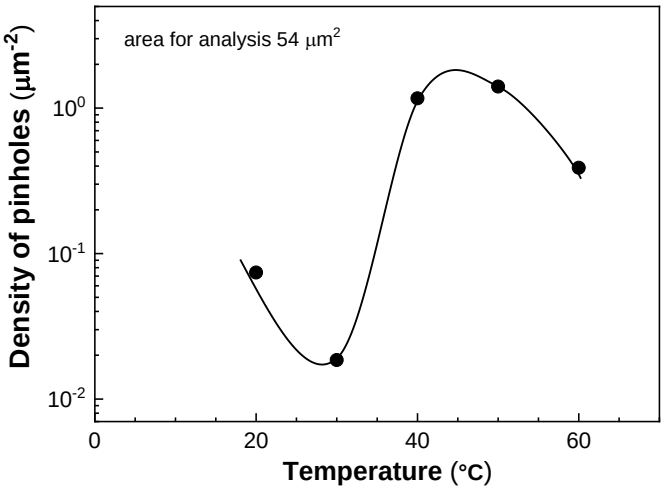

Figure 4.13. Pinhole densities of $MAPbI_3$ films as a function of temperature. The solid line is a guide for the eye.

4.3.2 Role of the temperature for the band gap and exponential tails of $MAPbI_3$

As before, we investigated the E_g and E_t of the $MAPbI_3$ layers prepared by vacuum-assisted treatment with different temperatures. Figure 4.14 shows in-phase and phase-shifted by 90 ° SPV spectra of $MAPbI_3$ prepared by vacuum-assisted treatment with the temperature of 20 ℃, 30 ℃, 40 ℃, 50 ℃ and 60 ℃. The amplitude of in-phase signals increased with the increasing temperature (except 50 ℃).

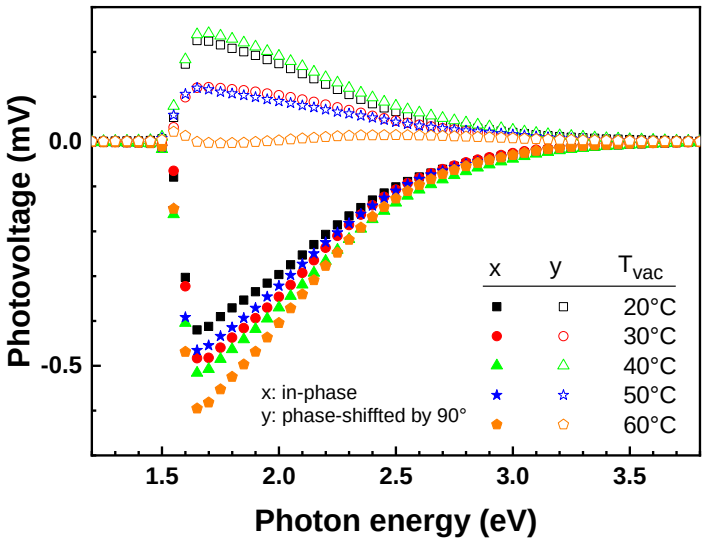

Figure 4.14. In-phase and phase-shifted by 90 ° overview surface photovoltage spectra of $MAPbI_3$ prepared by vacuum-assisted treatment with the temperature of 20 ℃, 30 ℃, 40 ℃, 50 ℃ and 60 ℃ (squares, circles, triangles, stars and pentagons respectively).

As shown in Figure 4.15, for the samples prepared with the temperature of 20 ℃, 30 ℃, 40 ℃, 50 ℃ and 60 ℃, the values of E_g were 1.571, 1.574, 1.56, 1.554 and 1.558 eV respectively. The overall trend of the band gap was decreasing when the temperature of vacuum-assisted treatment increasing and the maximum difference was 20 meV.

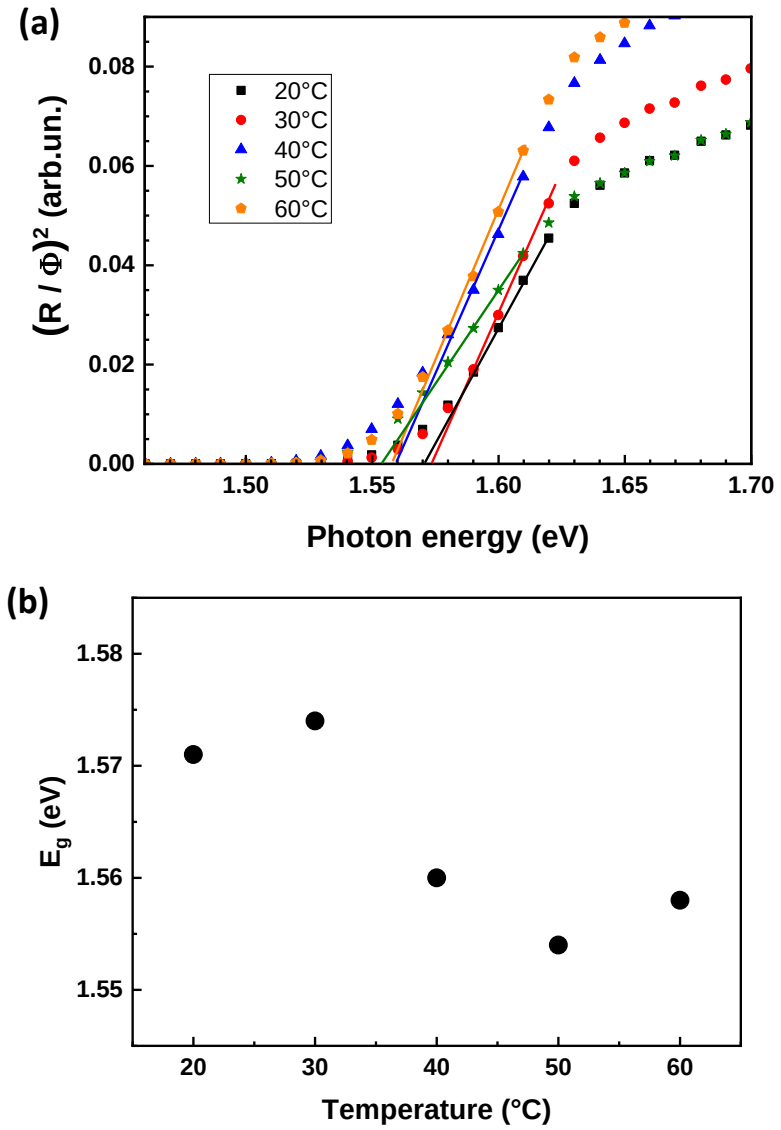

Figure 4.15. Tauc plots of the SPV amplitude spectra of $MAPbI_3$ layers prepared at temperature of 20 ℃, 30 ℃, 40 ℃, 50 ℃ and 60 ℃ (squares, circles, triangles, stars and pentagons respectively) (a) and band gaps as a function of the temperature (b).

The exponential tails of the $MAPbI_3$ layers prepared by vacuum-assisted treatment with different temperature were shown in Figure 4.16 (b). The corresponding values of E_t were amounted to 22, 20, 19, 18.5 and 17.5 meV for the temperature of 20 ℃, 30 ℃, 40 ℃, 50 ℃ and 60 ℃, respectively. This means the disorder of $MAPbI_3$ slightly decreased when the temperature of vacuum-assisted treatment increased.

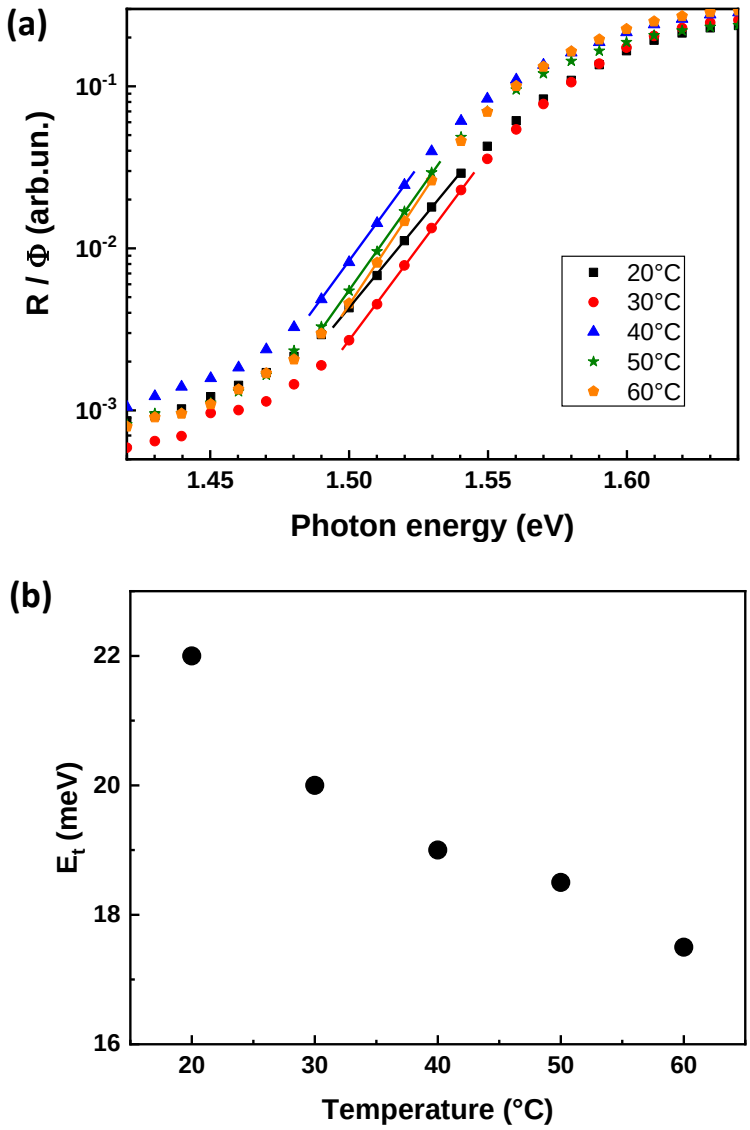

Figure 4.16. Spectra of the quotient of SPV amplitude and the photon flux on a logarithmic scale near the band gap of $MAPbI_3$ layers prepared at the temperature of 20 ℃, 30 ℃, 40 ℃, 50 ℃ and 60 ℃ (squares, circles, triangles, stars and pentagons respectively) (a) and exponential tails as a function of the temperature (b).

4.3.3 Role of the temperature for $MAPbI_3$ based solar cells

Figure 4.17 shows the J_{sc}, V_{oc}, FF and PCE of the solar cells based on the $MAPbI_3$ prepared by vacuum-assisted treatment with the temperature of 20 ℃, 30 ℃, 40 ℃, 50 ℃ and 60 ℃, respectively. As shown in Figure 4.17 (a), the highest PCE of 17.79% were obtained from the solar cells based on the $MAPbI_3$ prepared by vacuum-assisted treatment at 20 ℃. The values of average PCE for 20 ℃ and 30 ℃ were very close

(17.12% and 17.15% respectively). Then the values of average PCE decreased from 16.13% to 15.10%, when the temperature increased from 40 ℃ to 60 ℃. The solar cells for 30 ℃ also had the highest value of J_{SC} (21.24 mA/cm^2). And the value of average J_{SC} for 30 ℃ (20.86 mA/cm^2) was higher than that for 20 ℃ (20.69 mA/cm$_2$). For 40, 50 and 60 ℃, the values of average J_{SC} decreased to 19.96, 19.73 and 19.70 mA/cm^2, respectively.

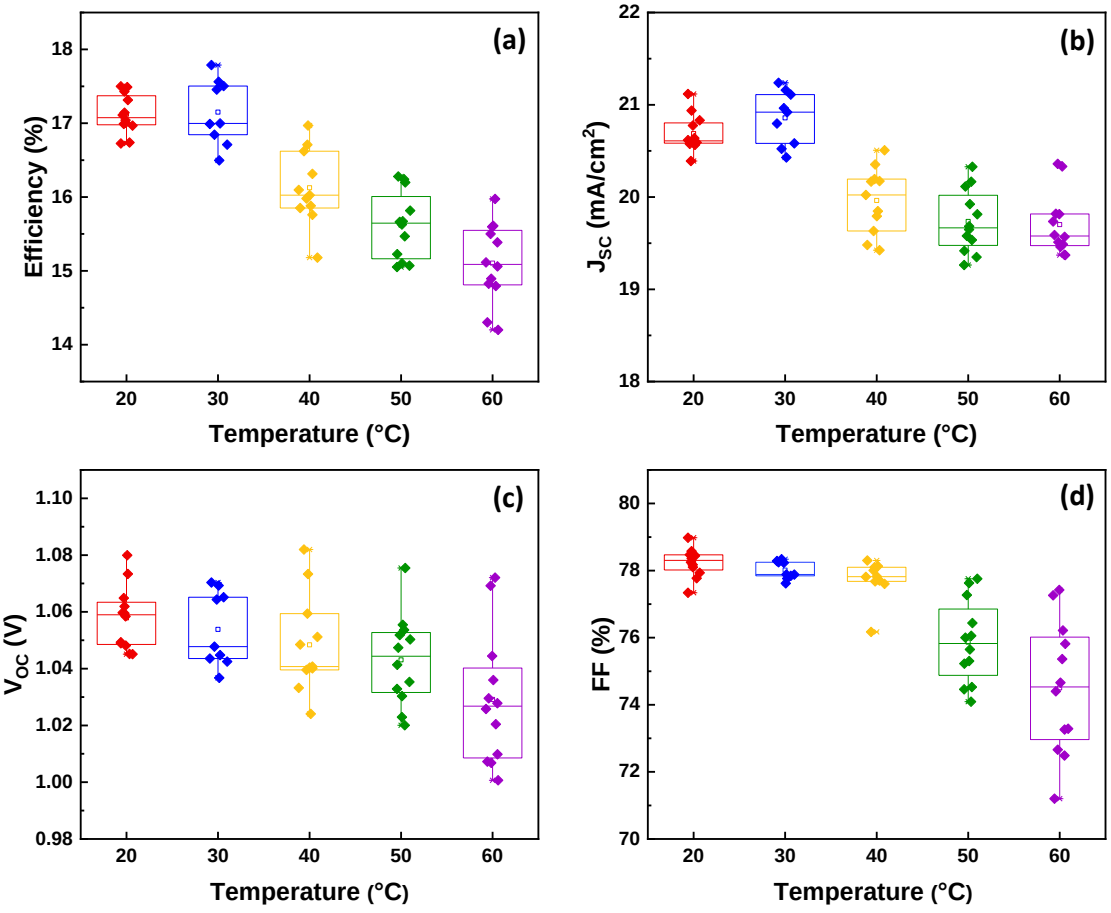

Figure 4.17. (a) power conversion efficiency (PCE), (b) short-circuit current density (J_{SC}), (c) open-circuit voltage (V_{OC}) and (d) fill factor (FF) of the solar cells based on the $MAPbI_3$ prepared by vacuum-assisted treatment with the temperature of 20 ℃, 30 ℃, 40 ℃, 50 ℃ and 60 ℃, respectively.

The maximum values of V_{OC} (Figure 4.17 (c)) for each temperature had little difference, which were between 1.07 and 1.08 V. The values of average V_{OC} had a trend of decline. The values of average FF for 20, 30 and 40 ℃ were also very close

(about 78%, Figure 4.17(d)). When the temperature increased to 50 and 60 ℃, the values of average FF decreased to 75.87% and 74.50%, respectively. And the deviation became much larger. The decline of the performance of $MAPbI_3$ solar cells could be attributed to two reasons. On one hand, the amount of grain boundaries increased as more small crystals formed, this created more obstruction for the charge carrier transporting and increased the recombination loss causing decrease of J_{SC} and V_{OC}. On the other hand, the shunt resistance was decreased by the formed pinholes and that led poor FF.

Then, we also compared the average values of the J_{SC} and J_{SC}^{max} from the $MAPbI_3$ solar cells with different measured band gap. As shown in Figure 4.18 (a), the J_{SCc} increased when the J_{SC}^{max} decreased with the increasing band gap. It also suggested that $MAPbI_3$ layer with less pinholes provided reduced the optical loss.

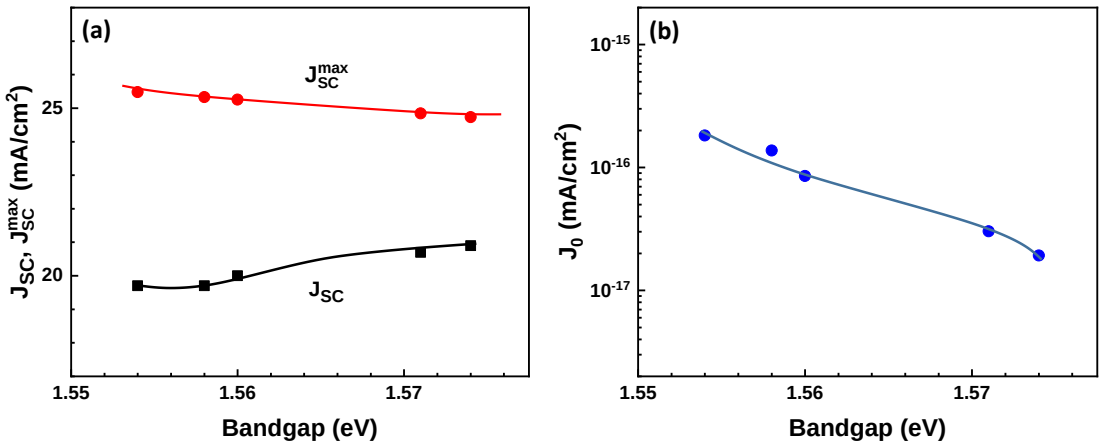

Figure 4.18. The average values of the measured short-circuit current densities (J_{SC}), the maximum values of the ideal short-circuit current densities (J_{SC}^{max}) and the diode saturation current density (J_0) of $MAPbI_3$ solar cells based on $MAPbI_3$ prepared by vacuum-assisted method with different temperature.

At last, the diode saturation current density (J_0) was studied. As shown in Figure 4.18 (b), J_0 decreased when the band gap increased. Combined with the previous result, the solar cells which showed better performance based on the $MAPbI_3$ were prepared at lower temperature.

4.4 Effect of the vacuum-assisted treatment time

More solvent will be removed in vacuum for a longer time. In this section, we expose the precursor solution layers to vacuum for different time, and studied the surface morphology, electronic properties and optical properties of $MAPbI_3$ prepared with different vacuum-assisted treatment time (the DMF/DMSO ratio and the temperature of vacuum-assisted treatment were kept at 9:1 and 30 ℃ respectively).

4.4.1 Effect of the vacuum-assisted treatment time for the morphology of $MAPbI_3$ layers

Figure 4.19 shows the SEM images of the $MAPbI_3$ films prepared by vacuum-assisted treatment with different time. From the top-view images, we can observe that, more and more small crystals appeared while the amount of crystal over 400 nm dropped off when the vacuum-assisted treatment time increased from 10 s to 600 s. And the mean size (Figure 4.20) decreased from 298 to 202 nm. In the experiments, we could observe that the color of precursor solution layer changed from transparent to light brown while the vacuum-assisted treatment time increasing. At longer time, more DMSO was removed from the rest solution, even from the $MAI \cdot PbI_2 \cdot DMSO$ intermediate phase. And that led a formation of $MAPbI_3$.

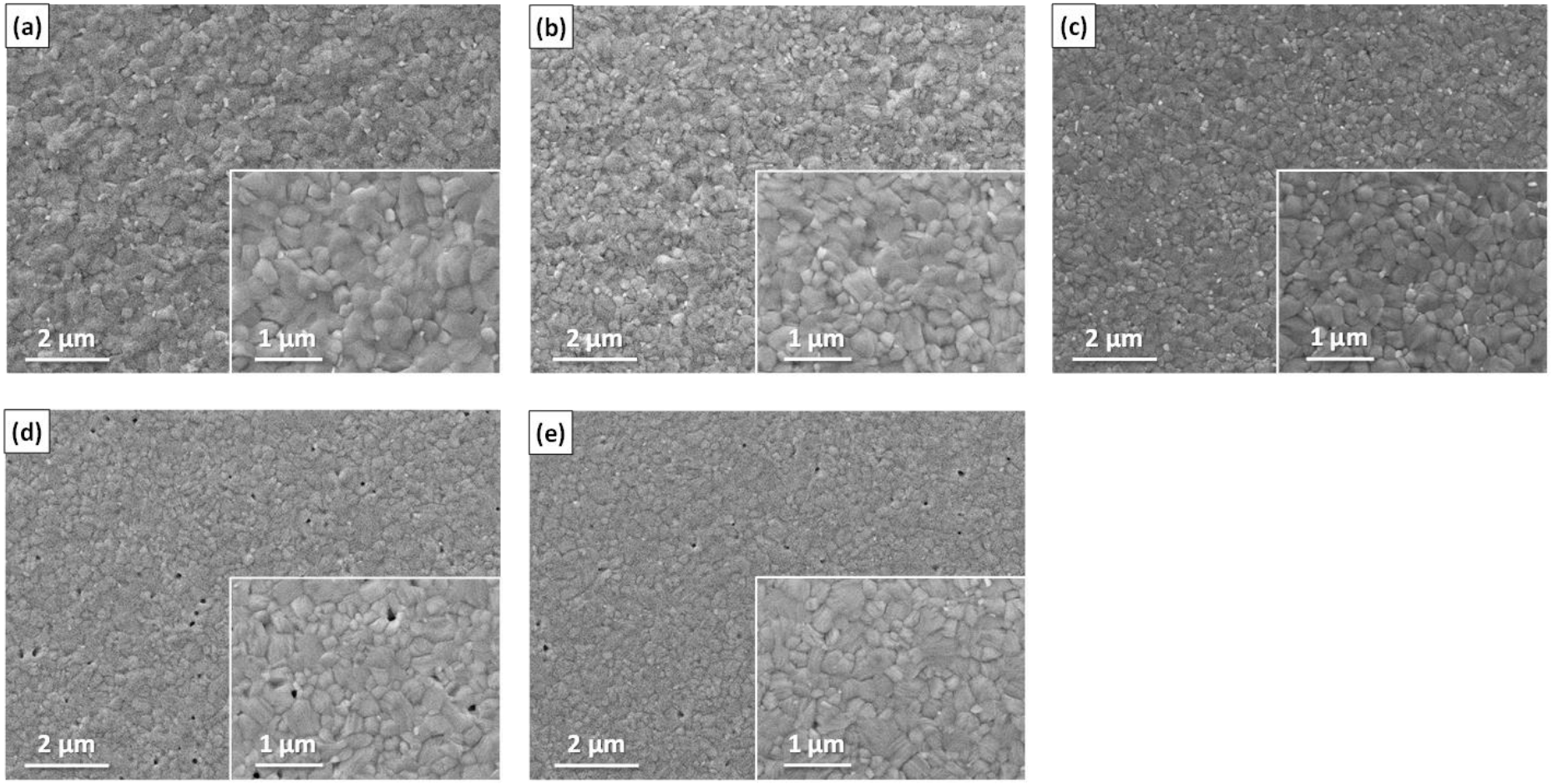

Figure 4.19. Surface view morphologies of the MAPbI3 films prepared by vacuum-assisted treatment with the time of 10 s (a), 30 s (b), 60 s (c), 300 s (d) and 600 s (e). The scale bars in all large images are 2 µm and the scale bars in all small images are 1 µm.

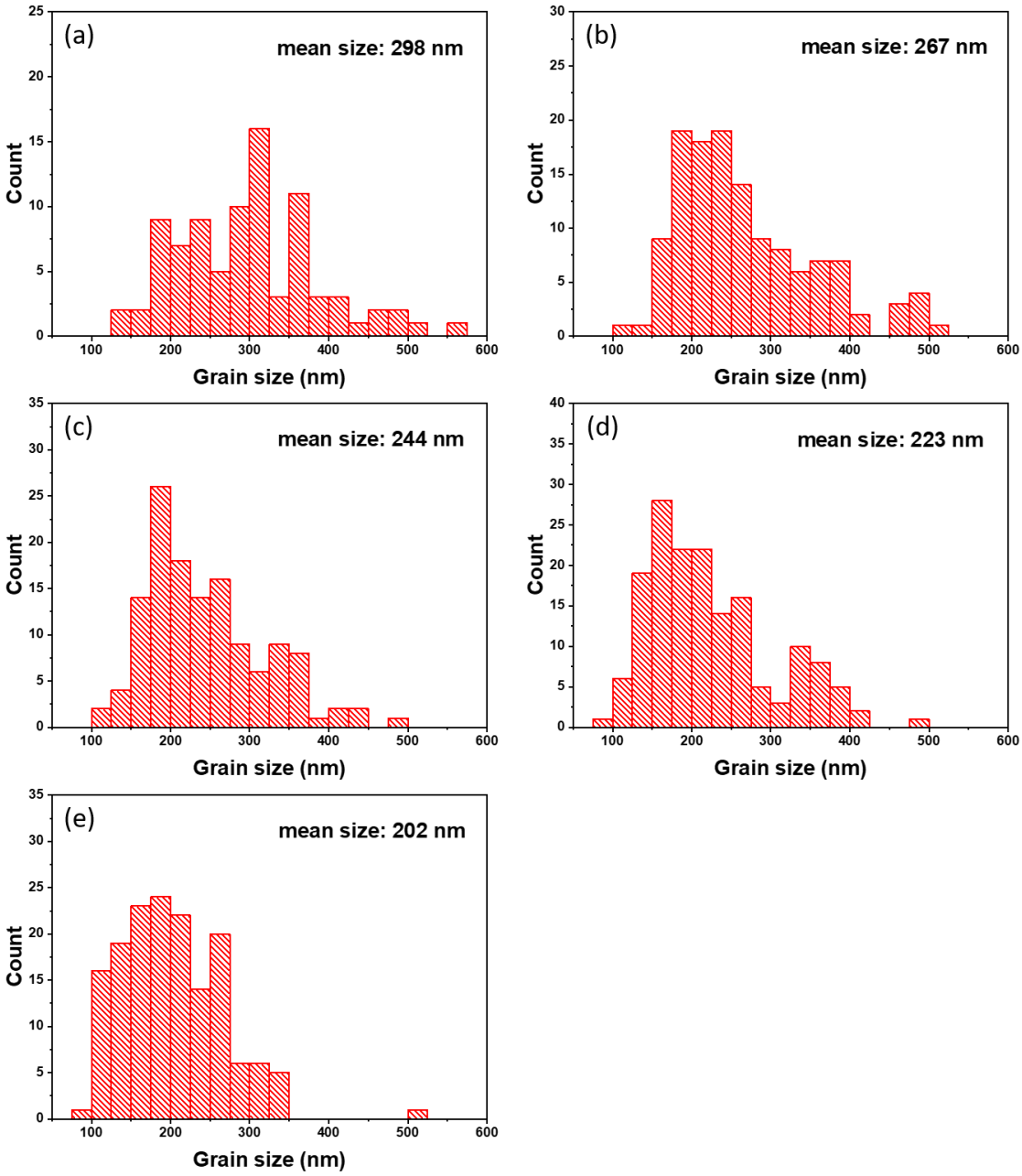

Figure 4.20. The grain size distribution of $MAPbI_3$ prepared by vacuum-assisted treatment with the time of 10 s (a), 30 s (b), 60 s (c), 300 s (d) and 600 s (e).

The precursor film became darker meant more $MAPbI_3$ formed and less intermediate phase left. After post annealing, more pinholes formed in the $MAPbI_3$ layers prepared with a longer vacuum-assisted treatment time (Figure 4.21). From the morphologies of prepared $MAPbI_3$ film, we can speculate the formation of $MAPbI_3$ before post annealing was not good for obtaining $MAPbI_3$ film with high quality.

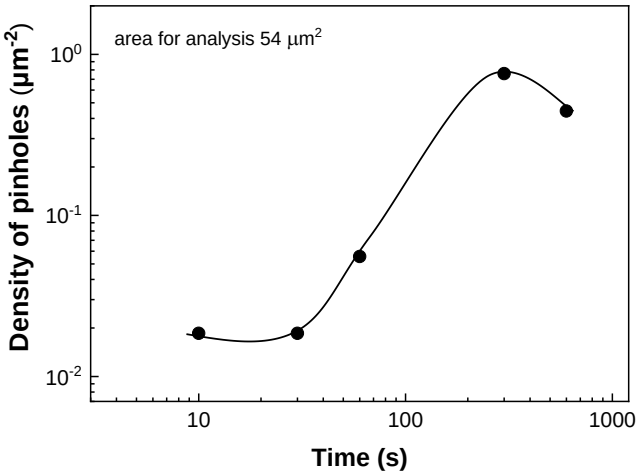

Figure 4.21. Pinhole densities of $MAPbI_3$ films as a function of time. The solid line is a guide for the eye.

4.4.2 Effect of the vacuum-assisted treatment time for the band gap and exponential tails of $MAPbI_3$

Finally, we investigated the band gap and exponential tails of $MAPbI_3$ layers prepared by vacuum-assisted treatment with different vacuum-assisted treatment time. Figure 4.22 shows in-phase and phase-shifted by 90 ° SPV spectra of $MAPbI_3$ prepared by vacuum-assisted treatment with the time of 10 s, 30 s, 60 s, 300 s and 600 s. And the amplitude of in-phase signals increased with the decreasing time.

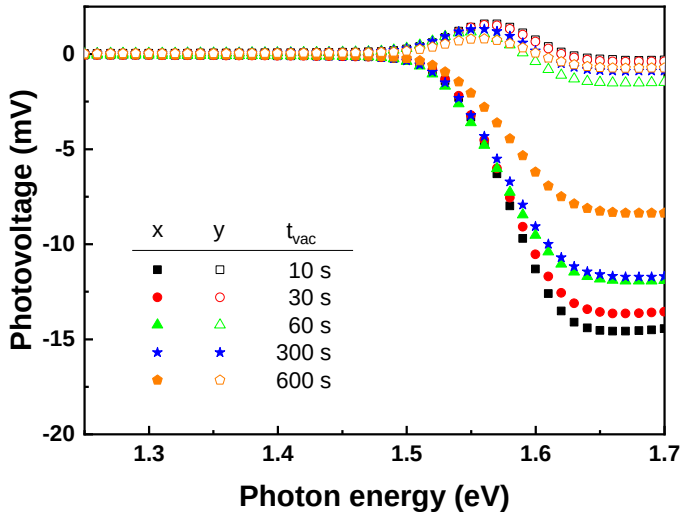

Figure 4.22. In-phase and phase-shifted by 90 ° overview surface photovoltage spectra of $MAPbI_3$ prepared by vacuum-assisted treatment with the time of 10 s, 30 s, 60 s, 300 s and 600 s (squares, circles, triangles, stars and pentagons respectively).

As shown in Figure 4.23 (b), for the samples prepared with the time of 10 s, 30 s, 60 s, 300 s and 600 s, the values of E_g were 1.563, 1.563, 1.562, 1.560 and 1.566 eV respectively. The band gap remained about the same. This indicated that the vacuum-assisted treatment time didn't have obvious impact on the band gap of the formed $MAPbI_3$ layers.

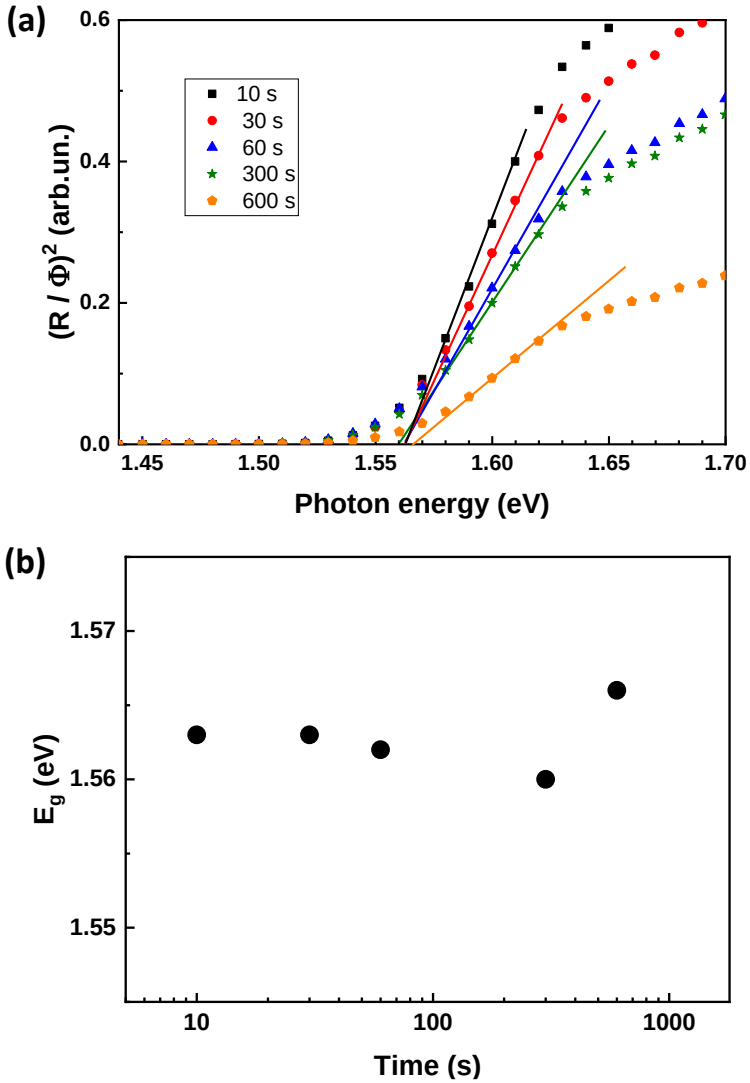

Figure 4.23. Tauc plots of the SPV amplitude spectra of $MAPbI_3$ layers prepared with the time of 10 s, 30 s, 60 s, 300 s and 600 s (squares, circles, triangles, stars, pentagons and hexagons respectively) (a) and band gaps as a function of the time (b).

The exponential tails of the $MAPbI_3$ layers prepared with different time of vacuum-assisted treatment were shown in Figure 4.24 (b). The corresponding values of E_t were amounted to 20.5, 20.5, 20.5, 20.5 and 21 meV for the time of 10 s, 30 s,

60 s, 300 s and 600 s, respectively. Similarly, the vacuum-assisted treatment time had a negligible effect on the disorder of the formed $MAPbI_3$ layers.

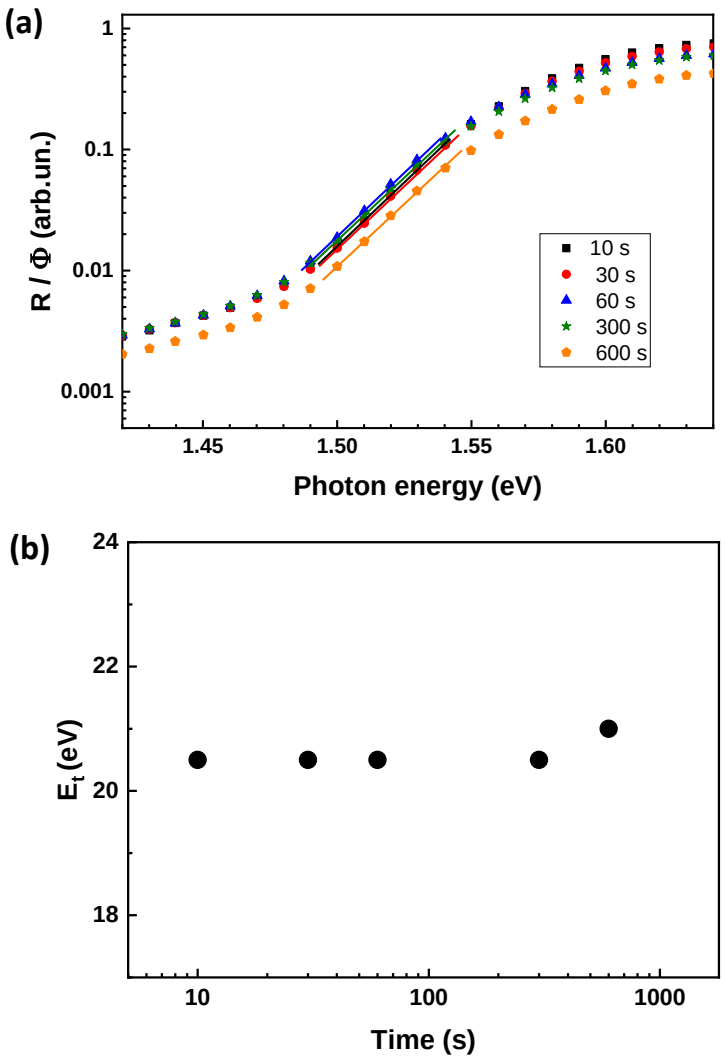

Figure 4.24. Spectra of the quotient of SPV amplitude and the photon flux on a logarithmic scale near the band gap of $MAPbI_3$ layers prepared with the time of 10 s, 30 s, 60 s, 300 s and 600 s (squares, circles, triangles, stars, pentagons and hexagons respectively) (a) and exponential tails as a function of the time (b).

4.4.3 Effect of the vacuum-assisted treatment time on $MAPbI_3$ based solar cells

Figure 4.25 shows the measured J_{SC}, V_{OC}, FF and PCE of the solar cells based on the $MAPbI_3$ prepared by vacuum-assisted treatment with the time of 10 s, 30 s, 60 s, 300 s

and 600 s, respectively. As shown in Figure 4.25 (a), the highest PCE of 17.80% was obtained from the solar cell based on the $MAPbI_3$ prepared by vacuum-assisted treatment at the time of 10 s. With the increasing time, the values of the average PCE were 17.45%, 17.17%, 17.26%, 16.43% and 14.99%, respectively. The highest J_{SC} of 21.48 mA/cm_2 was also obtained at the time of 10 s. The average values were 21.10, 20.77, 20.86, 20.47 and 19.38 mA/cm^2, respectively. And the average values of V_{OC} were 1.07, 1.07, 1.06, 1.05, and 1.02 V, respectively. There were decline trends in both of average values of J_{SC} and V_{OC}. In contrast, the highest FF of 78.89% and the highest average FF of 77.94% were both obtained from the solar cells prepared at the time of 60 s. The average values of FF increased when the vacuum-assisted treatment time increased from 10 s to 60 s. Then it decreased at a longer vacuum-assisted treatment time. Considering the little change of band gap, the decrease of V_{OC} could be attributed to more defects formed at the surface when the vacuum-assisted treatment increasing which affected the recombination rate. And the increased region around grain boundaries also could lead a decline of J_{SC}.

Then, we also compared the average values of the J_{SC} and J_{SC}^{max} from the $MAPbI_3$ solar cells with different measured band gap. As shown in Figure 4.26 (a), the J_{SC} increased when the J_{SC}^{max} decreased with the increasing band gap then turned to decreased at the band gap of 1.566 eV (It belonged to the $MAPbI_3$ layer prepared with a vacuum-assisted treatment time of 600 s). It also suggested that the optical loss increased again when the $MAPbI_3$ layer prepared with a long vacuum-assisted treatment time.

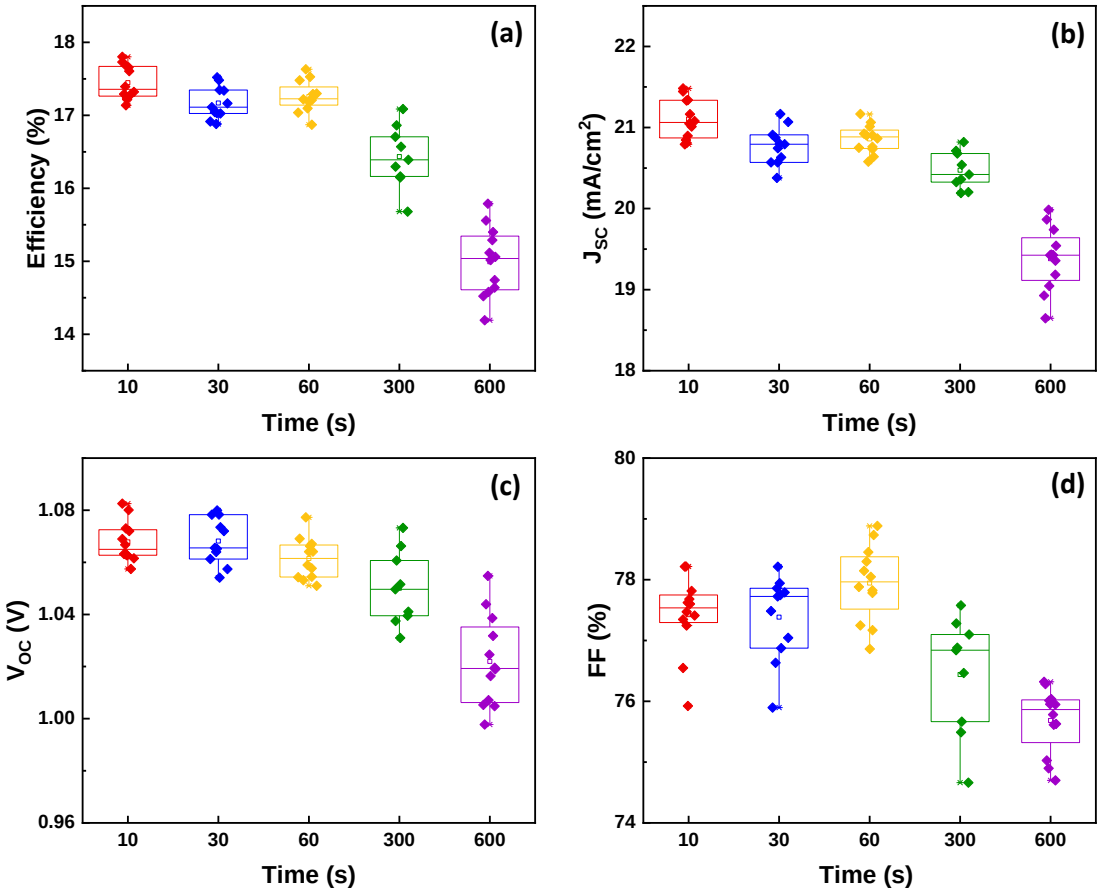

Figure 4.25. (a) power conversion efficiency (PCE), (b) short-circuit current density (J_{SC}), (c) open-circuit voltage (V_{OC}) and (d) fill factor (FF) of the solar cells based on the $MAPbI_3$ prepared by vacuum-assisted treatment with the time of 10 s, 30 s, 60 s, 300 s and 600 s, respectively.

At last, the diode saturation current density (J_0) was studied. As shown in Figure 4.26 (b), J_0 decreased when the band gap increased then increased at the band gap of 1.566 eV. Combined with the previous result, the solar cells which showed better performance based on the $MAPbI_3$ prepared at shorter vacuum-assisted treatment time.

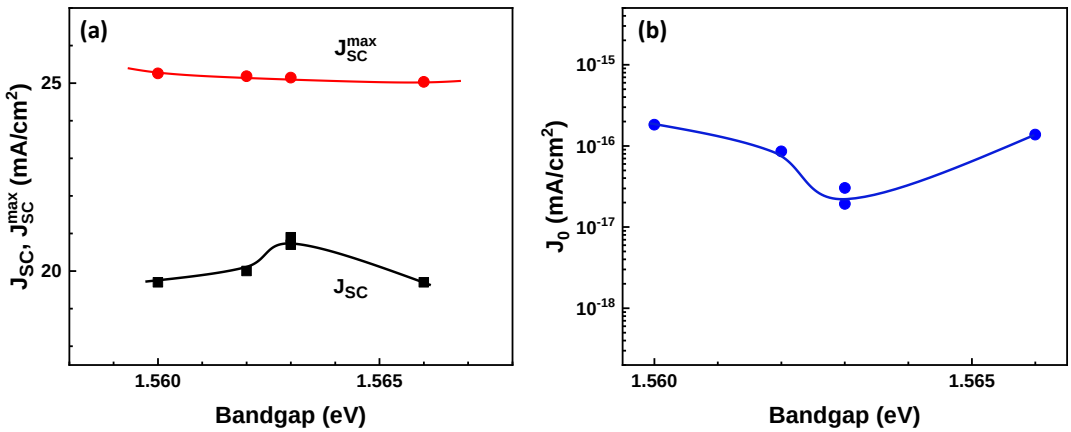

Figure 4.26. The average values of the measured short-circuit current densities (J_{SC}), the maximum values of the ideal short-circuit current densities (J_{SC}^{max}) and the diode saturation current density (J_0) of $MAPbI_3$ solar cells based on $MAPbI_3$ prepared by vacuum-assisted method with different vacuum-assisted treatment time.

4.5 Conclusions

For the vacuum-assisted method, it has been shown that the components of solvent, the temperature of substrate during the vacuum and the time of vacuum-assisted treatment all had influence on the morphologies and electronic bulk properties of the prepared $MAPbI_3$ layers, which affected the performance of $MAPbI_3$ solar cells. First, at fixed temperature (30 ℃) and vacuum-assisted treatment time (60 s), the solvent evaporation rate increased with the increasing DMSO proportion. From the LaMer model, this led to a shorter time of nucleation and a longer time of growth, which caused larger crystals and more pinholes formed. But the further increase of DMSO proportion led to the formation of small crystals and large clusters, and the reason was not clear yet. Second, at fixed solvent composition (DMF:DMSO = 9:1) and treatment time (60 s), the solvent evaporation rate increased with the increasing substrate temperature. However, the solubility was increased at the range of 20 ℃ to 60 ℃, which means the C_{min} was also increased. As a result, more small crystals formed with the increasing temperature. It was supposed that the nucleation period increased. The increased pinhole densities might be due to an inhomogeneous nucleation and growth at higher temperature (40-60 ℃). At last, at the fixed solvent composition

(DMF:DMSO = 9:1) and substrate temperature (30 ℃), a longer vacuum-assisted treatment time increased the nucleation period and reduced the growth period which led to the formation of more small crystals. More complete perovskite seeds formed as the solvent was removed from the intermediate. This might result in an inhomogeneous crystallization during post annealing which caused more pinholes formed.

In conclusion, higher DMSO proportion, higher substrate temperature and longer vacuum-assisted treatment time were all against the formation of high quality $MAPbI_3$ layer. The highest PCE of 17.8% was obtained from the solar cell based on the $MAPbI_3$ layer prepared with the optimized factors (DMF:DMSO = 9:1, 30 ℃, 10 s) at the given pressure of 60 pa.

5. Out-diffusion of solvent molecules during the formation of $MAPbI_3$

5.1 The solvent residue during the $MAPbI_3$ layer formation

Usually, γ-butyrolactone (GBL), N-methyl-2-pyrrolidone (NMP), DMF and DMSO are used as solvents for precursor solutions in solution-based deposition of organic/inorganic lead halide (PbX_2 where X= Cl, Br, I) perovskites. It is well known that lead halides can coordinate with monodentate (Y) and bidentate (YY) ligands to form five types of adducts: $PbX_2 \cdot Y$, $PbX_2 \cdot 2Y$, $2PbX_2 \cdot Y$, $PbX_2 \cdot YY$, and $PbX_2 \cdot 2YY$ whereas not all halides and ligands produced each type [128-129]. Incidentally, these kinds of adducts are also called Lewis acid−base adducts [130], where a base is defined as electron-pair donor and an acid as electron-pair acceptor (see the reaction in figure 5.1 a). In the solution, lead halides act as acceptors and the solvents act as donors (S-donors, O-donors, N-donors). DMSO, DMSF and NMP all belong to O-donors (see the chemical structures in figure 5.1 b).

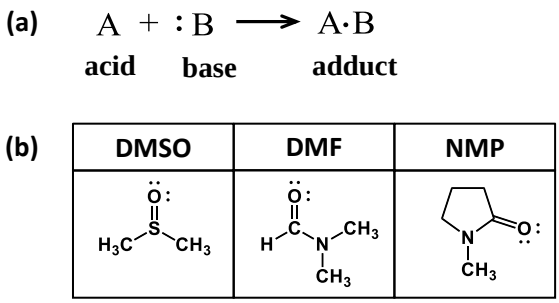

Figure 5.1. (a) Lewis acid (A) − base (B) reaction to form an adduct (A·B) with a dative bond, (b) Lewis bases (DMSO, DMF and NMP) with oxygen donor (O-donor).

The hard and soft acid-base concept, also known as Pearson acid-base concept, is widely used in chemistry for explaining stability of compounds, reaction mechanisms and pathways. It assigns the terms 'hard' or 'soft', and 'acid' or 'base' to chemical species. 'Hard' applies to species which are small, have high charge states (the charge criterion applies mainly to acids, to a lesser extent to bases), and are weakly

polarizable. 'Soft' applies to species which are big, have low charge states and are strongly polarizable [131]. In this concept, Pb(II) is classified as borderline soft, and therefore should bind more strongly with soft S-donors than with hard O-donors. Pb(II) is probably made even softer by symbiosis [132] with the surrounding halogen atoms, an effect which should decrease in the order I > Br > Cl, and hence acceptor powers should decrease in the order PbI_2 > $PbBr_2$ > $PbCl_2$. For the same O-donors, seen from the chemical structures, DMSO is expected to have the strongest Lewis basicity due to the electron donating supported by the nearest methyl group [10]. And NMP has the second strongest Lewis basicity due to the support from conjugated electrons [133]. As Lewis base, their basicity also correlated with the donor number (D_N). The Gutmann's donor number is defined as the negative enthalpy value for the 1:1 adduct formation between a Lewis base and the standard Lewis acid $SbCl_5$ in dilute solution in the non-coordinating solvent 1,2-dichloroethane. And the larger D_N implies the stronger basicity. From the previous study, the D_N of DMSO, NMP and DMF are 29.8, 27.3 and 26.6 kcal/mol respectively [134]. Therefore, the strength of dative bond with PbI_2 is supposed to be DMSO > NMP > DMF.

Although DMF can form intermediate adducts with lead halides such as PbI_2·DMF, it is unstable due to the relative weak dative bond with PbI_2. Part of the MAI·PbI_2·DMF converts into $MAPbI_3$ before post annealing. This leads to inhomogeneous crystallization. Finally, a dendritic perovskite film forms. The addition of DMSO can help with improving the stability of intermediate adducts by forming MAI·PbI_2·DMSO. In previous reports, mixed DMF/DMSO as solvent was usually used in precursor solution for preparing high-quality perovskite film [135-138]. When preparing the perovskite film with one step spin coating, most of the solvent is removed during or after the spin coating by anti-solvent dripping, hot casting, solvent bathing or vacuum-assisted evaporation. Therefore the intermediate adduct formed before post annealing, and it plays a crucial role in controlling the morphology.

As shown in Fig. 5.2, at the initial stage during spin coating, the film was composed

of MAI and PbI_2 dissolved in the DMF/DMSO solvent mixture, whereas in the intermediate stage, the composition of the film was concentrated by the evaporation of DMF and DMSO. Then the vacuum-assisted evaporation led to the immediate freezing of the constituents after spin coating via the quick removal of the excess DMF and DMSO solvent and the rapid formation of the MAI‧PbI_2‧DMSO adduct (also a few amount of MAI‧PbI_2‧DMF adduct), leaving a uniform and transparent thin layer. The role of DMSO (DMF) in the MAI‧PbI_2‧DMSO adduct (MAI‧PbI_2‧DMF adduct) is to retard the rapid reaction between PbI_2 and MAI during the evaporation of solvent in the spin coating vacuum process. Finally, a uniform, compact and pure crystalline $MAPbI_3$ pervoskite film was obtained after post annealing. In this process, the key material is the film consisting of MAI‧PbI_2‧DMSO.

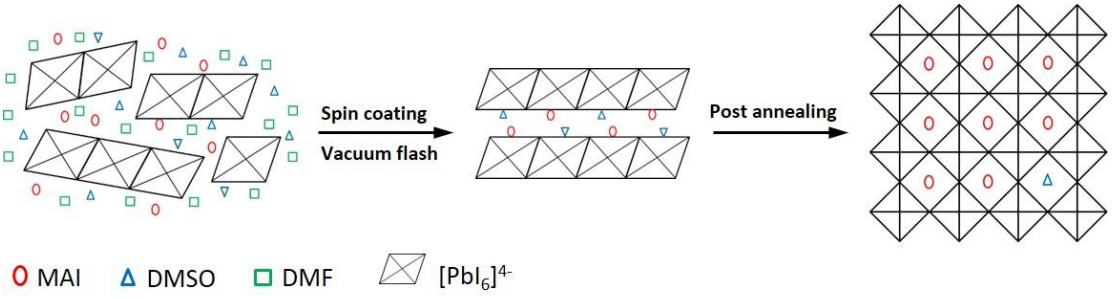

Figure 5.2 Scheme for the formation of the perovskite material via the MAI•PbI_2•DMSO intermediate adduct. Adapted by permission from ref [9]. Copyright (2014) Springer Nature Customer Service Centre GmbH.

During the $MAPbI_3$ film formation, most of the combined DMSO evaporate via post annealing. But the evaporation of DMSO is limited by their transport through the forming layer and a few DMSO will stay in the perovskite even after post annealing. Periodic DFT calculations were performed to get information about the stability of DMSO molecules trapped inside the $MAPbI_3$ structure. Figure 5.3 shows the computational model of the perfect $MAPbI_3$ structure, the $MAPbI_3$ structure with a MA^+ vacancy, and the $MAPbI_3$ structure with a DMSO molecule trapped at the position of the MA^+ vacancy. The binding energy of DMSO molecules trapped at the

position of the MA^+ vacancy was found to be -3.58 eV. Therefore, DMSO molecules incorporated into a perovskite crystal during the crystal growth are stable.

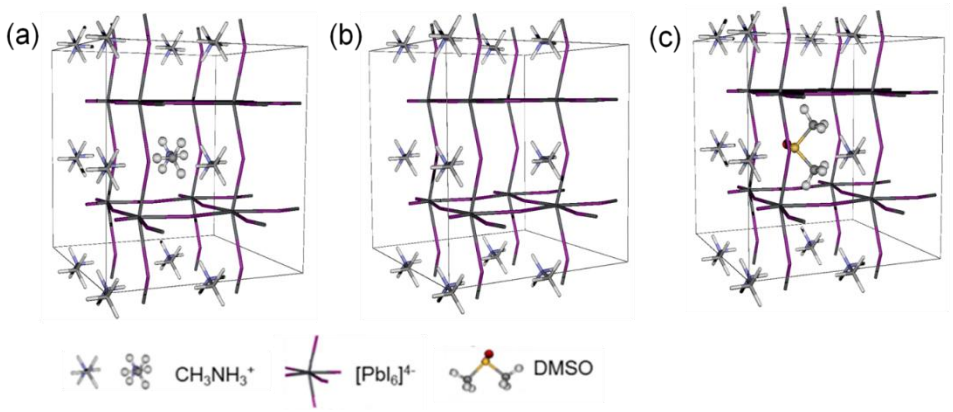

Figure 5.3 Ideal structure of $MAPbI_3$ (a), structure of $MAPbI_3$ with a MA^+ vacancy (b), and structure of $MAPbI_3$ with a DMSO molecule trapped at the position of the MA^+ vacancy (c) as calculated by DFT simulations.

The residual quantity depends on the annealing temperature and annealing time. As so far, only little is known about residual solvent molecules in metal halide perovskite layers and their influence of on the electronic properties of perovskites.

5.2 Model for diffusion of solvent molecules in a $MAPbI_3$ layer

The concentration of solvent molecules in the perovskite precursor layer can be assumed to be homogeneous across the layer thickness (d) before annealing. During annealing, solvent molecules disappear via the interface of the perovskite layer with the ambient atmosphere whereas solvent molecules do not disappear via the interface with the substrate. Therefore, the evolution of the concentration of solvent molecules in the perovskite layer can be simulated with a simple one-dimensional diffusion model including reflecting boundary conditions at the internal interface (x = 0) and a sink at the external interface (x = d).

The one-dimensional diffusion equation, also called 'Fick's second law of diffusion', which relates the rate of change of concentration at a point to the spatial variation of the concentration at that point:

$$\frac{\partial c}{\partial t} = \mathrm{D}\frac{\partial^2 c}{\partial x^2}, \qquad x \in (0, d), t \in (0, T) \qquad (5.1)$$

Where c is the population density, $\mathrm{c}(x, t)$ is a unknown function that depends on location x and time t, D is the diffusion coefficient and determines how fast c changes in time. For our experiments, the one-dimensional diffusion equation with a source term was simulated with the simple recursion formalism.

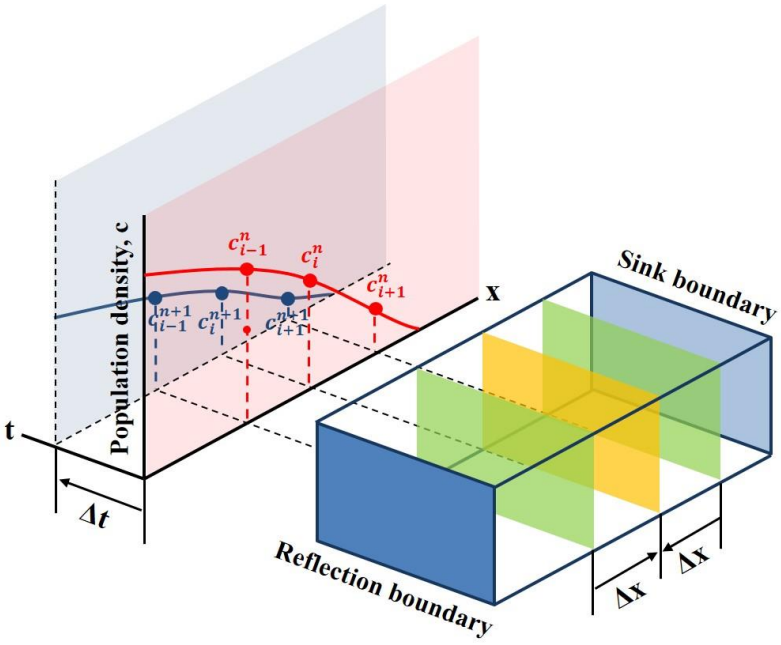

Figure 5.4 The changes of population density depend on diffusion length and time.

The first step in the discretization procedure is to replace the domain $(0, \mathrm{d}) \times (0, \mathrm{T})$ by a set of mesh points. As shown in Fig. 5.4, we apply equally spaced mesh points:

$$x_i = i\Delta x,\ i = 0, \ldots, N_x, \text{ and } t_i = n\Delta t,\ n = 0, \ldots, N_t$$

Moreover, c_i^n denotes the mesh function that approximates $\mathrm{c}(x_i, t_n)$ for $i = 0, \ldots, N_x$ and $n = 0, \ldots, N_t$. Requiring equation 5.1 to be fulfilled at a mesh point (x_i, t_n) leads to the equation:

$$\frac{\partial}{\partial t}c(x_i, t_n) = \mathrm{D}\frac{\partial^2}{\partial x^2}c(x_i, t_n) \qquad (5.2)$$

The next step is to replace the derivatives by finite difference approximations. The computationally simplest method arises from using a forward difference in time and a central difference in space, written out:

$$\frac{c_i^{n+1} - c_i^n}{\Delta t} = \mathrm{D}\frac{c_{i+1}^n - 2c_i^n + c_{i-1}^n}{\Delta x^2} \qquad (5.3)$$

We have turned the equation 5.1 into algebraic equations, also often called discrete equations. The key property of the equations is that they are algebraic, which makes them easy to solve. As usual, we anticipate that c_i^n is already computed such that c_i^{n+1} is the only unknown in equation 5.2. Solving with respect to this unknown is easy:

$$c_i^{n+1} = c_i^n + F(c_{i+1}^n - 2c_i^n + c_{i-1}^n) \qquad (5.4)$$

$\mathrm{F} = \mathrm{D}\Delta t/\Delta x^2$ is the key parameter in the discrete diffusion equation. Note that F is a dimensionless number that lumps the key physical parameter in the problem, D and the discretization parameters Δx and Δt into a single parameter. All the properties of the numerical method are critically dependent upon the value of F. In our experiments, equations of the boundary conditions are:

Internal surface: $c_{i=0}^{n+1} = c_{i=0}^n + \mathrm{F}(\mathrm{c}_{i=1}^n - 2\mathrm{c}_{i=0}^n)$ (5.5)

External surface: $c_{i=N_x}^{n+1} = c_{i=N_x}^n + \mathrm{F}\left(\mathrm{c}_{i=N_x-1}^n - 2\mathrm{c}_{i=N_x}^n\right)$ (5.6)

The diffusion coefficient (D) of molecules in solids is of the order of 10^{-30} – 10^{-9} cm²/s. A similar range can be expected for the diffusion coefficients of solvents in perovskite. The insert of figure 5.5 shows the depth dependencies of the concentration for a layer thickness of 200 nm after different times of diffusion with a diffusion coefficient of 10^{-11} cm²/s.

The time dependencies of the integrated concentrations are depicted in figure 5.5 for different values of D. At longer times, the decay of the integrated concentrations can

be well fitted with an exponential (decay time constant τ). This opens the opportunity for fast and robust analysis.

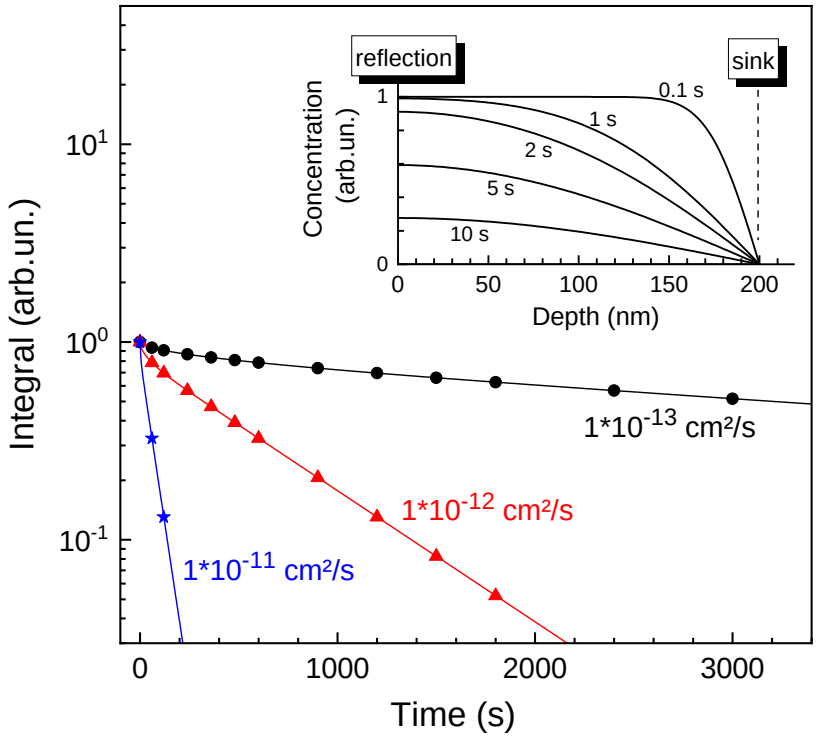

Figure 5.5 Depth dependencies of the concentration for a layer thickness of 200 nm after different times of diffusion (insert) and time dependencies of the concentrations integrated over the depth for diffusion coefficients of $1 \cdot 10^{-11}$ cm²/s, $1 \cdot 10^{-12}$ cm²/s and $1 \cdot 10^{-13}$ cm²/s (stars, triangles and spheres, respectively). The reflection and sink boundary conditions at the internal interface and at the interface to the ambient are marked the insert. At longer times, the decay of the integrated concentrations can be well fitted with an exponential.

The ratio of the squared thickness (d^2) and τ is correlated with the corresponding values of D in figure 5.6(a). There is a straight slope in the double logarithmic scale, i.e. d^2/τ is proportional to D whereas the proportionality factor is about 1.64 for analysis at longer times (D larger than 10^{-13} cm²/s, figure 5.6 (b)). For the given work, the accuracy of the proportionality factor of 1.6 is sufficient with respect to the accuracy of measurements, i.e.

$$D \approx 1.6 \cdot \frac{d^2}{\tau} \qquad (5.7)$$

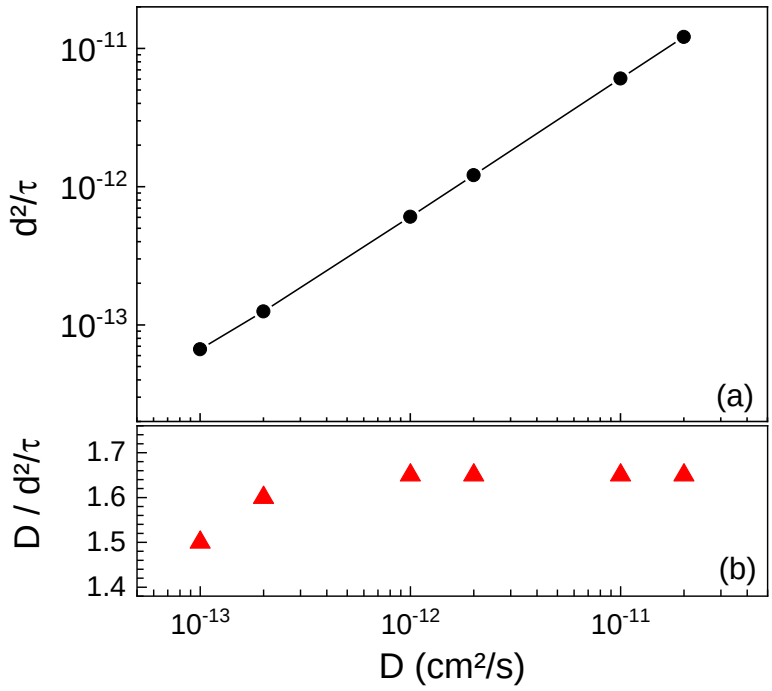

Figure 5.6 Correlations of the squared layer thickness divided by the decay time constant (a) and of the diffusion coefficient divided by the squared layer thickness divided by the decay time constant with the corresponding diffusion coefficient (b).

5.3 Detecting the absolute value of residual solvent (DMSO) in $MAPbI_3$ layers by HR-CSAS

The absolute amount of residual DMSO in $MAPbI_3$ layer was detected by the high-resolution continuum source absorption spectrometry (HR-CSAS). As shown in table 5.1, the amount of DMSO and Pb in each sample annealed at 100 ℃ with different time was measured. The similar amount of Pb indicated that each sample contained the similar amount of $MAPbI_3$, that is, these $MAPbI_3$ layers had good reproducibility of thickness and area. Besides, the existence of S suggested that there were still residual DMSO in the $MAPbI_3$ layer even after 10 min annealing. However, the amount of S decreased with the annealing time increasing. These results showed

that HR-CSAS can measure the amount of residual DMSO very accurately. But considering the complex sample preparation, more simple and straightforward method should be used.

Table 5.1 Sulfur amount in $MAPbI_3$ layers with different annealing time.

Annealing time (min)	S (μmol)	Pb (μmol)	Molar ratio (S / Pb)
1	0.021	1.52	1.38%
5	0.0065	1.48	0.44%
10	0.0037	1.58	0.23%

5.4 Infrared absorption analysis of $MAPbI_3$ layers

The direct investigation of the diffusion of solvent molecules in forming metal halide perovskite layers is extremely challenging due to the need for selectivity of investigated molecules and for avoiding disturbances in the investigated samples by the measurement technique. As some solvent molecules contain specific chemical bonds and bond configuration with specific vibration modes (e.g. DMSO contains S=O), which can be investigated by infrared spectroscopy.

The IRSE (infrared spectroscopic ellipsometry) spectra are sensitive to the integrated concentrations of residual solvent molecules (such as DMSO or DMF) diluted in the perovskite layer. Figure 5.7 shows IRSE spectra of $MAPbI_3$ layers annealed at 100 ℃ for 1 min and for 30 min. For this annealing temperature and annealing time, some of the lines of the IRSE spectra disappeared within the resolution of IRSE after the annealing whereas some of the lines stayed permanent. The positions of the peaks disappearing or staying permanent after annealing were identical for all samples, i.e. independent of annealing temperature and annealing time.

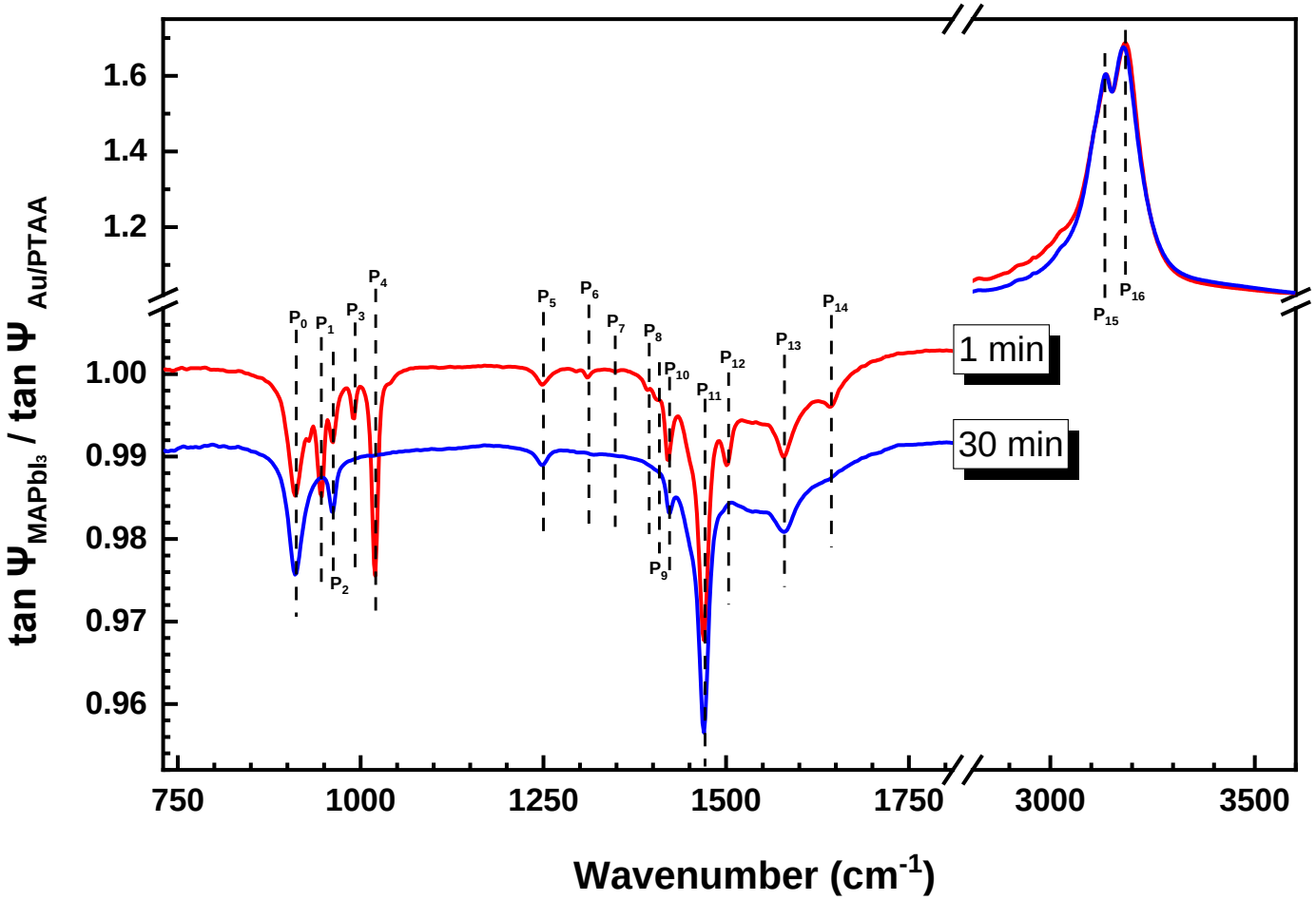

Figure 5.7 IRSE spectra of MAPbI3 layers annealed at 100 ℃ for 1 min (red line) and for 30 min (blue line), the most prominent peaks are labeled by numbers and described in table 5.2.

The peaks disappearing after 30 min annealing had their maxima at 945, 991, 1020, 1310, 1349, 1392, 1406, 1501 and 1642 cm^{-1}. The peaks staying permanent after 30 min annealing had their maxima at 911, 962, 1248, 1420, 1468, 1578, 3138 and 3182 cm^{-1}.

Table 5.2 Measured resonance frequencies of vibrational modes and peak assignments for the prepared perovskite layer with residual solvents ($MAPbI_3$/DMSO/DMF).

mode label	frequency (cm^{-1})	description	assignment
P_0	911	$\rho(CH_3\text{-}NH_3^+)$	$MAPbI_3$
P_1	945	$\rho(CH_3)$	DMSO
P_2	962	ν(C-N)	$MAPbI_3$
P_3	991	$\rho'(CH_3)$	DMSO
P_4	1020	ν(S=O)	DMSO
P_5	1248	$\rho'(CH_3\text{-}NH_3^+)$	$MAPbI_3$
P_6	1310	$\delta_s(CH_3)$	DMSO
P_7	1349	$\delta_s(CH_3)$C	DMF
P_8	1392	$\delta_s(CH_3)$N	DMF
P_9	1406	$\delta_{as}(CH_3)$	DMSO
P_{10}	1420	δ_{as}'(CH_3)	$MAPbI_3$
P_{11}	1468	$\delta_s(NH_3^+)$	$MAPbI_3$
P_{12}	1501	ν(C-N)	DMF
P_{13}	1578	$\delta_{as}(NH_3^+)$	$MAPbI_3$
P_{14}	1642	ν(C=O)	DMF
P_{15}	3138	ν_s(N-H)	$MAPbI_3$
P_{16}	3182	ν_{as}(N-H)	$MAPbI_3$

As shown in table 5.2, the peaks at 945, 991, 1020, 1310 and 1406 cm^{-1} can be assigned to DMSO whereas the largest peak at 1020 cm^{-1} is related to the S=O stretching mode. The peak at 1349, 1392, 1501 and 1642 cm^{-1} can be assigned to

DMF. Among them the peak at 1642 cm^{-1} is related to the C=O stretching mode. The peaks staying permanent after annealing are related to vibrations of CH_3-NH_3^+ (rocking modes at 911 and 1248 cm^{-1}), C-N (stretching modes at 962 cm^{-1}), CH_3 (asymmetric bending modes at 1420 cm^{-1}), NH_3^+ (symmetric and asymmetric bending modes at 1468 and 1578 cm^{-1}) and N-H (symmetric and asymmetric stretching modes at 3138 and 3182 cm^{-1}, incidentally, due to the overlapping with the thickness interference the band point upwards). These peaks can be assigned to MAI [139-143].

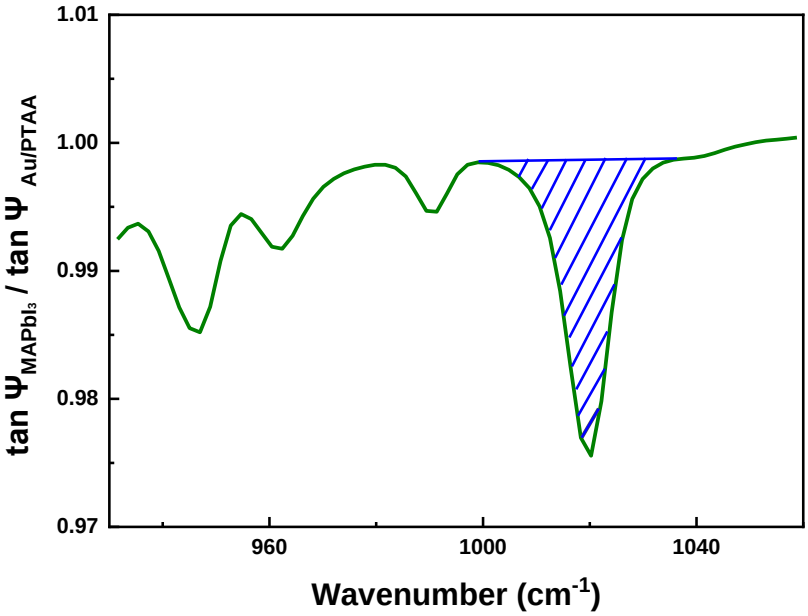

Figure 5.9 Schematic of peak integration in IRSE spectrum.

IRSE spectrum can not only be used to detect the existence of residual solvents in $MAPbI_3$ layer but also to quantify the relative solvent residue by calculating the integral amplitude of peaks (seen in figure 5.9) which can be assigned to the solvents (such as DMSO).

In figure 5.10, the DMSO residue measured by IRSE (integral amplitudes) increased with the increase of that measured by HR-CSAS (molar ratio of S/Pb, amount of Pb is constant), and they could be well fitted with a linear relationship. This illustrates that describing the change of DMSO residue in $MAPbI_3$ layers by integral amplitudes from IRSE measurement is reliable and any absolute amount of residue DMSO can be

calculated from the IRSE analysis results by this linear relationship.

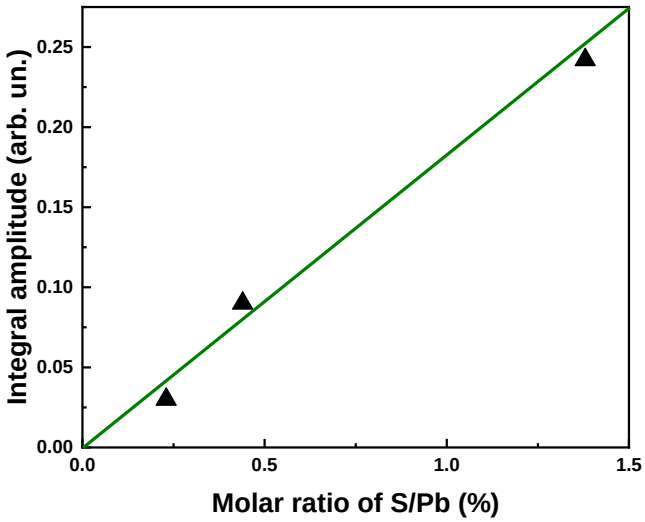

Figure 5.10 The Change of DMSO residue in $MAPbI_3$ layers with increasing annealing time, detected by HR-CSAS and IRSE respectively, the green line a linear fitting.

5.5 Analysis of solvents diffusion in $MAPbI_3$ layers

5.5.1 Analysis of DMSO diffusion in $MAPbI_3$ layers

In IRSE spectrum of $MAPbI_3$ layer, we quantify the relative DMSO residue by calculating the integral amplitude of peaks which can be assigned to DMSO. Figure 5.11 shows IRSE spectra of $MAPbI_3$ layers annealed at 100 ℃ for 1, 2, 4, 6, 8 and 15 min in a reduced spectral range of 930 to 1050 cm^{-1} and 2500 to 4000 cm^{-1}. In these ranges, CH_3 rocking modes at 945 and 991 cm^{-1} (in DMSO), C-N stretching mode at 962 cm^{-1} (in MAI), S=O stretching mode at 1020 cm^{-1} (in DMSO) and symmetric and asymmetric N-H stretching modes at 3138 and 3182 cm^{-1} are well resolved. With the annealing time increased, the peak amplitudes related to DMSO weakened and eventually disappeared after 15 min of annealing. In the same time, the peak amplitudes related to $MAPbI_3$ were invariable. This indicates that DMSO residue escaped from the $MAPbI_3$ layer while the $MAPbI_3$ kept stable.

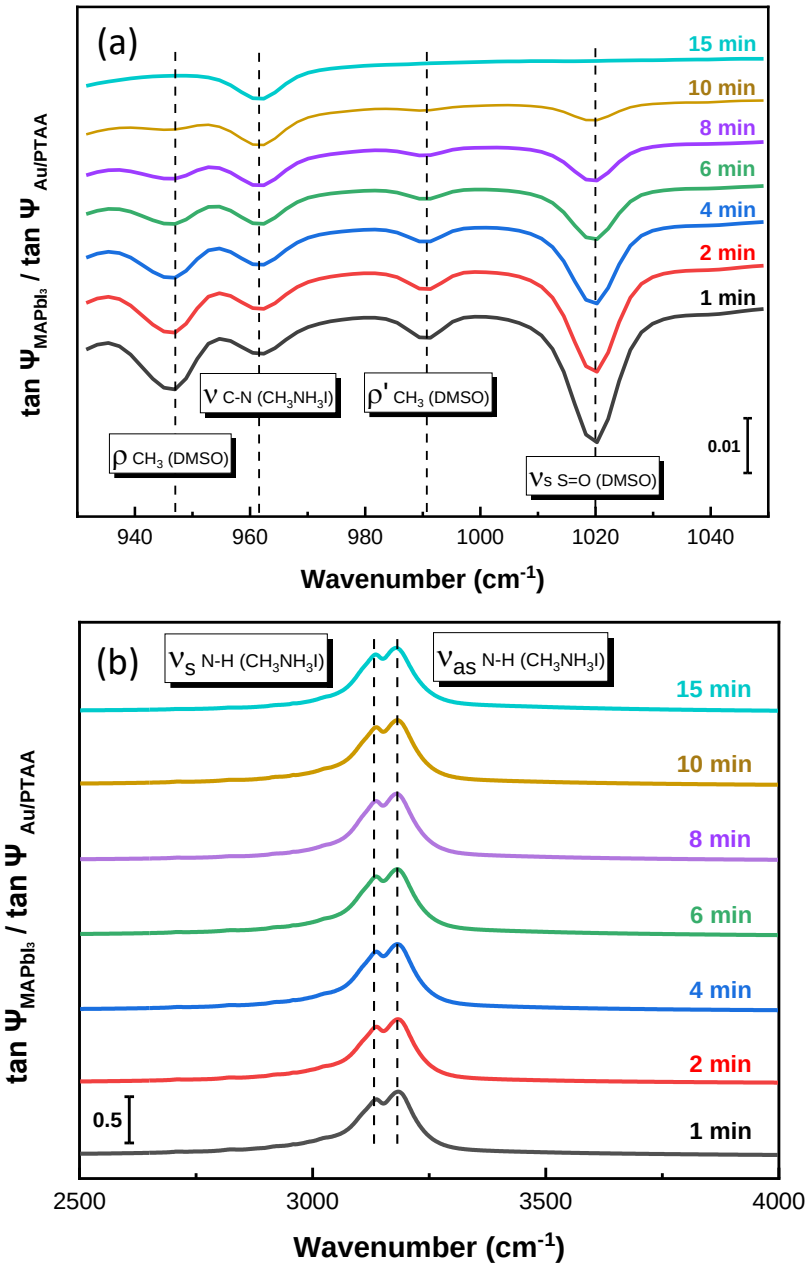

Figure 5.11 IRSE spectra of $MAPbI_3$ layers annealed at 100 ℃ for 1 (grey line), 2 (red line), 4 (blue line), 6 (green line), 8 (purple line), 10 (brown line) and 15 (cyan line) min in the spectral range of 930 – 1050 cm^{-1} (a) and 2500 – 4000 cm^{-1} (b), the prominent peaks are labeled.

Figure 5.12 makes the DMSO residue more visually change. In figure 5.12 (a), we can observe that the peak amplitudes related to CH_3 and S=O in DMSO decreased with increasing annealing time and were below the resolution of IRSE after annealing for 15 min. Whereas in figure 5.12 (b), the peak amplitudes related to CH_3 and N-H in

MAI were independent of annealing. Among these peaks related to DMSO, the peak at 1020 cm^{-1} (S=O stretching mode) was usually regarded as the fingerprint peak of DMSO in IR spectrum analysis. And because of the larger amplitude and change, it was suitable to be applied for DMSO residue analysis. Thus, we quantify the relative DMSO residue by integrating the amplitude of this peak.

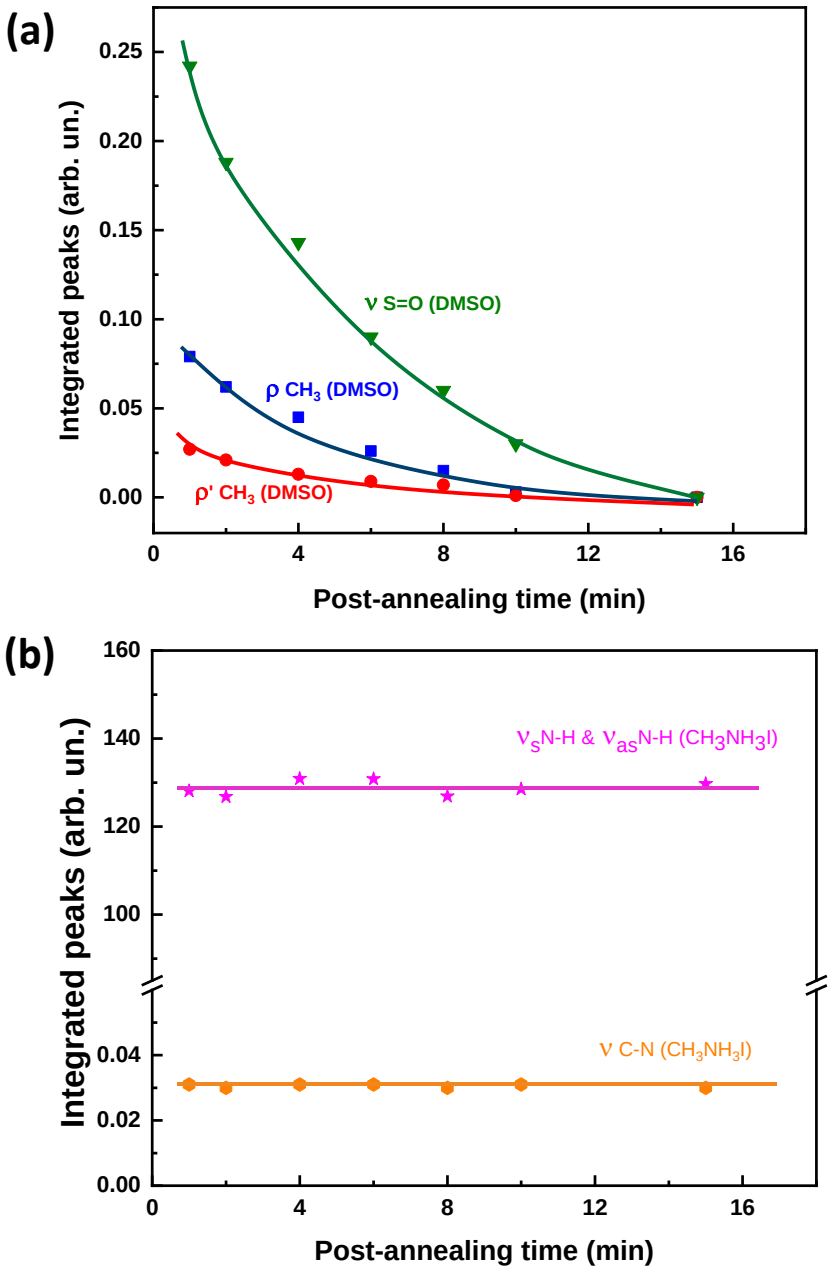

Figure 5.12 Integral peak amplitudes of νS=O (triangles), ρCH_3 (squares) and ρ' CH_3 (circles) in DMSO (a), ν_sN-H & ν_{as}N-H (stars) and ρCH_3 (hexagons) in $MAPbI_3$ (b) depend on different annealing time.

In figure 5.13, this peak was integrated for the different annealing temperatures and annealing time. For all annealing temperatures, there was a time range in which the dependence of the integrated peak could be very well fitted with an exponential decay. Therefore, in this time range the diffusion model in a homogeneous layer works very well. The integrated peak measured for the as-prepared sample was much higher than expected from the diffusion model. Therefore, a layer of DMSO molecules was still adsorbed at the sample surface and disappeared within the first min of annealing. This time range could not be well controlled within the given experiments (un-controlled range). At longer times and higher annealing temperatures, the integrated peaks decreased with increasing time faster than expected from the diffusion model. The reason for this is the ongoing crystallization leading to a rougher surface.

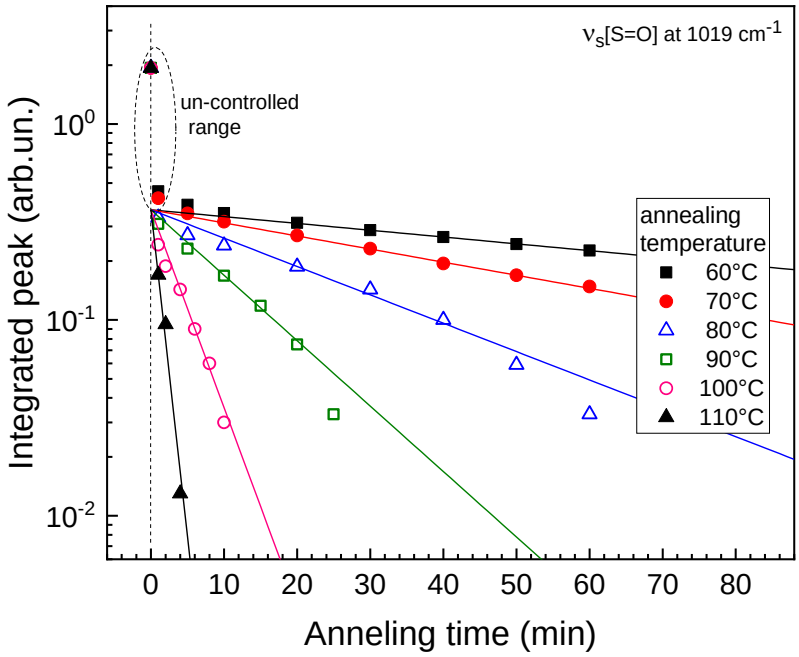

Figure 5.13 Dependence of the integrated IRSE peak of the ν_s[S=O] vibration mode on the annealing time for the annealing temperatures of 60, 70, 80, 90, 100 and 110 ℃ (filled squares, filled circles, open triangles, open squares, open circles and filled triangles, respectively).

The time constants of the decay of the integrated ν_s [S=O] peaks amounted to 125, 65, 30, 13, 4.3 and 1.3 min for the annealing temperatures of 60, 70, 80, 90, 100 and 110 ℃, respectively. These time constants correspond, with respect to a layer

thickness of 400 nm, to values of d^2/τ of $2.1 \cdot 10^{-13}$, $4.1 \cdot 10^{-13}$, $8.9 \cdot 10^{-13}$, $2.05 \cdot 10^{-12}$, $6.2 \cdot 10^{-12}$ and $2.05 \cdot 10^{-11}$ cm²/s, respectively.

The Arrhenius plot of the values of d^2/τ is given in figure 5.14. The activation energy of d^2/τ was not constant. At the lower and higher temperatures, the activation energies could be approximated by 0.64 and 1.48 eV, respectively. The temperature dependence of d^2/τ could be fitted with a diffusion coefficient having two activation energies (E_{A1} and E_{A2}), i.e. the out-diffusion of DMSO was limited by two different processes. The pre-factors of the diffusion coefficients of the two processes are denoted by D_{01} and D_{02}.

$$D_{DMSO} = D_{01} \cdot exp\left(-\frac{E_{A1}}{k_B \cdot T}\right) + D_{02} \cdot exp\left(-\frac{E_{A2}}{k_B \cdot T}\right) \qquad (5.8)$$

The values of E_{A1}, E_{A2}, D_{01} and D_{02} are 0.6 eV, 1.8 eV, $5 \cdot 10^{-12}$ cm²/s and $1.8 \cdot 10^{-14}$ cm²/s, respectively.

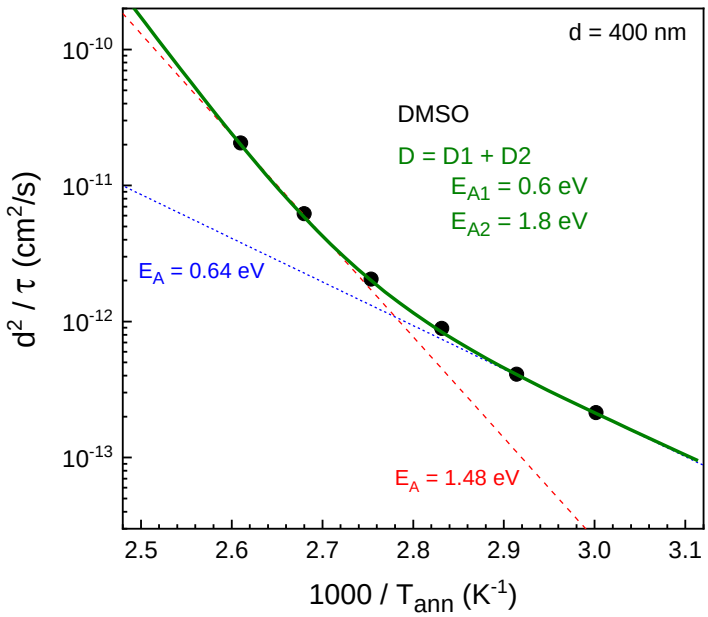

Figure 5.14 Arrhenius plot of d^2/τ (circles), plots for activation energies of 0.64 and 1.48 eV (blue and red short dashed lines, respectively) and fitted with two diffusion coefficients with activation energies of 0.6 and 1.8 eV (green line)

Diffusion processes are limited by transport barriers. Two different activation energies

for the diffusion of DMSO in $MAPbI_3$ give evidence for two different kinds of barriers. We believe that the lower barrier is related to relatively weak bonding of DMSO in complexes which may include, for example, DMSO and components of the precursor salts such as Pb^{2+}. The higher barrier is related to a more stable configuration of DMSO molecules in $MAPbI_3$, for example, at a lattice position of the perovskite.

5.5.2 Analysis of DMF diffusion in $MAPbI_3$ layers

In the previous analysis, we noticed that although DMSO is the main residual solvent, there was still a small amount of DMF residue in the forming $MAPbI_3$ layer. We also made some research on DMF diffusion during annealing.

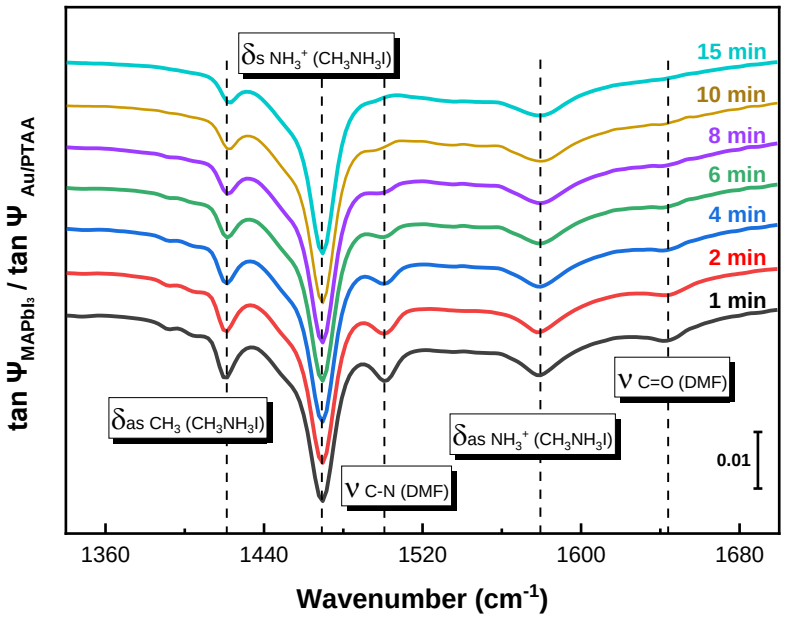

Figure 5.15 IRSE spectra of $MAPbI_3$ layers annealed at 100 ℃ for 1 (black line), 2 (red line), 4 (blue line), 6 (green line), 8 (purple line), 10 (brown line) and 15 (cyan line) min in the spectral range of 1340 – 1700 cm^{-1}, the prominent peaks are labeled

Figure 5.15 shows IRSE spectra of $MAPbI_3$ layers annealed at 100 ℃ for 1, 2, 4, 6, 8 and 15 min in a reduced spectral range between 1340 and 1700 cm^{-1}. In this range, except the peaks from $MAPbI_3$ (CH_3 bending mode at 1420 cm^{-1}, NH_3^+ symmetric

and asymmetric bending modes at 1468 and 1578 cm^{-1}), there were also two peaks assigned to DMF (C-N stretching mode at 1501 cm^{-1} and C=O stretching mode at 1578 cm^{-1}). That means DMF residue was also in the prepared $MAPbI_3$ layer because of the DMF-PbI_2 complex formed. When comparing with the DMSO residue, there was much less DMF residue as the peak intensities were much weaker. The peak amplitudes also decreased with increasing annealing time and were below the resolution of IRSE after annealing for 15 min. For the residue analysis, we quantify the relative amount by integrating the amplitude of peaks at 1578 cm^{-1}.

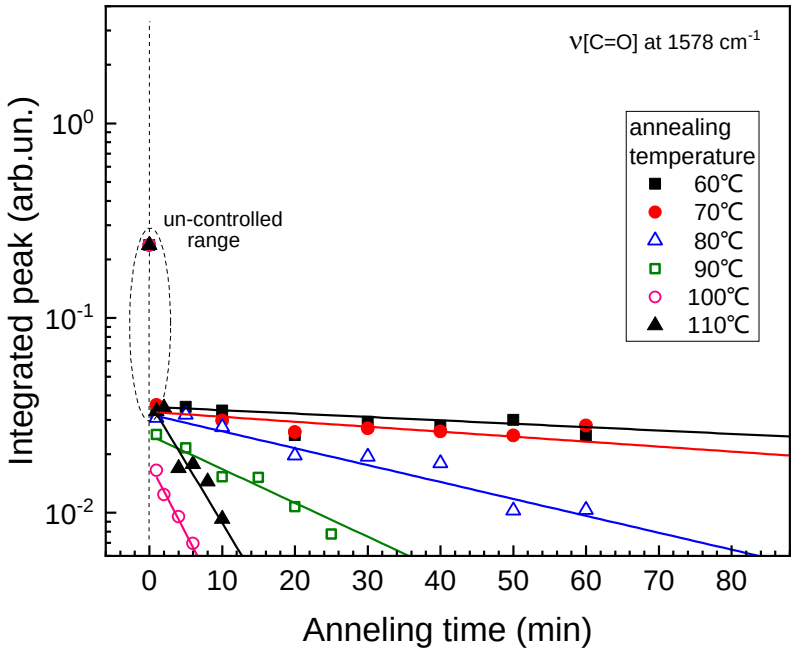

Figure 5.16 Dependence of the integrated IRSE peak of the ν[C=O] vibration mode on the annealing time for the annealing temperatures of 60, 70, 80, 90, 100 and 110 ℃ (filled squares, filled circles, open triangles, open squares, open circles and filled triangles, respectively)

As shown in figure 5.16, this peak was integrated for the different annealing temperatures and annealing times. Unlike the results from integrated peak of DMSO, except annealing temperature at 100 ℃, the dependence of other integrated peaks could not be fitted with an exponential decay very well. Moreover, the difference of integral values of DMF peaks was larger after 1 min annealing with different temperature. The main reason that caused the above results was that DMF is less

stable in the $MAPbI_3$ layer because of the lower boiling point and weaker bond with Pb when compared with DMSO. Less DMF residue also led to weaker absorptions, which made it more difficult to analysis. And the inconsistency of DMF residues in samples caused larger experimental errors.

From figure 5.13, we can work out that the time constants of the decay of the integrated ν [C=O] peaks amounted to 250, 170, 50, 25, 6 and 7 min for the annealing temperatures of 60, 70, 80, 90, 100 and 110 ℃, respectively. Then the values of d^2/τ were $1.07 \cdot 10^{-13}$, $1.57 \cdot 10^{-13}$, $5.33 \cdot 10^{-13}$, $1.07 \cdot 10^{-12}$, $4.44 \cdot 10^{-12}$ and $3.81 \cdot 10^{-12}$ cm^2/s, respectively.

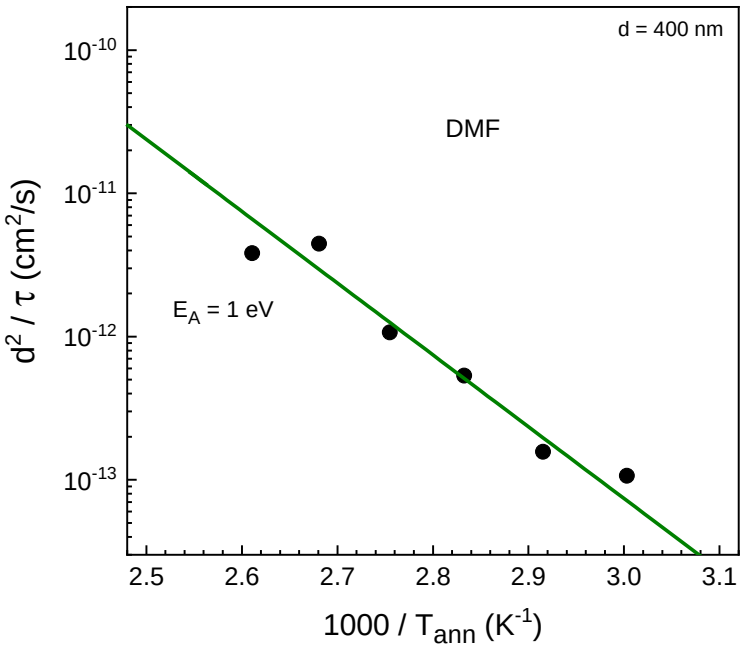

Figure 5.14 Arrhenius plot of d^2/τ, plots are fitted with activation energies of 1 eV

The Arrhenius plots in figure 5.14 were fitted with a linear relationship. The activation energy of 1 eV was calculated. Usually, higher temperature should have smaller time constant of the decay because there's more heat for solvent diffusion. But the τ is larger at 110 ℃ than that at 100 ℃ which led a lower value of d^2/τ. It could be that bad controllability of DMF in samples caused the irregular difference. Comparing with DMSO, more work need be done to build an accurate out-diffusion model for DMF in $MAPbI_3$ layer during the annealing.

5.6 Influence of the content of residual solvents on $MAPbI_3$ layers and solar cells

The influence of residual solvent on the morphology, electronic properties of the formed $MAPbI_3$ layer was investigated. The performance of solar cells based on $MAPbI_3$ layers with different level of residues was also studied.

5.6.1 Influence of the content of residual solvents on the morphology of $MAPbI_3$ layers

The SEM images of the $MAPbI_3$ layers treated with different post annealing time at 100 ℃ are shown in Figure 5.15.

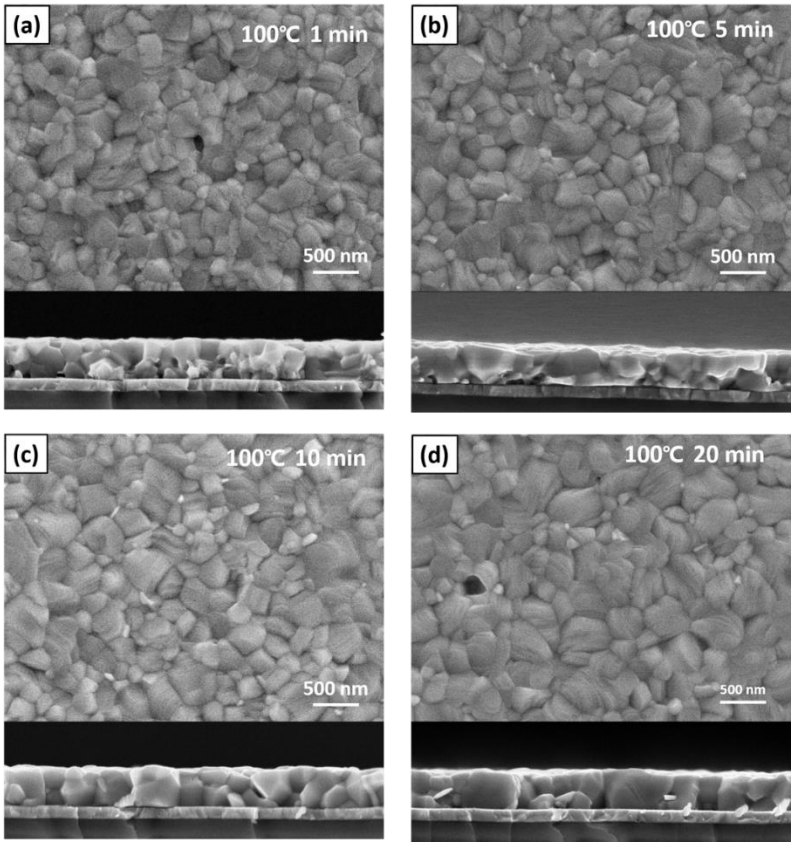

Figure 5.15 Surface, cross section view morphologies of the $MAPbI_3$ layers post annealed at 100 ℃ with the time of 1 min (a), 5 min (b), 10 min (c) and 20 min (d).

The increasing post annealing time means there were less residual solvents in the $MAPbI_3$ layers. From both top-view and cross-section SEM images, we can observe that, more and more larger crystals formed when fewer residual solvent left.

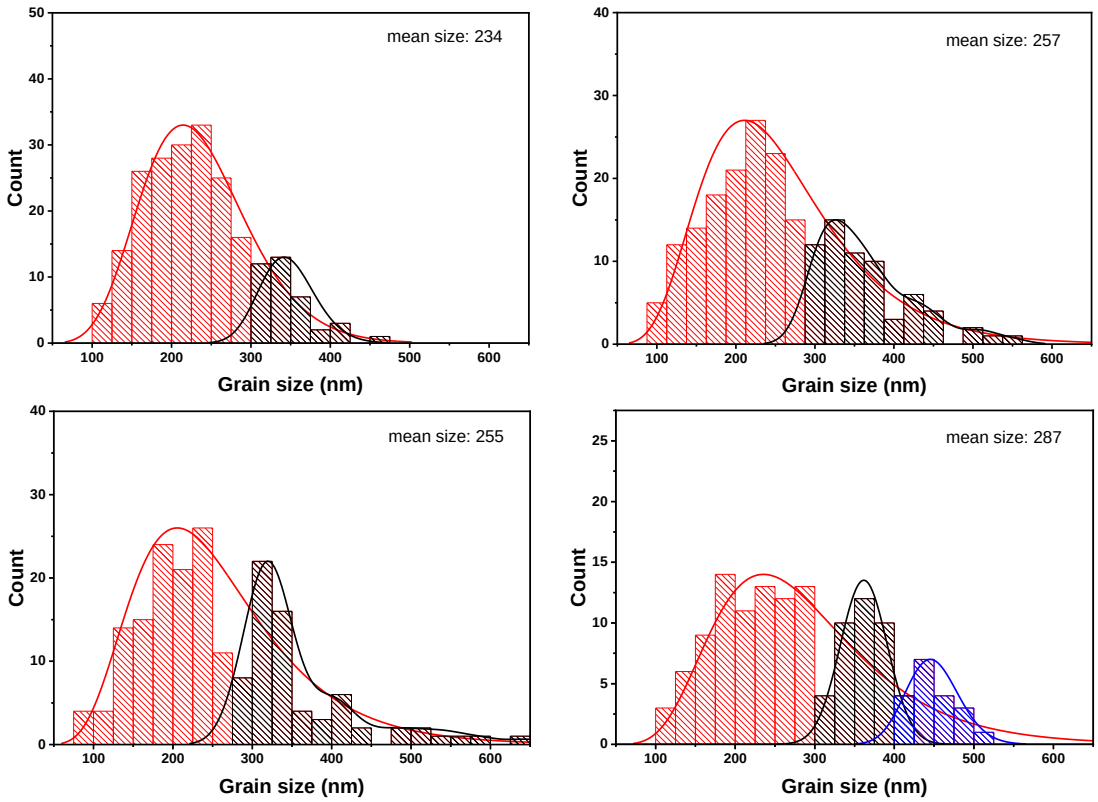

Figure 5.16. Grain size distribution of $MAPbI_3$ layers post annealed at 100 ℃ with the time of 1 min (a), 5 min (b), 10 min (c) and 20 min (d).

From the analysis of grain size distribution of $MAPbI_3$ layers annealed at 100 ℃ with different time (Figure 5.16), it was shown that the mean size increased from 234 nm to 287 nm with longer time of post annealing. And the amount of crystals over 300 nm increased. This demonstrated that reducing the residual solvent in the formed $MAPbI_3$ layers was beneficial to the further growth of $MAPbI_3$ crystals.

5.6.2 Influence of the content of residual solvents on the band gap and exponential tails in $MAPbI_3$

The band gaps and exponential tails of $MAPbI_3$ layers prepared by vacuum-assisted

treatment annealed at 100 ℃ with different post annealing time were investigated. Figure 5.17 shows in-phase and phase-shifted by 90 ° overview surface photovoltage spectra of $MAPbI_3$ layers post annealed at 100 ℃ with the time of 1, 2, 4, 6, 8, 10 and 20 min. From 1 min to 6 min, the amplitude of in-phase signals increased with the increasing post annealing time. Then the signals started to decrease with longer annealing time. This might be due to less traps generated at external surface after 8 min or longer post annealing.

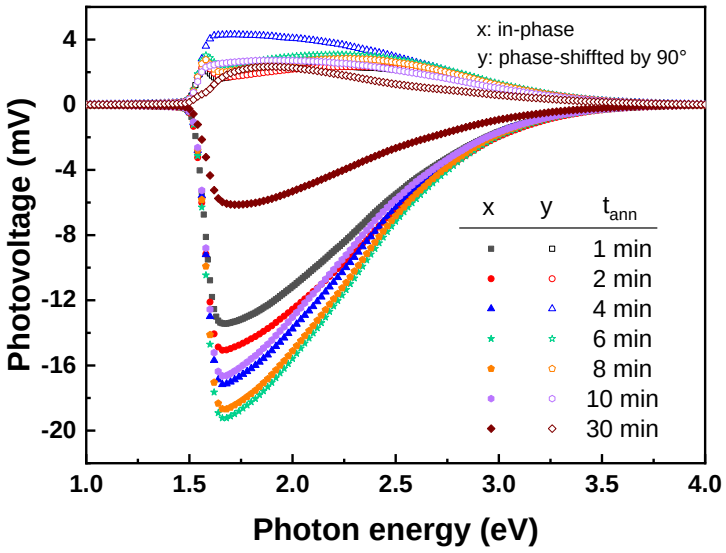

Figure 5.17 In-phase and phase-shifted by 90 ° overview surface photovoltage spectra of $MAPbI_3$ layers annealed at 100 ℃ with post annealing time of 1, 2, 4, 6, 8, 10 and 20 min (squares, circles, triangles, stars, pentagons, hexagons and rhombus respectively).

In Figure 5.18, for the samples post annealing with the time of 1, 2, 4, 6, 8, 10 and 20 min, the values of Eg were 1.554, 1.554, 1.558, 1.56, 1.561, 1.561 and 1.56 eV, respectively. The band gaps increased a little bit in the first 6 min, then tended to be stable around 1.56 eV. The exponential tails of the $MAPbI_3$ layers post annealed at 100 ℃ with different time were shown in Figure 5.19. The corresponding values of E_t were amounted to 21.5, 22.5, 21, 22, 21.5 22.5 and 25 meV for the time of 1, 2, 4, 6, 8, 10 and 20 min, respectively. It can be seen that the exponential tails fluctuated within a narrow range of 21 to 22.5 meV. After 20 min post annealing, the values of E_t

increased to 25 meV. This means the disorder of $MAPbI_3$ layer also slightly increased.

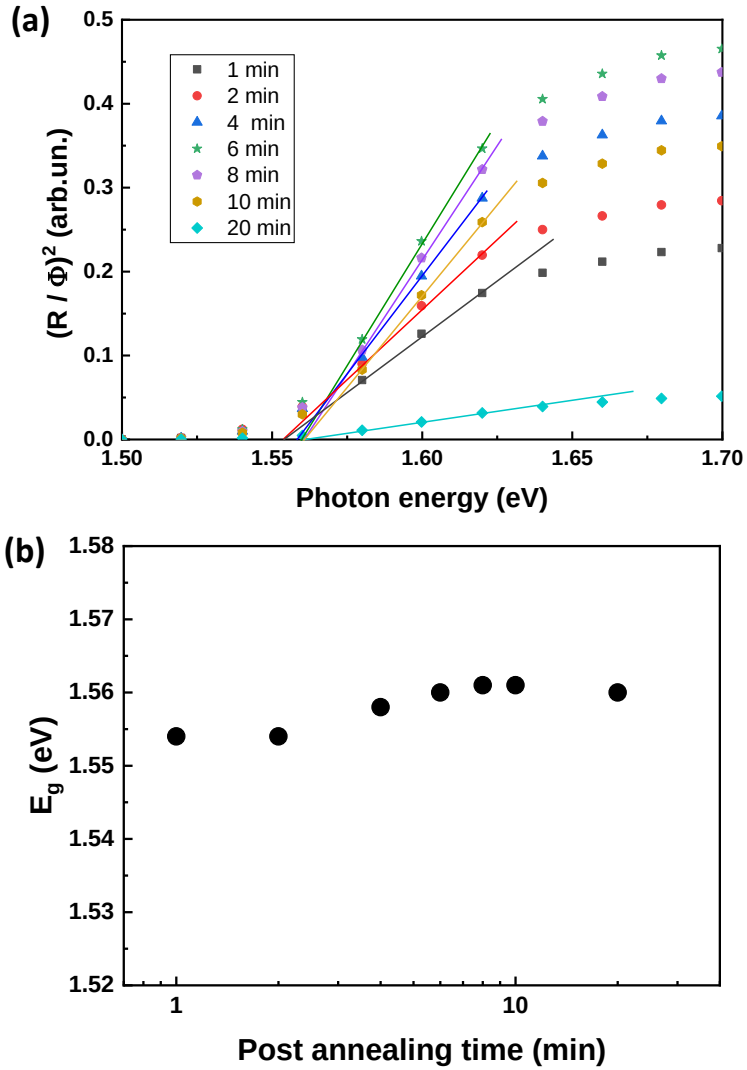

Figure 5.18 Tauc plots of the SPV amplitude spectra of $MAPbI_3$ layers prepared with the post annealing time of 1, 2, 4, 6, 8, 10 and 20 min (squares, circles, triangles, stars, pentagons, hexagons and rhombus respectively) (a) and band gaps as a function of the post annealing time (b).

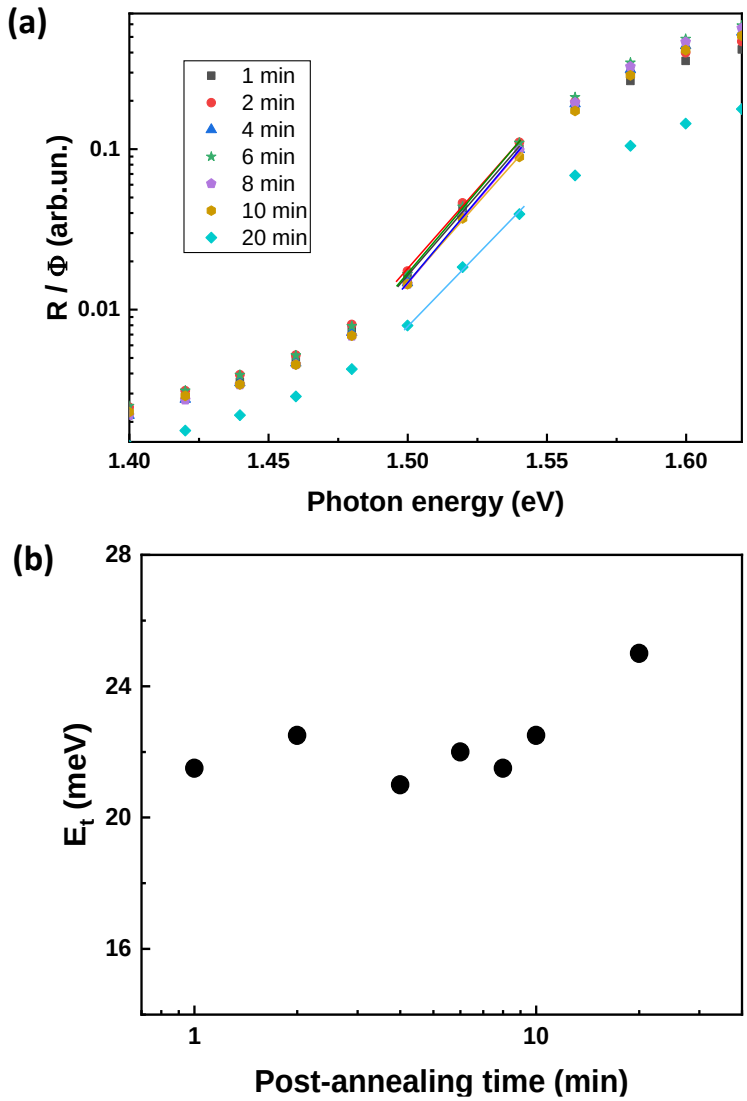

Figure 5.19 Spectra of the quotient of SPV amplitude and the photon flux on a logarithmic scale near the band gap of $MAPbI_3$ layers prepared with the post annealing time of 1, 2, 4, 6, 8, 10 and 20 min (squares, circles, triangles, stars, pentagons, hexagons and rhombus respectively) (a) and exponential tails as a function of the post annealing time (b).

5.6.3 Performance of solar cells based on $MAPbI_3$ layers prepared with different post annealing time

Figure 5.20 shows the measured short-circuit current density (J_{SC}), open-circuit voltage (V_{OC}), fill factor (FF) and power conversion efficiency (PCE) of the solar cells based on the $MAPbI_3$ prepared by vacuum-assisted treatment with the post

annealing time of 1 min, 5 min, 10 min and 20 min, respectively. There were about 12 solar cells measured for each kind. As shown in Figure 5.20 (a), the highest average PCE was obtained from the solar cells based on the $MAPbI_3$ post annealed with 20 min.

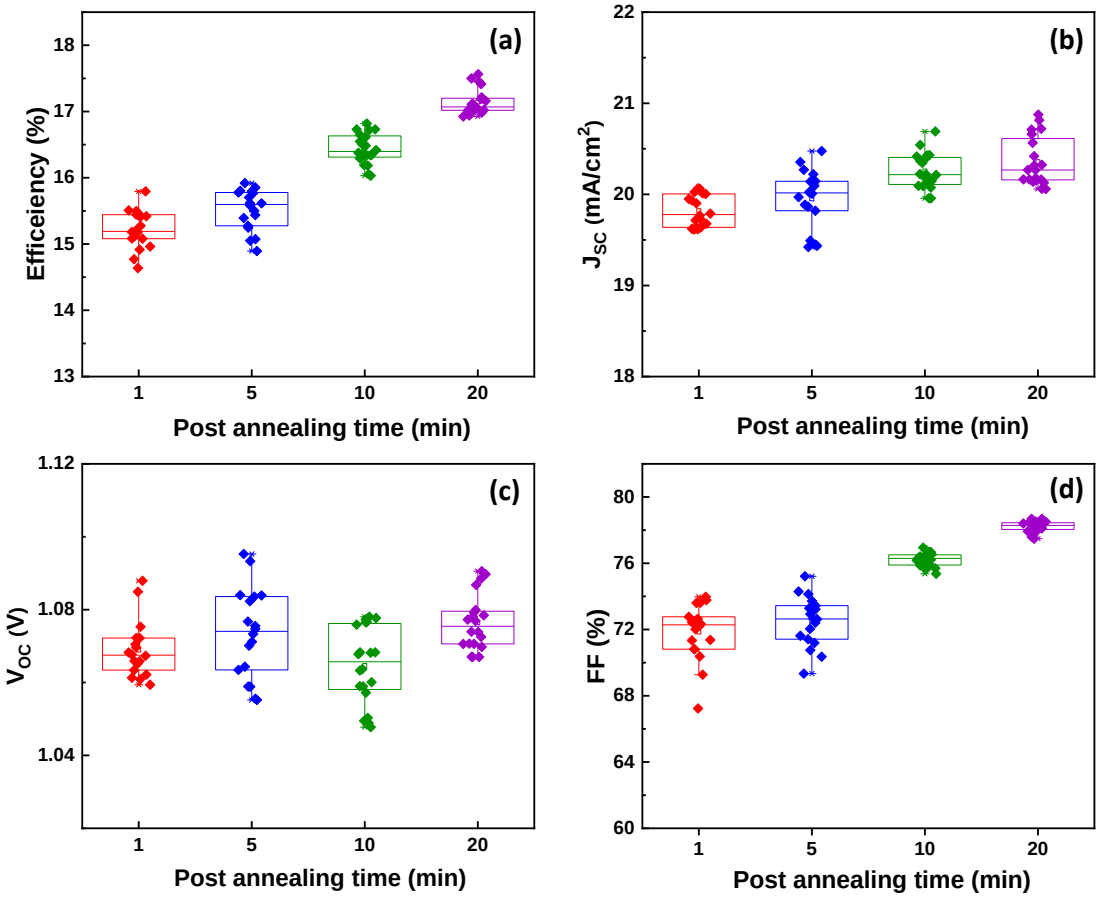

Figure 5.20 (a) power conversion efficiency (PCE), (b) short-circuit current density (J_{SC}), (c) open-circuit voltage (V_{OC}) and (d) fill factor (FF) of the solar cells based on the $MAPbI_3$ post annealed with the time of 1min, 5 min, 10 min and 20 min, respectively.

The increasing post annealing time also means the content of the residual solvent in the perovskite layers was decreasing. With the decrease of residual solvent, the J_{SC} of solar cells gradually increased to more than 20 mA/cm^2. But the V_{OC} of solar cells had a little change. The values fluctuated in a range of 1.04-1.1 V. It should be noted that the V_{OC} is often limited by the contact layers and not by the absorber quality when E_g doesn't change. The biggest change is from the FF of solar cells. The average values had not only noticeable increase, but also less dispersion. This is the main reason that

caused an improvement of solar cells performance.

5.6.4 Performance of solar cells based on $MAPbI_3$ layers prepared at different post annealing temperature

By using the DMSO diffusion model, similar amounts of residual DMSO can be adjusted for different post annealing temperatures by the annealing time. Therefore, the influence of the out-diffusion rate of DMSO on the performance of solar cells based on the $MAPbI_3$ can be studied. The sample were post annealed at 60 ℃, 80 ℃, 100 ℃ and 120 ℃ for the time of 5 min, 10 min, 60 min and 150 min, respectively. From the model, the calculated diffusion coefficients were $3.41x10^{-13}$, $1.33x10^{-12}$, $9.92x10^{-12}$ and $7.20x10^{-11}$ cm^2/s for annealing at 60 ℃, 80 ℃, 100 ℃ and 120 ℃, respectively. With respect to the diffusion model, the amounts of residual DMSO can be estimated with a S/Pb ratio and are equal to $4.5x10^{-3}$, $2.7x10^{-3}$ and $2.3x10^{-3}$ for annealing at 60 ℃, 80 ℃ and 100 ℃. However, the amounts of residual DMSO is much lower for annealing at 120 ℃, and the S/Pb ratio is equal to $1x10^{-6}$.

Figure 5.21 shows the measured short-circuit current density (J_{SC}), open-circuit voltage (V_{OC}), fill factor (FF) and power conversion efficiency (PCE) of the solar cells based on the $MAPbI_3$ prepared by vacuum-assisted treatment at the post annealing temperature of 60 ℃, 80 ℃, 100 ℃ and 120 ℃, respectively. As shown in Figure 5.21 (a), the highest PCE of 20.19% was obtained from the solar cells based on the $MAPbI_3$ post annealed at 120 ℃ with the time of 5 min. The average PCE was 19.80%. For comparison, the average PCE of 60 ℃, 80 ℃ and 100 ℃ were 15.47%, 17.29% and 18.36%, respectively. The solar cells based on the $MAPbI_3$ post annealed at 120 ℃ also had the highest J_{SC} and V_{OC}.

The average values of J_{SC} were 20.9, 21.9, 22.3 and 23.7 mA/cm^2 for annealing at 60 ℃, 80 ℃, 100 ℃ and 120 ℃, respectively. There was a significant increase of J_{SC} when the post annealing temperature was increased which means the out-diffusion

rate was increased. And the deviation also decreased with the increasing temperature. This could be because a higher out-diffusion rate of DMSO led to the formation of larger crystals with high quality [144-145].

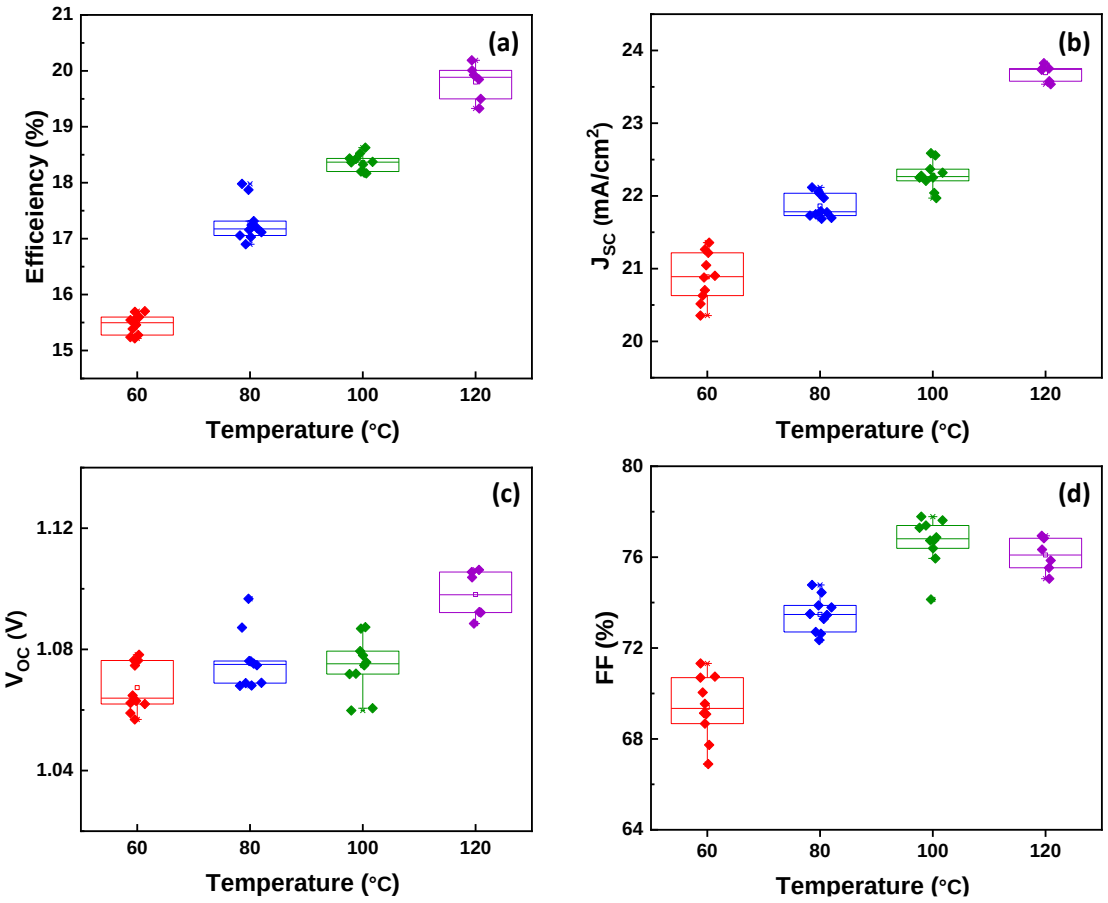

Figure 5.21 (a) power conversion efficiency (PCE), (b) short-circuit current density (J_{sc}), (c) open-circuit voltage (V_{oc}) and (d) fill factor (FF) of the solar cells based on the $MAPbI_3$ post annealed at the temperature of 60 ℃, 80 ℃, 100 ℃ and 120 ℃ with the time of 5min, 10 min, 60 min and 150 min, respectively.

The change of average V_{OC} for annealing at 60 ℃, 80 ℃ and 100 ℃ was small (1.07, 1.08, and 1.08 V, respectively). Therefore, the variation of the diffusion rate did not significantly influence V_{OC}, i.e. recombination losses in the bulk and at the interfaces did not change significantly. In contrast, V_{OC} increased to about 1.1 V for annealing at 120 ℃ for 5 min. Therefore, it seems that the amount of residual DMSO can influence V_{OC} for high diffusion rates. However, much more detailed experiments will be needed in order to clarify the complex influence of crystallization, complex formation

and out-diffusion of solvent molecules on the behavior of solar cells based on $MAPbI_3$ layers.

The values of the average FF were 69.4%, 73.5%, 76.7% and 76.1% for annealing at 60 ℃, 80 ℃, 100 ℃ and 120 ℃, respectively. Therefore, the FF increased with the increasing out-diffusion rate of DMSO and tended to saturate at a high out-diffusion rate and a very low amount of residual DMSO.

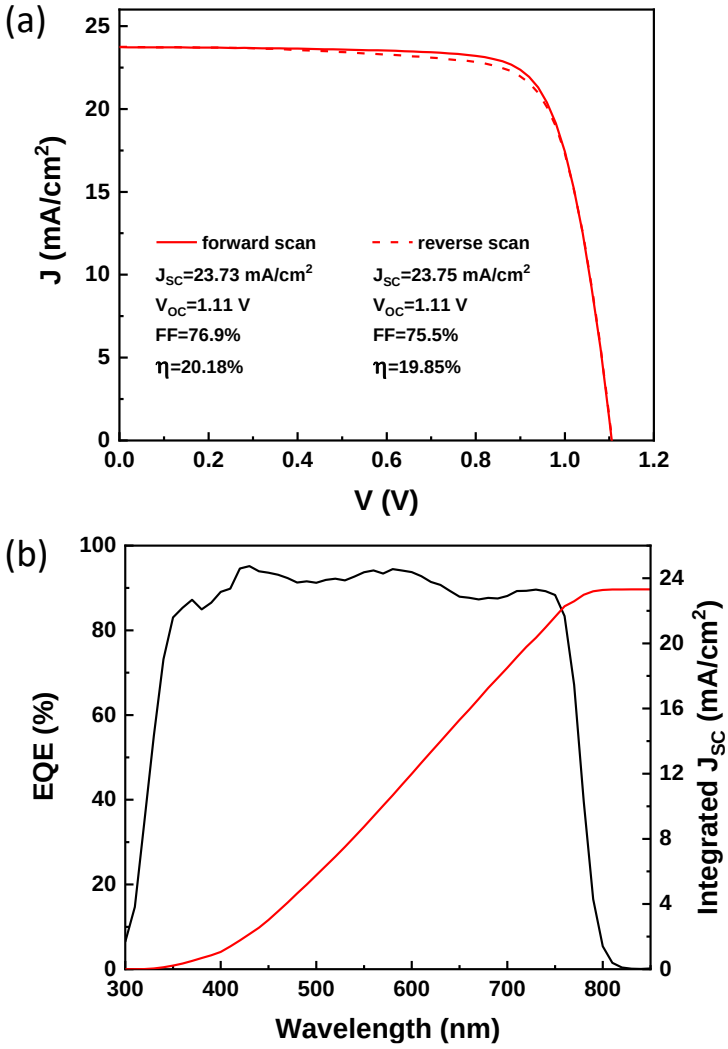

Figure 5.22 Forward (solid line) and reverse (dash line) scans of the J-V characteristic of the solar cells with the highest efficiency under illumination at AM1.5 (a) and spectra of the external quantum efficiency (black line) and of the integrated short circuit current density (red line) (b).

Figure 5.22 (a) shows the forward and reverse scans of the J-V characteristics of the solar cell with the highest efficiency (T_{ann} = 120 °C, t_{ann} = 5 min) under illumination at AM1.5. The values of the J_{SC}, V_{OC}, FF and PCE were 23.73 mA/cm², 1.11 V, 76.9% and 20.2%, respectively. The spectra of the external quantum efficiency (EQE) and of the corresponding integrated J_{SC} are given in Figure 5.22 (b). The value of J_{SC} following from the EQE measurement was 23.3 mA/cm².

5.7. Conclusions

Methodologies for the measurement of the content of DMSO and of diffusion coefficients of DMSO in $MAPbI_3$ layers have been developed by applying HR-CSAS and IRSE in combination with a diffusion model in a homogeneous layer. The amount of DMSO was calibrated with HR-CSAS in terms of the S/Pb molar ratio for measurements by IRSE. It was shown that diffusion coefficients of DMSO in $MAPbI_3$ can be obtained from the dependencies of integrated peaks of specific vibration modes such as the S=O stretching mode on annealing time and annealing temperature.

It was found that the diffusion coefficient of DMSO in $MAPbI_3$ is a superposition of two thermally activated processes with E_{A1}, D_{01}, E_{A2} and D_{02} are 0.6 eV, 10^{-11} cm²/s, 1.8 eV and $3.6 \cdot 10^{-4}$ cm²/s, respectively. Different coordination and/or binding states of DMSO molecules are the origin for the rather different diffusion processes. It is obvious that the lower activation energy corresponds to activation of loosely bond molecules whereas the higher activation energy belongs to activation of DMSO trapped in the lattice of $MAPbI_3$. Furthermore, it was also found that out-diffusion of DMSO can have a strong influence on the fill factor of solar cells and its standard deviation. Incidentally, an additional influence by DMF molecules cannot be ruled out.

A preliminary research about the influence of out-diffusion rate on the solar cells performance was done. It has been demonstrated that efficiencies above 20% can be

reached at a high out-diffusion rate and very low content of DMSO. Therefore, it seems that a high out-diffusion rate of the solvent is very useful for further improving the quality of perovskite films. However, more complex studies about the change of morphology and electronic properties of perovskite films prepared with different out-diffusion rates have to be performed in order to get deeper knowledge about mechanisms behind and their relation to the performance of solar cells.

6. Summary and outlook

In this thesis, $MAPbI_3$ perovskite films were prepared by a one-step solution based process. Vacuum-assisted evaporation of solvent (vacuum-assisted treatment) was used for fast removing of solvents in the precursor solutions after spin coating. Furthermore, perovskite layers were conditioned in a post-annealing process. In contrast to the commonly used anti-solvent dripping process, the vacuum-assisted treatment allows for realization of practically ideal boundary conditions for studying out-diffusion of solvents, first, and for upscaling of perovskite layer deposition, second. In previous reports, the effect of changing the pressure during vacuum-assisted treatment has been studied. In this thesis, another three major factors were investigated. The three major factors of vacuum-assisted treatment are related to solvent composition, the substrate temperature and the treatment time whereas the two major factors of post-annealing are related to annealing temperature and annealing time. The influence of the major factors of vacuum-assisted treatment and post-annealing on morphology, electronic properties and performance of solar cells was studied. The morphologies were measured by SEM, distributions of grain size and the mean size for different $MAPbI_3$ films were obtained based on the SEM images. The studied electronic properties included the band gaps (E_g) and exponential tails (E_t) and were measured by modulated SPV spectroscopy. The variation of the major factors of the vacuum-assisted treatment was mainly aimed to the optimization of conditions for reaching high efficiencies. The post-annealing experiments aimed to the study of the role of out-diffusion of solvent molecules. For this purpose, a methodology was developed by using HR-CSAS and IRSE for quantitative analysis of the DMSO content in perovskite layers. In addition, the performance of solar cells based on the $MAPbI_3$ prepared under different post-annealing conditions was studied.

In the optimization, one factor was varied in a certain range when the other two were fixed. First, at fixed temperature (30 ℃) and vacuum-assisted treatment time (60 s), the DMF/DMSO varied from 12:1 to 4:1. With the increasing DMSO proportion,

larger crystals and more pinholes were formed. However, the further increase of DMSO proportion led to the formation of small crystals and large clusters. Both E_g and E_t showed a trend of decrease with increasing DMSO proportion. The solar cells based on the $MAPbI_3$ layers prepared with a DMF/DMSO ratio of 9:1 showed the highest efficiency. Second, at fixed solvent composition (DMF:DMSO=9:1) and treatment time (60 s), the substrate temperature was varied from 20 ℃ to 60 ℃. As a result, more small crystals and pinholes were formed with increasing temperature. Both E_g and E_t showed a trend of decrease with increasing temperature. The solar cells based on the $MAPbI_3$ layers prepared at a temperature of 20 ℃ showed the highest efficiency. At last, at the fixed solvent composition (DMF:DMSO=9:1) and substrate temperature (30 ℃), the vacuum-assisted treatment time was varied from 10 s to 600 s. With increasing treatment time, more small crystals and pinholes were formed. The change of the treatment time had little effect on E_g and E_t. The solar cells with best performance was obtained based on the $MAPbI_3$ layers prepared with a treatment time of 10 s. Above all, at the given pressure of 60 Pa, solar cells with best performance based on the $MAPbI_3$ layer were obtained with the optimized factors (DMF:DMSO = 9:1, 30 ℃, 10 s). The highest efficiency was 17.8%. In general, higher DMSO proportion, higher temperature and longer vacuum-assisted treatment time resulted in a reduction of the efficiency.

At first glance, results can be discussed based on the nucleation/growth LaMer model. The solvent evaporation rate decreased with increasing DMSO proportion. Following the LaMer model, it can be supposed that the nucleation time became shorter and the time of growth became longer with increasing solvent evaporation rate whereas the change of solubility with changing DMSO proportion can be ignored. The evaporation rate and the solubility increased with increasing substrate temperature. With respect to the experimental results, it can be concluded that the nucleation time increased with increasing temperature.

For studying the out-diffusion of DMSO during post annealing, the change of residual DMSO in the formed $MAPbI_3$ layer was determined by two methods. The HR-CSAS was used as the DMSO was the only S-containing ingredient, and the IRSE was used because there was a finger print peak of DMSO (S=O stretching mode) which was analyzed in the IRSE spectrum. The amount of DMSO was calibrated with HR-CSAS in terms of the S/Pb molar ratio which correlated linearly with the integrated values of S=O peaks from the measured IRSE spectra. Therefore, the integrated peaks of the S=O stretching mode could be directly used for diffusion analysis. The annealing time and the annealing temperature were varied. A simple model was developed for diffusion analysis correlating the ratio of the squared layer thickness and the exponential decay time directly with the diffusion coefficient. It was found that the diffusion coefficient of DMSO in $MAPbI_3$ is a superposition of two thermally activated processes with E_{A1}, D_{01}, E_{A2} and D_{02} are 0.6 eV, 10^{-11} cm^2/s, 1.8 eV and $3.6x10^{-4}$ cm^2/s, respectively. Different coordination and/or binding states of DMSO molecules are the origin for the rather different diffusion processes. It is obvious that the lower activation energy corresponds to activation of loosely bond of complex whereas the higher activation energy belongs to activation of DMSO trapped in the lattice of $MAPbI_3$. Incidentally, the out-diffusion of DMF could also be investigated by analyzing C=O (IRSE), however, the experimental error was much larger than for DMSO out-diffusion.

Furthermore, it was found that out-diffusion of DMSO can have a strong influence on the performance of solar cells and the standard deviations of parameters. Incidentally, an additional influence by DMF molecules cannot be ruled out. It was shown that efficiencies above 20% can be realized with vacuum-assisted treatment for solar cells based on $MAPbI_3$.

For getting a deeper understanding of the complex mechanisms of solvent evaporation and out-diffusion and crystallization from intermediates and perovskite seeds, more extended investigations are needed in combination with more sophisticated models.

For the analysis of limiting mechanisms of out-diffusion of residual solvents, it will be interesting to vary different kinds of solvents and perovskites. In future, knowledge about vacuum-assisted treatment and out-diffusion of solvent molecules can be transferred to other HOIP systems such as multi-cation perovksites. Although there is a limitation for applying HR-CSAS to specific atoms, IRSE can be used for any solvent molecules showing characteristic finger print peaks. Finally, the vacuum-assisted treatment is a promising method for producing perovskite films in large areas, for example, in combination with printing technologies.

List of Symbols and abbreviations

Abbreviation	Description
Ag	silver
A.M 1.5 G	air mass of 1.5 global
Au	gold
BCP	bathocuproine
CIGS	copper indium gallium selenide
CdTe	cadmium telluride
CPD	contact potential difference
CS	carbon monosulfide
C_s	saturation concentration
C_{max}	maximum concentration of nucleation
C_{min}	minimum concentration of nucleation
Cu	copper
CZTS	copper tin zinc sulphide
C_{60}	fullerene
c-Si	crystalline silicon
cm^2	squared centimeter
D	charge carrier diffusion coefficient
DFT	density functional theory
DMF	N,N-dimethylformamide
DMSO	dimethyl sulfoxide
D_N	donor number
DSSCs	dye-sensitized solar cells
d	layer thickness
d_s	distance between the centers of positive and negative charge carriers
E_A	activation energy
E_F	Fermi-energy

E_{Fn}	Fermi-energy of electrons
E_{Fp}	Fermi-energy of holes, EFp
$E_{F,ce}$	Fermi-energy of electrons in contact material
$E_{F,ch}$	Fermi-energy of holes in contact material
E_g	band gap
E_t	exponential tails
EQE	external quantum efficiency
eV	electron volt
$FAPbI_3$	formamidinium lead iodide
FF	fill factor
GaAs	gallium arsenide
GBL	γ-butyrolactone
HR-CSAS	high resolution continuous source absorption spectrometry
h	hour
hv	photon energy
I_D	a current across a diode
IRSE	infrared spectroscopic ellipsometry
ITO	Indium tin oxide
I_{SC}	short circuit current
J	joule
J_{mp}	corresponding photocurrent density
J_{SC}	short circuit current density
J_{SC}^{max}	ideal short circuit current density
J_0	diode saturation current density
k_B	Boltzmann constant
L	diffusion length
$MAPbI_3$	methylammonium lead iodide
$MAPbBr_3$	methylammonium lead bromide
$MASnI_3$	methylammonium tin iodide

meV	milli-electron volt
mg	milligram
min	minute
mL	milliliter
mpp	maximum power point
mV	millivolt
N_e	the number of collected photo-generated electrons
N_{ph}	the number of incident photons
NiOx	nickel oxide
P	pressure
Pa	Pascal
Pb	lead
PCE	power conversion efficiency
PEDOT	poly(3,4-ethylenedioxythiophene)
P_{in}	incident power from the sunlight
PTAA	poly[bis(4-phenyl)(2,4,6-trimethylphenyl)amine]
Q	amount of separated charge carriers in space
QE	quantum efficiency
q	electronic charge
R_L	load resistance
R_m	measurement resistance
R_S	series resistance
R_{SH}	shunt resistance
SEM	scanning electron microscopy
SPV	surface photovoltage
SnO_2	stannic oxide
spiro-OMeTAD	2,2',7,7'-Tetrakis[N,N-di(4-methoxyphenyl)amino]-9,9'-spirobiflu orene
T	absolute temperature

TCO	transparent conducting oxide
TiO_2	titanium dioxide
T_{ann}	post annealing temperature
T_{vac}	substrate temperature during vacuum-assisted treatment
t_{ann}	time of post annealing
t_{vac}	time of vacuum assisted treatment
V	volume
V_{mp}	corresponding photovoltage
V_{OC}	open circuit voltage
V_s	light induced voltage between the electrodes
W_s	work functions of the sample electrode
W_{ref}	work functions of reference electrode
X	in-phase signal
Y	phase shifted by 90 °signal
ZnO	zinc oxide
ε	permittivity
ε_0	vacuum permittivity
μ	charge carrier mobility
τ	1. charge carrier lifetime, 2. decay time constant
Φ_{ph}	photon flux
℃	degrees centigrade

References

[1] Green, M. A. Third generation photovoltaics: Ultra-high conversion efficiency at low cost. Progress in Photovoltaics: Research and Applications, 2001, 9(2), 123–135.

[2] Kojima, A., Teshima, K., Shirai, Y., Miyasaka, T. Organometal Halide Perovskites as Visible-Light Sensitizers for Photovoltaic Cells. Journal of the American Chemical Society, 2009, 131(17), 6050–6051.

[3] NREL Efficiency Chart. This Plot Is Courtesy of the National Renewable Energy Laboratory, Golden, CO. Available online: https://www.nrel.gov/pv/cell-efficiency.html.

[4] He, Y., & Galli, G. Perovskites for Solar Thermoelectric Applications: A First Principle Study of $CH_3NH_3AI_3$ (A = Pb and Sn). Chemistry of Materials, 26(18), 2014, 5394–5400.

[5] You, Y.-M., Liao, W.-Q., Zhao, D., Ye, H.-Y., Zhang, Y., Zhou, Q., Niu, X., Wang, J., Li, P.-F., Fu, D.-W., Wang, Z., Gao, S., Yang, K., Liu, J.-M., Li, J., Yan, Y., Xiong, R.-G. An organic-inorganic perovskite ferroelectric with large piezoelectric response. Science, 2017, 357(6348), 306–309.

[6] Yin, W.-J., Shi, T., Yan, Y. Unique Properties of Halide Perovskites as Possible Origins of the Superior Solar Cell Performance. Advanced Materials, 2014, 26(27), 4653–4658.

[7] Gao, L.-L., Liang, L.-S., Song, X.-X., Ding, B., Yang, G.-J., Fan, B., Li, C.-X., Li, C.-J. Preparation of flexible perovskite solar cells by a gas pump drying method on a plastic substrate. Journal of Materials Chemistry A, 2016, 4(10), 3704–3710.

[8] Chen, W., Wu, Y., Yue, Y., Liu, J., Zhang, W., Yang, X., Chen, H., Bi, E., Ashraful, I., Grätzel, M., Han, L. Efficient and stable large-area perovskite solar cells with inorganic charge extraction layers. Science, 2015, 350(6263), 944–948.

[9] Jeon, N. J., Noh, J. H., Kim, Y. C., Yang, W. S., Ryu, S., Seok, S. I. Solvent engineering for high-performance inorganic–organic hybrid perovskite solar cells. Nature Materials, 2014, 13(9), 897–903.

[10] Lee, J.-W., Kim, H.-S., Park, N.-G. Lewis Acid–Base Adduct Approach for High Efficiency Perovskite Solar Cells. Accounts of Chemical Research, 2016, 49(2), 311–319.

[11] Bhalla, A. S., Guo, R., Roy, R. The perovskite structure—a review of its role in ceramic science and technology. Materials Research Innovations, 2000, 4(1), 3–26.

[12] Johnsson, M., Lemmens, P. Crystallography and Chemistry of Perovskites. Handbook of Magnetism and Advanced Magnetic Materials. 2007.

[13] Jahn, H. A., Teller, E. Stability of Polyatomic Molecules in Degenerate Electronic States. I. Orbital Degeneracy. Proceedings of the Royal Society A: Mathematical, Physical and Engineering Sciences, 1937, 161(905), 220–235.

[14] Goldschmidt, V. M. Die Gesetze der Krystallochemie. Die Naturwissenschaften, 1926, 14(21), 477–485.

[15] Wells, A. F. Structural Inorganic Chemsitry, Oxford University Press, 1995.

[16] Müller, U. Inorganic Structural Chemistry, Wiley & Sons Ltd, 1993.

[17] Li, C., Lu, X., Ding, W., Feng, L., Gao, Y., Guo, Z. Formability of ABX_3 (X= F, Cl, Br, I) halide perovskites. Acta Crystallographica Section B Structural Science, 2008, 64(6), 702–707.

[18] Li, W., Wang, Z., Deschler, F., Gao, S., Friend, R. H., Cheetham, A. K. Chemically diverse and multifunctional hybrid organic–inorganic perovskites. Nature Reviews Materials, 2017, 2(3).

[19] Nagabhushana, G. P., Shivaramaiah, R., Navrotsky, A. Direct calorimetric verification of thermodynamic instability of lead halide hybrid perovskites. Proceedings of the National Academy of Sciences, 2016, 113(28), 7717–7721.

[20] Bartel, C. J., Sutton, C., Goldsmith, B. R., Ouyang, R., Musgrave, C. B., Ghiringhelli, L. M., Scheffler, M. New tolerance factor to predict the stability of perovskite oxides and halides. Science Advances, 2019, 5(2), eaav0693.

[21] Brivio, F., Walker, A. B., Walsh, A. Structural and electronic properties of hybrid perovskites for high-efficiency thin-film photovoltaics from first-principles. APL Materials, 2013, 1(4), 042111.

[22] Stoumpos, C. C., Malliakas, C. D., Kanatzidis, M. G. Semiconducting Tin and Lead Iodide Perovskites with Organic Cations: Phase Transitions, High Mobilities, and Near-Infrared Photoluminescent Properties. Inorganic Chemistry, 2013, 52(15), 9019–9038.

[23] Chen, Q., De Marco, N., Yang, Y. (Michael), Song, T.-B., Chen, C.-C., Zhao, H., Hong, Z.-R., Zhou, H.-P., Yang, Y. Under the spotlight: The organic–inorganic hybrid halide perovskite for optoelectronic applications. Nano Today, 2015, 10(3), 355–396.

[24] Poglitsch, A., Weber, D. Dynamic disorder in methylammonium trihalogenoplumbates (II) observed by millimeter-wave spectroscopy. The Journal of Chemical Physics, 1987, 87(11), 6373–6378.

[25] Whitfield, P. S., Herron, N., Guise, W. E., Page, K., Cheng, Y. Q., Milas, I., Crawford, M. K. Structures, Phase Transitions and Tricritical Behavior of the Hybrid Perovskite Methyl Ammonium Lead Iodide. Scientific Reports, 2016, 6(1).

[26] Ansari, M. I. H., Qurashi, A., Nazeeruddin, M. K. Frontiers, opportunities, and challenges in perovskite solar cells: A critical review. Journal of Photochemistry and Photobiology C: Photochemistry Reviews, 2018, 35, 1–24.

[27] Sutton, R. J., Filip, M. R., Haghighirad, A. A., Sakai, N., Wenger, B., Giustino, F., Snaith, H. J. Cubic or Orthorhombic? Revealing the Crystal Structure of Metastable Black-Phase CsPbI3 by Theory and Experiment. ACS Energy Letters, 2018, 3(8), 1787–1794.

[28] Chung, I., Song, J.-H., Im, J., Androulakis, J., Malliakas, C. D., Li, H., Freeman, A. J., Kenney, J. T., Kanatzidis, M. G. CsSnI3: Semiconductor or Metal? High Electrical Conductivity and Strong Near-Infrared Photoluminescence from a Single Material. High Hole Mobility and Phase-Transitions. Journal of the American Chemical Society, 2012, 134(20), 8579–8587.

[29] Trots, D. M., Myagkota, S. V. High-temperature structural evolution of caesium and rubidium triiodoplumbates. Journal of Physics and Chemistry of Solids, 2008, 69(10), 2520–2526.

[30] Fan, R., Huang, Y., Wang, L., Li, L., Zheng, G., Zhou, H. The Progress of Interface Design in Perovskite-Based Solar Cells. Advanced Energy Materials, 2016, 6(17), 1600460.

[31] Luo, S., Daoud, W. A. Recent progress in organic–inorganic halide perovskite solar cells: mechanisms and material design. Journal of Materials Chemistry A, 2015, 3(17), 8992–9010.

[32] Zhou, Z., Pang, S., Liu, Z., Xu, H., Cui, G. Interface engineering for high-performance perovskite hybrid solar cells. Journal of Materials Chemistry A, 2015, 3(38), 19205–19217.

[33] Noh, J. H., Im, S. H., Heo, J. H., Mandal, T. N., Seok, S. I. Chemical Management for Colorful, Efficient, and Stable Inorganic–Organic Hybrid Nanostructured Solar Cells. Nano Letters, 2013, 13(4), 1764–1769.

[34] McMeekin, D. P., Sadoughi, G., Rehman, W., Eperon, G. E., Saliba, M., Horantner, M. T., Haghighirad, A., Sakai, N., Korte, L., Bernd, R., Johnston, M., B., Herz, L., M., Snaith, H. J. A mixed-cation lead mixed-halide perovskite absorber for tandem solar cells. Science, 2016, 351(6269), 151–155.

[35] Hao, F., Stoumpos, C. C., Chang, R. P. H., Kanatzidis, M. G. Anomalous Band Gap Behavior in Mixed Sn and Pb Perovskites Enables Broadening of Absorption Spectrum in Solar Cells. Journal of the American Chemical Society, 2014, 136(22), 8094–8099.

[36] Yang, Z., Chueh, C.-C., Liang, P.-W., Crump, M., Lin, F., Zhu, Z., Jen, A. K.-Y. Effects of formamidinium and bromide ion substitution in methylammonium lead triiodide toward high-performance perovskite solar cells. Nano Energy, 2016, 22, 328–337.

[37] Rosencher, E., Vinter, B., Optoelectronics, Cambridge University Press, 2002.

[38] Colella, S., Mosconi, E., Fedeli, P., Listorti, A., Gazza, F., Orlandi, F., Ferro, P., Besagni, T., Rizzo, A., Calestani, G., Gigli, G., Angelis, F. D., Mosca, R. $MAPbI_{3-x}Cl_x$ Mixed Halide Perovskite for Hybrid Solar Cells: The Role of Chloride as Dopant on the Transport and Structural Properties. Chemistry of Materials, 2013, 25(22), 4613–4618.

[39] Prajongtat, P., Dittrich, T. Precipitation of $CH_3NH_3PbCl_3$ in $CH_3NH_3PbI_3$ and Its Impact on Modulated Charge Separation. The Journal of Physical Chemistry C, 2015, 119(18), 9926–9933.

[40] Cody, G. D., Tiedje, T., Abeles, B., Moustakas, T. D., Brooks, B., Goldstein, Y. DISORDER AND THE OPTICAL ABSORPTION EDGE OF HYDROGENATED AMORPHOUS SILICON. Le Journal de Physique Colloques, 1981, 42(C4), C4–301–C4–304.

[41] Kegelmann, L., Wolff, C. M., Awino, C., Lang, F., Unger, E. L., Korte, L., Dittrich, T., Neher, D., Rech, B., Albrecht, S. It Takes Two to Tango—Double-Layer Selective Contacts in Perovskite Solar Cells for Improved Device Performance and Reduced Hysteresis. ACS Applied Materials & Interfaces, 2017, 9(20), 17245–17255.

[42] De Wolf, S., Holovsky, J., Moon, S.-J., Löper, P., Niesen, B., Ledinsky, M., Haug, F.-J., Yum, J.-H., Ballif, C. Organometallic Halide Perovskites: Sharp Optical Absorption Edge and Its Relation to Photovoltaic Performance. The Journal of Physical Chemistry Letters, 2014, 5(6), 1035–1039.

[43] Levine, I., Gupta, S., Brenner, T. M., Azulay, D., Millo, O., Hodes, G., Cahen, D., Balberg, I. Mobility–Lifetime Products in MAPbI3 Films. The Journal of Physical Chemistry Letters, 2016, 7(24), 5219–5226.

[44] Edri, E., Kirmayer, S., Mukhopadhyay, S., Gartsman, K., Hodes, G., Cahen, D. Elucidating the charge carrier separation and working mechanism of $CH_3NH_3PbI_{3-x}Cl_x$ perovskite solar cells. Nature Communications, 2014, 5(1).

[45] Goodman, A. M. A Method for the Measurement of Short Minority Carrier Diffusion Lengths in Semiconductors. Journal of Applied Physics, 1961, 32(12), 2550–2552.

[46] Shargaieva, O., Lang, F., Rappich, J., Dittrich, T., Klaus, M., Meixner, M., Genzel, C., Nickel, N. H. Influence of the Grain Size on the Properties of $CH_3NH_3PbI_3$ Thin Films. ACS Applied Materials & Interfaces, 2017, 9(44), 38428–38435.

[47] Dittrich, T., Lang, F., Shargaieva, O., Rappich, J., Nickel, N. H., Unger, E., Rech, B. Diffusion length of photo-generated charge carriers in layers and powders of

$CH3NH_3PbI_3$ perovskite. Applied Physics Letters, 2016, 109(7), 073901.

[48] Dong, Q., Fang, Y., Shao, Y., Mulligan, P., Qiu, J., Cao, L., Huang, J. Electron-hole diffusion lengths > 175 μm in solution-grown $CH_3NH_3PbI_3$ single crystals. Science, 2015, 347(6225), 967–970.

[49] Wang, Q., Shao, Y., Xie, H., Lyu, L., Liu, X., Gao, Y., Huang, J. Qualifying composition dependent p and n self-doping in $CH_3NH_3PbI_3$. Applied Physics Letters, 2014, 105(16), 163508.

[50] Naikaew, A., Prajongtat, P., Lux-Steiner, M. C., Arunchaiya, M., Dittrich, T. Role of phase composition for electronic states in $CH_3NH_3PbI_3$ prepared from $CH_3NH_3I/PbCl_2$ solution. Applied Physics Letters, 2015, 106(23), 232104.

[51] Burschka, J., Pellet, N., Moon, S.-J., Humphry-Baker, R., Gao, P., Nazeeruddin, M. K., Grätzel, M. Sequential deposition as a route to high-performance perovskite-sensitized solar cells. Nature, 2013, 499(7458), 316–319.

[52] Ke, W., Fang, G., Liu, Q., Xiong, L., Qin, P., Tao, H., Wang, J., Lei, H., Li, B., Wan, J., Yang, G., Yan, Y. Low-Temperature Solution-Processed Tin Oxide as an Alternative Electron Transporting Layer for Efficient Perovskite Solar Cells. Journal of the American Chemical Society, 2015, 137(21), 6730–6733.

[53] Liu, D., Kelly, T. L. Perovskite solar cells with a planar heterojunction structure prepared using room-temperature solution processing techniques. Nature Photonics, 2013, 8(2), 133–138.

[54] Zhao, J., Zheng, X., Deng, Y., Li, T., Shao, Y., Gruverman, A., Shield, J., Huang, J. Is Cu a stable electrode material in hybrid perovskite solar cells for a 30-year lifetime? Energy & Environmental Science, 2016, 9(12), 3650–3656.

[55] Heo, J. H., Han, H. J., Kim, D., Ahn, T. K., Im, S. H. Hysteresis-less inverted $CH3NH_3PbI_3$ planar perovskite hybrid solar cells with 18.1% power conversion efficiency. Energy & Environmental Science, 2015, 8(5), 1602–1608.

[56] Jeng, J.-Y., Chen, K.-C., Chiang, T.-Y., Lin, P.-Y., Tsai, T.-D., Chang, Y.-C., Guo, T.-F., Chen, P., Wen, T.-C., Hsu, Y.-J. Nickel Oxide Electrode Interlayer in $CH_3NH_3PbI_3$ Perovskite/PCBM Planar-Heterojunction Hybrid Solar Cells. Advanced Materials, 2014, 26(24), 4107–4113.

[57] Frost, J. M., Butler, K. T., Brivio, F., Hendon, C. H., van Schilfgaarde, M., Walsh, A. Atomistic Origins of High-Performance in Hybrid Halide Perovskite Solar Cells. Nano Letters, 2014, 14(5), 2584–2590.

[58] Niu, G., Li, W., Meng, F., Wang, L., Dong, H., Qiu, Y. Study on the stability of $CH_3NH_3PbI_3$ films and the effect of post-modification by aluminum oxide in all-solid-state hybrid solar cells. J. Mater. Chem. A, 2014, 2(3), 705–710.

[59] Aristidou, N., Sanchez-Molina, I., Chotchuangchutchaval, T., Brown, M., Martinez, L., Rath, T., Haque, S. A. The Role of Oxygen in the Degradation of Methylammonium Lead Trihalide Perovskite Photoactive Layers. Angewandte Chemie International Edition, 2015, 54(28), 8208–8212.

[60] Jørgensen, M., Norrman, K., Krebs, F. C. Stability/degradation of polymer solar cells. Solar Energy Materials and Solar Cells, 2008, 92(7), 686–714.

[61] Hinsch, A., Kroon, J. M., Kern, R., Uhlendorf, I., Holzbock, J., Meyer, A., Ferber, J. Long-term stability of dye-sensitised solar cells. Progress in Photovoltaics: Research and Applications, 2001, 9(6), 425–438.

[62] Osterwald, C.R., Anderberg, A., Rummel, S., Ottoson, L., Degradation analysis of weathered crystalline-silicon PV modules, in: Proceedings of the Photovoltaic Specialists Conference Record of the Twenty-Ninth IEEE, 2002, 1392–1395.

[63] Leijtens, T., Eperon, G. E., Pathak, S., Abate, A., Lee, M. M., Snaith, H. J. Overcoming ultraviolet light instability of sensitized TiO2 with meso-superstructured organometal tri-halide perovskite solar cells. Nature Communications, 2013, 4(1).

[64] Wojciechowski, K., Leijtens, T., Siprova, S., Schlueter, C., Hörantner, M. T., Wang, J. T.-W., Li, C.-Z., Jen, A. K.-Y., Lee, T.-L., Snaith, H. J. C60 as an Efficient n-Type Compact Layer in Perovskite Solar Cells. The Journal of Physical Chemistry Letters, 2015, 6(12), 2399–2405.15.

[65] Tang, X., Brandl, M., May, B., Levchuk, I., Hou, Y., Richter, M., Chen, H., Chen, S., Kahmann, S., Osvet, A., Maier, F., Steinrück H.-P., Hock, R., Matt, G. J., Brabec, C. J. Photoinduced degradation of methylammonium lead triiodide perovskite semiconductors. Journal of Materials Chemistry A, 2016, 4(41),

15896–15903.

[66] Cuddihy, E. and Coulbert, C. and Gupta, A. and Liang, R. Electricity from photovoltaic solar cells: Flat-Plate Solar Array Project final report. Volume VII: Module encapsulation. JPL Publication, 1986, 86-31

[67] Conings, B., Drijkoningen, J., Gauquelin, N., Babayigit, A., D'Haen, J., D'Olieslaeger, L., Ethirajan, A., Verbeeck, J., Manca, J., Mosconi, E., Angelis, F. D., Boyen, H.-G. Intrinsic Thermal Instability of Methylammonium Lead Trihalide Perovskite. Advanced Energy Materials, 2015, 5(15), 1500477.

[68] Dualeh, A., Gao, P., Seok, S. I., Nazeeruddin, M. K., Grätzel, M. Thermal Behavior of Methylammonium Lead-Trihalide Perovskite Photovoltaic Light Harvesters. Chemistry of Materials, 2014, 26(21), 6160–6164.

[69] Philippe, B., Park, B.-W., Lindblad, R., Oscarsson, J., Ahmadi, S., Johansson, E. M. J., Rensmo, H. Chemical and Electronic Structure Characterization of Lead Halide Perovskites and Stability Behavior under Different Exposures-A Photoelectron Spectroscopy Investigation. Chemistry of Materials, 2015, 27(5), 1720–1731.

[70] Pisoni, A., Jaćimović, J., Barišić, O. S., Spina, M., Gaál, R., Forró, L., Horváth, E. Ultra-Low Thermal Conductivity in Organic–Inorganic Hybrid Perovskite $CH_3NH_3PbI_3$. The Journal of Physical Chemistry Letters, 2014, 5(14), 2488–2492.

[71] Liu, M., Johnston, M. B., Snaith, H. J. Efficient planar heterojunction perovskite solar cells by vapour deposition. Nature, 2013, 501(7467), 395–398.

[72] Chen, C.-W., Kang, H.-W., Hsiao, S.-Y., Yang, P.-F., Chiang, K.-M., Lin, H.-W. Efficient and Uniform Planar-Type Perovskite Solar Cells by Simple Sequential Vacuum Deposition. Advanced Materials, 2014, 26(38), 6647–6652.

[73] Momblona, C., Gil-Escrig, L., Bandiello, E., Hutter, E. M., Sessolo, M., Lederer, K., Blochwitz-Nimoth, J., Bolink, H. J. Efficient vacuum deposited p-i-n and n-i-p perovskite solar cells employing doped charge transport layers. Energy Environ. Sci., 2016, 9(11), 3456–3463.

[74] Conings, B., Babayigit, A., Klug, M. T., Bai, S., Gauquelin, N., Sakai, N., Wang,

J. T.-W., Verbeeck, J., Boyen, H.-G., Snaith, H. J. A Universal Deposition Protocol for Planar Heterojunction Solar Cells with High Efficiency Based on Hybrid Lead Halide Perovskite Families. Advanced Materials, 2016, 28(48), 10701–10709.

[75] Li, X., Bi, D., Yi, C., Decoppet, J.-D., Luo, J., Zakeeruddin, S. M., Hagfeldt, A., Gratzel, M. A vacuum flash-assisted solution process for high-efficiency large-area perovskite solar cells. Science, 2016, 353(6294), 58–62.

[76] Xiao, Z., Bi, C., Shao, Y., Dong, Q., Wang, Q., Yuan, Y., Wang, C., Gao, Y., Huang, J. Efficient, high yield perovskite photovoltaic devices grown by interdiffusion of solution-processed precursor stacking layers. Energy Environ. Sci., 2014. 7(8), 2619–2623.

[77] Chen, Q., Zhou, H., Hong, Z., Luo, S., Duan, H.-S., Wang, H.-H., Liu, Y., Li, J., Yang, Y. Planar Heterojunction Perovskite Solar Cells via Vapor-Assisted Solution Process. Journal of the American Chemical Society, 2013, 136(2), 622–625.

[78] Leyden, M. R., Ono, L. K., Raga, S. R., Kato, Y., Wang, S., Qi, Y. High performance perovskite solar cells by hybrid chemical vapor deposition. J. Mater. Chem. A, 2014, 2(44), 18742–18745.

[79] Grätzel, C., Zakeeruddin, S. M. Recent trends in mesoscopic solar cells based on molecular and nanopigment light harvesters. 2013, Materials Today, 16(1-2), 11–18.

[80] Jeon, N. J., Na, H., Jung, E. H., Yang, T.-Y., Lee, Y. G., Kim, G., Shin, H.-W., Seok, S. II, Lee, J., Seo, J. A fluorene-terminated hole-transporting material for highly efficient and stable perovskite solar cells. Nature Energy, 2018, 3(8), 682–689.

[81] Lee, M. M., Teuscher, J., Miyasaka, T., Murakami, T. N., Snaith, H. J. Efficient Hybrid Solar Cells Based on Meso-Superstructured Organometal Halide Perovskites. Science, 2012, 338(6107), 643–647.

[82] Ball, J. M., Lee, M. M., Hey, A., Snaith, H. J. Low-temperature processed meso-superstructured to thin-film perovskite solar cells. Energy & Environmental

Science, 2013, 6(6), 1739.

[83] Yu, Y., Wang, C., Grice, C. R., Shrestha, N., Chen, J., Zhao, D., Liao, W., Cimaroli, A. J., Roland, P. J., Ellingson, R. J., Yan, Y. Improving the Performance of Formamidinium and Cesium Lead Triiodide Perovskite Solar Cells using Lead Thiocyanate Additives. ChemSusChem, 2016, 9(23), 3288–3297.

[84] Luo, D., Yang, W., Wang, Z., Sadhanala, A., Hu, Q., Su, R., Shivanna, R., Trindade, G. F., Watts, J. F., Xu, Z., Liu, T., Chen, K., Ye, F., Wu, P., Zhao, L., Wu, J., Tu, Y., Zhang, Y., Yang, X., Zhang, W., Friend, R. H., Gong, Q., Snaith, H. J., Zhu, R. Enhanced photovoltage for inverted planar heterojunction perovskite solar cells. Science, 2018, 360(6396), 1442–1446.

[85] Jiang, Q., Zhano, Y., Zhang, X., Yang, X., Chen, Y., Chu, Z., Ye, Q., Li, X., Yin, Z., You, J., Surface passivation of perovskite film for efficient solar cells, Nature Photonics, 2019, 13, 460–466.

[86] Heo, J. H., Im, S. H. $CH_3NH_3PbBr_3$-$CH_3NH_3PbI_3$ Perovskite-Perovskite Tandem Solar Cells with Exceeding 2.2 V Open Circuit Voltage. Advanced Materials, 2015, 28(25), 5121–5125.

[87] Bailie, C. D., McGehee, M. D. High-efficiency tandem perovskite solar cells. MRS Bulletin, 2015, 40(08), 681–686.

[88] Jošt, M., Köhnen, E., Morales Vilches, A., Lipovšek, B., Jäger, K., Macco, B., Al-Ashouri, A., Krč, J., Korte, L., Rech, B., Schlatmann, R., Topič, M., Stannowski, B., Albrecht, S. Textured interfaces in monolithic perovskite/silicon tandem solar cells: Advanced light management for improved efficiency and energy yield. Energy & Environmental Science, 2018, 11, 3511-3523.

[89] Yang, Z., Rajagopal, A., Chueh, C.-C., Jo, S. B., Liu, B., Zhao, T. Jen, A. K.-Y. Stable Low-Bandgap Pb-Sn Binary Perovskites for Tandem Solar Cells. Advanced Materials, 2016, 28(40), 8990–8997.

[90] Eperon, G. E., Leijtens, T., Bush, K. A., Prasanna, R., Green, T., Wang, J. T., McMeekin, D. P., Volonakis, G., Milot, R. L., May, R., Palmstrom, A., Slotcavage, D. J., Belisle, R. A., Patel, J. B., Parrott, E. S., Sutton, R. J., Ma, W., Moghadam, F., Conings, B., Babayigit, A., Boyen, H. G., Bent, S., Giustino, F., Herz, L. M.,

Johnston, M. B., McGehee, M. D., Snaith, H. J. Perovskite-perovskite tandem photovoltaics with optimized band gaps. Science, 2016, 354(6314), 861–865.

[91] Ding, B., Li, Y., Huang, S.-Y., Chu, Q.-Q., Li, C.-X., Li, C.-J., Yang, G.-J. Material nucleation/growth competition tuning towards highly reproducible planar perovskite solar cells with efficiency exceeding 20%. Journal of Materials Chemistry A, 2017, 5(15), 6840–6848.

[92] Wu, Y., Yan, D., Peng, J., Duong, T., Wan, Y., Phang, S. P., Shen, H., Wu, N., Barugkin, C., Fu, X., Surve, S., Grant, D., Walter, D., White, T. P., Catchpole, K. R., Weber, K. J. Monolithic perovskite/silicon-homojunction tandem solar cell with over 22% efficiency. Energy & Environmental Science, 2017, 10(11), 2472–2479.

[93] Kronik, L., Shapira, Y. Surface photovoltage phenomena: theory, experiment, and applications. Surface Science Reports, 1999, 37(1-5), 1–206.

[94] Szaro, L., Rębisz, J., Misiewicz, J. Surface photovoltage in semiconductors under sub-band-gap illumination: continuous distribution of surface states. Applied Physics A: Materials Science & Processing, 1999, 69(4), 409–413.

[95] Duzhko, V., Timoshenko, V. Y., Koch, F., Dittrich, T. Photovoltage in nanocrystalline porousTiO2. Physical Review B, 2001, 64(7).

[96] Kronik, L., Shapira, Y. Surface photovoltage spectroscopy of semiconductor structures: at the crossroads of physics, chemistry and electrical engineering. Surface and Interface Analysis, 2001, 31(10), 954–965.

[97] Schroder, D. K. Surface voltage and surface photovoltage: history, theory and applications. Measurement Science and Technology, 2001, 12(3), R16–R31.

[98] Dittrich, T., Fengler, S. Surface photovoltage analysis of photoactive materials, World Scientific, 2019

[99] Dittrich, T., Bönisch, S., Zabel, P., Dube, S. High precision differential measurement of surface photovoltage transients on ultrathin CdS layers. Review of Scientific Instruments, 2008, 79(11), 113903.

[100] Snaith, H. J., Abate, A., Ball, J. M., Eperon, G. E., Leijtens, T., Noel, N. K., Stranks, S. D., Wang, W., Wojciechowski, K., Zhang, W. Anomalous Hysteresis

in Perovskite Solar Cells. The Journal of Physical Chemistry Letters, 2014, 5(9), 1511–1515.

[101] Kim, H.-S., Park, N.-G. Parameters Affecting I–V Hysteresis of $CH_3NH_3PbI_3$ Perovskite Solar Cells: Effects of Perovskite Crystal Size and Mesoporous TiO_2 Layer. The Journal of Physical Chemistry Letters, 2014, 5(17), 2927–2934.

[102] Tauc, J. Optical properties and electronic structure of amorphous Ge and Si. Materials Research Bulletin, 1968, 3(1), 37–46.

[103] Kurik, M. V. Urbach rule. Physica Status Solidi (a), 1971, 8(1), 9–45.

[104] Duzhko, V., Timoshenko, V. Y., Koch, F., Dittrich, T. Photovoltage in nanocrystalline porousTiO2. Physical Review B, 2001, 64(7).

[105] Welz, B., Becker-Ross, H., Florek, S., Heitmann, U. High-resolution continuum source AAS, Wiley-VCH, Weinheim, 2005.

[106] Welz, B., Vale, M. G. R., Florek, S., Okruss, M., Huang, M.-D., Becker-Ross, H. High-resolution Continuum Source Atomic Absorption Spectrometry-Theory and Applications. Encyclopedia of Analytical Chemistry, 2010.

[107] Butcher, D. J. Molecular absorption spectrometry in flames and furnaces: A review. Analytica Chimica Acta, 2013, 804, 1–15.

[108] Resano, M., Flórez, M. R., & García-Ruiz, E. Progress in the determination of metalloids and non-metals by means of high-resolution continuum source atomic or molecular absorption spectrometry. A critical review. Analytical and Bioanalytical Chemistry, 2013, 406(9-10), 2239–2259.

[109] Huang, M. D., Becker-Ross, H., Florek, S., Heitmann, U., Okruss, M. Determination of sulfur by molecular absorption of carbon monosulfide using a high-resolution continuum source absorption spectrometer and an air-acetylene flame. Spectrochimica Acta Part B: Atomic Spectroscopy, 2006, 61(2), 181–188.

[110] Heitmann, U., Becker-Ross, H., Florek, S., Huang, M. D., Okruss, M. Determination of non-metals via molecular absorption using high-resolution continuum source absorption spectrometry and graphite furnace atomization. Journal of Analytical Atomic Spectrometry, 2006, 21(11), 1314.

[111] Ferrieu, F. Infrared spectroscopic ellipsometry using a Fourier transform

infrared spectrometer: Some applications in thin-film characterization. Review of Scientific Instruments, 1989, 60(10), 3212–3216.

[112] Hinrichs, K., Gensch, M., Esser, N. Analysis of Organic Films and Interfacial Layers by Infrared Spectroscopic Ellipsometry. Applied Spectroscopy, 2005, 59(11), 272A–282A.

[113] Röseler, A., Korte, E. H., Reins, J. Applications of photometric ellipsometry in infrared spectroscopy. Vibrational Spectroscopy, 1993, 5(3), 275–283.

[114] Hinrichs, K., Eichhorn, K. J. Ellipsometry of Functional Organic Surfaces and Films, vol. 52. Springer International Publishing AG, part of Springer Nature, 2018.

[115] Atkins, P., Paula, J. Atkins' Physical Chemistry (10th Edition), Oxford University Press, 2014.

[116] IEC. Photovoltaic devices – Part 3: Measurement principles for terrestrial photovoltaic (PV) solar devices with reference spectral irradiance data, IEC60904-3, 2008, 1–62.

[117] RReDc, ASTM G173-03 reference spectra derived from SMARTS v. 2.9.2. Available at: https://rredc.nrel.gov/solar//spectra/am1.5/ASTMG173.html.

[118] Rühle, S. Tabulated values of the Shockley–Queisser limit for single junction solar cells. Solar Energy, 2016, 130, 139–147.

[119] LaMer, V. K., Dinegar, R. H. Theory, Production and Mechanism of Formation of Monodispersed Hydrosols. Journal of the American Chemical Society, 1950, 72(11), 4847–4854.

[120] Ocaña, M., Rodriguez-Clemente, R., Serna, C. J. Uniform colloidal particles in solution: Formation mechanisms. Advanced Materials, 1995, 7(2), 212–216.

[121] Ng, J., Xu, S., Zhang, X., Yang, H. Y., Sun, D. D. Hybridized Nanowires and Cubes: A Novel Architecture of a Heterojunctioned $TiO_2/SrTiO_3$ Thin Film for Efficient Water Splitting. Advanced Functional Materials, 2010, 20(24), 4287–4294.

[122] Yan, K., Long, M., Zhang, T., Wei, Z., Chen, H., Yang, S., Xu, J. Hybrid Halide Perovskite Solar Cell Precursors: Colloidal Chemistry and Coordination

Engineering behind Device Processing for High Efficiency. Journal of the American Chemical Society, 2015, 137(13), 4460–4468.

[123] Zhou, Y., Game, O. S., Pang, S., Padture, N. P. Microstructures of Organometal Trihalide Perovskites for Solar Cells: Their Evolution from Solutions and Characterization. The Journal of Physical Chemistry Letters, 2015, 6(23), 4827–4839.

[124] Li, Y., He, X.-L., Ding, B., Gao, L.-L., Yang, G.-J., Li, C.-X., Li, C.-J. Realizing full coverage of perovskite film on substrate surface during solution processing: Characterization and elimination of uncovered surface. Journal of Power Sources, 2016, 320, 204–211.

[125] Juma, A. O., Azarpira, A., Steigert, A., Pomaska, M., Fischer, C.-H., Lauermann, I., Dittrich, T. Role of chlorine in In2S3 for band alignment at nanoporous-TiO2/In2S3 interfaces. Journal of Applied Physics, 2013, 114(5), 053711.

[126] Jacobsson, T. J., Correa-Baena, J.-P., Halvani Anaraki, E., Philippe, B., Stranks, S. D., Bouduban, M. E. F., Tress, W., Schenk, K., Teuscher, J., Moser, J.-E., Rensmo, H., Hagfeldt, A. Unreacted PbI_2 as a Double-Edged Sword for Enhancing the Performance of Perovskite Solar Cells. Journal of the American Chemical Society, 2016, 138(32), 10331–10343.

[127] Li, Y., He, X.-L., Ding, B., Gao, L.-L., Yang, G.-J., Li, C.-X., Li, C.-J. Realizing full coverage of perovskite film on substrate surface during solution processing: Characterization and elimination of uncovered surface. Journal of Power Sources, 2016, 320, 204–211.

[128] Wharf, I., Gramstad, T., Makhija, R., Onyszchuk, M. Synthesis and vibrational spectra of some lead(II) halide adducts with O-, S-, and N-donor atom ligands. Canadian Journal of Chemistry, 1976, 54(21), 3430–3438.

[129] Miyamae, H., Numahata, Y., Nagata, M. THE CRYSTAL STRUCTURE OF LEAD(II) IODIDE-DIMETHYLSULPHOXIDE(1/2), PbI2(dmso)2. Chemistry Letters, 1980, 9(6), 663–664.

[130] Lewis, G. N. Acids and Bases. J. Franklin Inst. 1938, 226, 293−313.

[131] Pearson, R. G. Hard and Soft Acids and Bases. Journal of the American Chemical Society, 1963, 85(22), 3533–3539.

[132] Jorgensen, C. K. “Symbiotic” Ligands, Hard and Soft Central Atoms. Inorganic Chemistry, 1964, 3(8), 1201–1202.

[133] Fang, X., Wu, Y., Lu, Y., Sun, Y., Zhang, S., Zhang, J., Zhang, W., Yuan, N., Ding, J. Annealing-free perovskite films based on solvent engineering for efficient solar cells. Journal of Materials Chemistry C, 2017, 5(4), 842–847.

[134] Cataldo, F. A revision of the gutmann donor numbers of a series of phosphoramides including tepa. European Chemical Bulletin, 2015, 4(2), 92-97.

[135] Ahn, N., Son, D.-Y., Jang, I.-H., Kang, S. M., Choi, M., Park, N.-G. Highly Reproducible Perovskite Solar Cells with Average Efficiency of 18.3% and Best Efficiency of 19.7% Fabricated via Lewis Base Adduct of Lead(II) Iodide. Journal of the American Chemical Society, 2015, 137(27), 8696–8699.

[136] Saliba, M., Matsui, T., Seo, J.-Y., Domanski, K., Correa-Baena, J.-P., Nazeeruddin, M. K., Zakeeruddin, S. M., Tress, W., Abate, A., Hagfeldt, A., Grätzel, M. Cesium-containing triple cation perovskite solar cells: improved stability, reproducibility and high efficiency. Energy & Environmental Science, 2016, 9(6), 1989–1997.

[137] Han, Q., Bai, Y., Liu, J., Du, K., Li, T., Ji, D., Zhou, Y., Cao, C., Shin, D., Ding, J., Franklin, A. D., Glass, J. T., Hu, J., Therien, M. J., Liu, J., Mitzi, D. B. Additive engineering for high-performance room-temperature-processed perovskite absorbers with micron-size grains and microsecond-range carrier lifetimes. Energy & Environmental Science, 2017, 10(11), 2365–2371.

[138] Kim, M., Kim, G.-H., Oh, K. S., Jo, Y., Yoon, H., Kim, K.-H., Lee, H., Kim, J. Y., Kim, D. S. High-Temperature–Short-Time Annealing Process for High-Performance Large-Area Perovskite Solar Cells. ACS Nano, 2017, 11(6), 6057–6064.

[139] Skripkin, M. Y., Lindqvist-Reis, P., Abbasi, A., Mink, J., Persson, I., Sandström, M. Vibrational spectroscopic force field studies of dimethyl sulfoxide and hexakis(dimethyl sulfoxide)scandium(iii) iodide, and crystal and solution

structure of the hexakis(dimethyl sulfoxide)scandium(iii) ion. Dalton Trans., 2004, (23), 4038–4049.

[140] Chalapathi, V. V., Ramiah, K. V., Normal vibrations of N, N-dimethylformamide and N, N-dimethylacetamide. Proceedings of the Indian Academy of Sciences - Section A, 1968, 68(3), 109–122.

[141] Oxton, I. A., Knop, O., Duncan, J. I. The infrared spectrum and force field of the methyl-ammonium ion in $(CH_3NH_3)_2PtCl_6$. Journal of Molecular Structure, 1977, 38, 25–32.

[142] Glaser, T., Müller, C., Sendner, M., Krekeler, C., Semonin, O. E., Hull, T. D., Yaffe, O., Owen, J. S., Kowalsky, W., Pucci, A., Lovrinčić, R. Infrared Spectroscopic Study of Vibrational Modes in Methylammonium Lead Halide Perovskites. The Journal of Physical Chemistry Letters, 2015, 6(15), 2913–2918.

[143] Pérez-Osorio, M. A., Milot, R. L., Filip, M. R., Patel, J. B., Herz, L. M., Johnston, M. B., Giustino, F. Vibrational Properties of the Organic–Inorganic Halide Perovskite $CH_3NH_3PbI_3$ from Theory and Experiment: Factor Group Analysis, First-Principles Calculations, and Low-Temperature Infrared Spectra. The Journal of Physical Chemistry C, 2015, 119(46), 25703–25718.

[144] Nie, W., Tsai, H., Asadpour, R., Blancon, J.-C., Neukirch, A. J., Gupta, G., Crochet, J. J., Chhowalla, M., Tretiak, S., Alam, M. A., Wang, H.-L., Mohite, A. D. High-efficiency solution-processed perovskite solar cells with millimeter-scale grains. Science, 2015, 347(6221), 522–525.

[145] Kim, M., Kim, G.-H., Oh, K. S., Jo, Y., Yoon, H., Kim, K.-H., Lee, H., Kim, J. Y., Kim, D. S. High-Temperature–Short-Time Annealing Process for High-Performance Large-Area Perovskite Solar Cells. ACS Nano, 2017, 11(6), 6057–6064.

Publications

Journal articles

Qin Tan, Karsten Hinrichs, Mao Dong Huang, Steffen Fengler, Jörg Rappich, Pongthep Prajongtat, Norbert Nickel, and Thomas Dittrich, Temperature dependent diffusion of DMSO in $CH_3NH_3PbI_3$ precursor films during layer formation and impact on solar cells, ACS Applied Energy Materials, 2019, accepted.

Conference Presentations

Oral Presentation

Qin Tan, Karsten Hinrichs, Mao Dong Huang, Steffen Fengler, Jörg Rappich, Pongthep Prajongtat, Norbert Nickel, and Thomas Dittrich, Temperature dependent diffusion of DMSO during the crystallization of $CH_3NH_3PbI_3$ layers, nanoGe International Conference on Perovskite Solar Cells, Photonics and Optoelectronics (NIPHO19), 2019, Jerusalem (Israel).

Curriculum Vitae

Bachelor 09/2008-06/2012

South China University of Technology

Major: chemical engineering and technology

Undergraduate thesis: Improving the performance of photoanode in quantum-dot sensitized solar cells

Master 09/2012-06/2015

Dalian University of Technology

Major: fine chemical engineering

Master thesis: Design, synthesis and application of novel donor materials for small molecule organic solar cells

PhD 10/2015-10/2019

Helmholtz Zentrum Berlin für Materialien und Energie

Freie Universität Berlin

Major: physical chemistry

PhD thesis: Influence of vacuum-assisted solvent evaporation on $MAPbI_3$ layers and solar cells